

RESEARCH ARTICLE | MAY 09 2023

## Physics and instabilities of low-temperature $E \times B$ plasmas for spacecraft propulsion and other applications

Special Collection: [Papers from the 64th Annual Meeting of the APS Division of Plasma Physics](#)

Jean-Pierre Boeuf  ; Andrei Smolyakov 

 Check for updates

*Physics of Plasmas* 30, 050901 (2023)

<https://doi.org/10.1063/5.0145536>



View  
Online



Export  
Citation

CrossMark

Physics of Plasmas

Features in Plasma Physics Webinars

Register Today!

# Physics and instabilities of low-temperature $E \times B$ plasmas for spacecraft propulsion and other applications

Cite as: Phys. Plasmas **30**, 050901 (2023); doi: [10.1063/5.0145536](https://doi.org/10.1063/5.0145536)

Submitted: 6 February 2023 · Accepted: 15 April 2023 ·

Published Online: 9 May 2023




View Online



Export Citation



CrossMark

Jean-Pierre Boeuf<sup>1,a)</sup>  and Andrei Smolyakov<sup>2</sup> 

## AFFILIATIONS

<sup>1</sup>LAPLACE, Université de Toulouse, CNRS, INPT, UPS, 118 Route de Narbonne, 31062 Toulouse, France

<sup>2</sup>Department of Physics and Engineering Physics, University of Saskatchewan, Saskatoon, Saskatchewan S7N 5E2, Canada

**Note:** This paper is part of the Special Collection: Papers from the 64th Annual Meeting of the APS Division of Plasma Physics.

**Note:** Paper JT2 1, Bull. Am. Phys. Soc. **67** (2022).

<sup>a)</sup>Invited speaker. Author to whom correspondence should be addressed: [jpb@laplace.univ-tlse.fr](mailto:jpb@laplace.univ-tlse.fr)

## ABSTRACT

Low-temperature  $E \times B$  plasmas are used in various applications, such as Hall thrusters for satellite propulsion, ion sources and magnetron discharges for plasma processing, and negative ion sources for neutral beam injection in fusion. The plasmas in these devices are partially magnetized, meaning that the electrons are strongly magnetized while the ions are not. They are subject to various micro- and macro-instabilities that differ significantly from instabilities in fusion plasmas. These instabilities are often triggered by the large difference in electron and ion drift velocities in the  $E \times B$  direction. The possibility of maintaining a large electric field in the quasineutral plasma of Hall thrusters despite anomalous electron transport, or the presence of strong double layers associated with the azimuthal rotation of plasma structures (“rotating spokes”) in magnetron discharges and Hall thrusters are examples of the very challenging and exciting physics of  $E \times B$  devices. The turbulence and instabilities present in  $E \times B$  plasma devices constitute a major obstacle to the quantitative description of these devices and to the development of predictive codes and are the subject of intense research efforts. In this tutorial, we discuss the key aspects of the physics of low-temperature partially magnetized  $E \times B$  plasmas, as well as recent advances made through simulations, theory, and experiments in our understanding of the various types of instabilities (such as gradient-drift/Simon-Hoh and lower hybrid instabilities, rotating ionization waves, electron cyclotron drift instability, modified two-stream instability, etc.) that occur in these plasmas.

Published under an exclusive license by AIP Publishing. <https://doi.org/10.1063/5.0145536>

## I. INTRODUCTION

In low-temperature  $E \times B$  plasmas devices, an external magnetic field is placed perpendicular to the discharge current or to the electric field applied between two electrodes. The perpendicular magnetic field increases the electron residence time in the device and the electron collisionality, allowing plasma sustainment by electron impact ionization at low pressures and moderate applied voltage. The perpendicular magnetic field decreases the electron conductivity parallel to the electric field, so an objective of the  $E \times B$  configuration can also be to generate a large electric field in the quasineutral plasma, which can accelerate ions (application to gridless ion sources such as the Hall thruster). Lowering the electron conductivity with a perpendicular magnetic field is actually not trivial because of the development of instabilities that tend to increase

electron transport across the magnetic field. This question is at the center of this tutorial.

In most applications of  $E \times B$  plasmas, the external magnetic field and the device dimensions are such that electrons are strongly magnetized (Larmor radius much smaller than the device dimensions), while ions are not or are only weakly magnetized. Such plasmas are called “partially magnetized plasmas.” Electron transport along the electric field is, in principle, strongly reduced by the external magnetic field applied perpendicular to the electric field. In most devices, the magnetic field lines intersect a wall (cathode or dielectric surface) so that along the magnetic field line the electrons are electrostatically confined by the wall sheath potential. Electron confinement is therefore a combination of magnetic and electrostatic confinement. Collisionless electrons are trapped in the direction perpendicular to

the magnetic field. Only collisions with neutrals can un-trap the electrons from their cyclotron trajectory and allow transport across the magnetic field (“cross field transport”) along the electric field. Electron confinement by the magnetic field in the direction of the applied electric field is generally not as good as predicted by the classical collisional theory because of turbulence and instabilities that lead to cross field transport (“anomalous transport”). Because of their partial magnetization, the physics and instabilities of these plasmas are very distinct from those of other plasmas, e.g., for fusion applications.

The study of instabilities and anomalous transport in  $E \times B$  plasmas has recently attracted much attention, largely driven by the need to better understand the operation of devices, such as Hall thrusters and magnetron discharges, and to develop predictive models of these devices. Joint efforts by the low-temperature plasma community and the plasma propulsion community “to develop a rigorous understanding of the rich phenomena observed in  $E \times B$  devices” are described in a recent perspective article by Kaganovich *et al.*<sup>1</sup> that “presents the current understanding of the physics of these phenomena and state-of-the-art computational results, identifies critical questions, and suggests directions for future research”. The present tutorial article can be considered as complementary to the perspective article by Kaganovich *et al.*, but is aimed at non-specialists, with more emphasis on the physics of instabilities in various  $E \times B$  plasma devices.

In plasmas with perpendicular electric field and magnetic field, there is a charged particle drift in the  $E \times B$  direction (“ $E \times B$  drift”) with a velocity close to  $|E \times B|/B^2 = E/B$ . This drift plays an important role in regions of large electric fields. Electrons are subject to this drift while ions are accelerated out of the large electric field region before they have time to reach the  $E \times B$  drift velocity (this is another way to say that the plasma is partially magnetized). The large  $E \times B$  electron drift and the negligible ion drift in this direction can lead to charge separation and is often responsible for triggering instabilities. The electron pressure gradient  $\nabla P_e$  perpendicular to the magnetic field also creates a drift in the  $\nabla P_e \times B$  direction. This is the diamagnetic drift velocity,  $|\nabla P_e \times B|/enB^2 = |\nabla(nT_e)|/nB$  where  $n$  is the plasma density,  $e$  the elementary charge, and  $T_e$  the electron temperature in eV.  $E \times B$  and  $\nabla P_e \times B$  electron drift can both contribute to the development of instabilities. Instabilities are ubiquitous in low-temperature partially magnetized  $E \times B$  plasmas and can significantly enhance cross field electron transport. They manifest themselves in a wide range of unstable fluctuations, with frequencies from kilohertz to tens of megahertz and wavelengths from a fraction of millimeter to several centimeters.<sup>2</sup>

The electron drift in the  $E \times B$  direction gives rise to the Hall current. Efficient electron confinement parallel to the electric field requires that the Hall current does not intercept a wall (otherwise the Hall effect would destroy the confinement of electrons). This is possible if the Hall current is closed on itself, as for example, in a cylindrical geometry where the electric field is axial and the magnetic field radial, or the opposite. The Hall current in such geometries is in the azimuthal direction, i.e., is closed on itself. Plasma devices with closed electron drift are called closed-drift devices.<sup>3</sup>

The concept of closed-drift devices has led to important applications in ion sources for space propulsion (Hall thrusters, HT, also called stationary plasma thrusters, SPT,<sup>4–7</sup> and thrusters with anode layer, TAL<sup>5</sup>) and plasma processing (End-Hall ion sources,<sup>3,8,9</sup> closed-drift anode layer ion sources, ALIS,<sup>3,10</sup> or Anode Layer Plasma Accelerators,

ALPA<sup>3,11</sup>) The originality of these “Hall ion sources” lies in the fact that ions are extracted from the plasma not by a system of biased grids (they are “gridless ion sources”), but by the electric field generated in the quasineutral plasma by the local lowering of electron conductivity due to a magnetic field barrier placed between an emissive cathode and the anode. Magnetron discharges can also be considered as closed-drift ion sources where ions are extracted from the plasma and accelerated in the cathode sheath to sputter atoms from the cathode, with applications to thin film deposition. They can be operated at high power densities in a pulsed regime (HiPIMS, high power impulse magnetron sputtering).<sup>12–15</sup> In magnetron discharges as in Hall thrusters, electrons are heated by the applied dc electric field. They drift in the azimuthal  $E \times B$  direction, generate the plasma by ionization and slowly drift to the anode due to collisions or instabilities. Penning discharges,<sup>16–19</sup> consisting of two facing cathodes surrounded by a cylindrical anode, with an axial magnetic field, are another type of closed-drift device that has been used in many ion source applications. Hall ion sources, magnetron discharges, and Penning ion sources operate under pressure typically between a fraction of pascals and a few pascals but it is interesting to note that Penning discharges were first implemented as ion gauges<sup>20,21</sup> in the 1930s, operating at much lower pressures. In these conditions, the  $E \times B$  plasma can become non-neutral (electron density larger than ion density) and specific types of instabilities, called diocotron instabilities<sup>22–26</sup> are likely to develop.

Historical references on the development of  $E \times B$  devices for electric propulsion can be found in Refs. 3, 4, and 27, for magnetron discharges applications to sputtering and deposition in Refs. 12–15, and for various cross field devices operating over a wide pressure range in Refs. 23 and 28. Recent review or perspective papers on electric propulsion including gridless ion sources can be found in Refs. 29–31.

The question of cross field electron transport or anomalous transport also arises in situations where the plasma simply diffuses across the magnetic field, in the absence of applied voltage perpendicular to the magnetic field. The plasma can be generated by inductive coupling, microwave, or by injection of an electron beam. This is the case of magnetized plasma sources where the plasma is confined by magnetic cusps (applications to plasma processing or gridded ion sources<sup>32–34</sup>) or of magnetized cylindrical plasma columns with axial magnetic field. Magnetized plasma columns have been used extensively to study turbulence and anomalous electron transport.<sup>35–43</sup>  $E \times B$  and  $\nabla P_e \times B$  flows combine in these plasmas to ensure a zero net current to the walls. Diffusion is often non-ambipolar and “short-circuit” effects<sup>44</sup> are possible in the case of metallic walls, i.e., the electron current does not balance locally but globally the ion current and a large fraction of the electron current to the walls is in the parallel direction (along the magnetic field).  $E \times B$  plasmas have potential applications in mass separation, which requires the imposition and customization of an electric field perpendicular to the axial magnetic field in a plasma column to create an  $E \times B$  flow.<sup>45,46</sup> Research is ongoing into ways to generate this radial electric field, such as through electrode biasing,<sup>46–48</sup> the use of emissive end-electrodes,<sup>49</sup> or wave injection.<sup>50</sup>

$E \times B$  plasma devices, such as Hall ion sources or magnetron discharges, are now currently used successfully in space propulsion and plasmas processing applications. However, despite important research efforts and progress in the last two or three decades, the physics of these devices is still poorly understood and models of these plasmas with predictive capabilities are still lacking. In this article we

describe, for non-specialists, the basic physics of low-temperature partially magnetized  $E \times B$  plasmas, with emphasis on the development of instabilities, and we illustrate with some examples the recent progress in our understanding of these plasmas and their instabilities through experiments, simulation, and theory.

The basic physics and principles of  $E \times B$  plasma devices are presented in Sec. II. Section III shows how instabilities in  $E \times B$  plasmas can be described and understood with the combination of theory (dispersion relations) and simulations. Section IV focuses on two important  $E \times B$  plasma devices, the Hall thruster and the magnetron discharge, with a more detailed discussion of the physics and of the evidence of the presence of instabilities in these devices. Microscopic (kinetic) instabilities in Hall thrusters are studied in Sec. V with the help of a kinetic dispersion relation and particle simulations. The macroscopic instabilities that can be observed in magnetron discharges and under certain Hall thruster conditions (rotating spokes) are described in Sec. VI with particle simulations and comparisons with experiments.

## II. BASIC PHYSICS AND PRINCIPLES OF $E \times B$ PLASMA DEVICES

The typical conditions of low-temperature partially magnetized  $E \times B$  plasmas devices and the orders of magnitude of the plasma parameters are presented in Subsection II A. The classical, collisional transport theory is briefly recalled in Subsection II B. The geometry and principles of the main closed-drift devices are described in Subsection II C. The Hall effect, which occurs in devices with non-closed-drift, is discussed with two examples in Subsection II D.

### A. Conditions and orders of magnitude

Under usual conditions of  $E \times B$  plasmas applications, the effect of the plasma current on the magnetic field is negligible so we will assume that the magnetic field is purely external, i.e., is generated by a system of coils or magnets and a magnetic circuit. This condition may not be satisfied<sup>51</sup> in the extreme conditions of HiPIMS where very high power densities are injected in the plasma through short pulses of several microseconds.

As said in the introduction, we consider partially magnetized plasmas, which implies that the mean electron Larmor radius  $\rho_e$  is much smaller than the device dimensions  $\rho_e \ll L$  while the ion Larmor radius is not. For a Maxwellian electron velocity distribution at temperature  $T_e$ , the mean Larmor radius is given by  $\rho_e = v_{e\perp} / \omega_{ce}$  where  $v_{e\perp} = (eT_e/m)^{1/2}$  is the electron mean velocity perpendicular to the magnetic field, and  $\omega_{ce} = eB/m$  is the electron cyclotron angular frequency. Orders of magnitude of magnetic field intensity, charged particles cyclotron frequencies, and Larmor radii are given in Table I. Electron-neutral collisions play an important role in applications of  $E \times B$  plasmas because they control the electron magnetization and contribute to cross field transport (and also because the plasma is sustained by electron impact ionization). Hall ion sources and magnetron discharges operate at pressures typically between 0.1 and 5 Pa and with magnetic field usually smaller than 100 mT. The plasma dimensions are generally less than 5–10 cm. Table II gives some orders of magnitude of collision frequencies, and free paths of electron and argon ions.

Usual values of plasma densities, plasma frequencies, and electron Debye lengths are given in Table III.

**TABLE I.** Typical values of magnetic field intensities in low-temperature partially magnetized  $E \times B$  plasmas and corresponding values of electron and ion angular cyclotron frequencies,  $\omega_{ce}$  and  $\omega_{ci}$ , and mean Larmor radii,  $\rho_e$  and  $\rho_i$ , assuming Maxwellian distributions at 5 eV. The maximum magnetic field intensity is 10–20 mT in Hall thrusters and can be on the order of 100 mT in magnetron discharges.

| $B$ (mT)                                      | 1–100                                  |
|---|--|
| $\omega_{ce}$ (rad/s)                         | $1.8 \times 10^8 - 1.8 \times 10^{10}$ |
| $\rho_e$ ( $\mu\text{m}$ ) for 5 eV electrons | 5300–53                                |
| $\omega_{ci}$ (rad/s) Ar <sup>+</sup> ions    | $2.4 \times 10^3 - 2.4 \times 10^5$    |
| $\rho_i$ (cm) for 5 eV Ar <sup>+</sup> ions   | 140–1.4                                |

Since the electron trajectory around the magnetic field changes after each electron-neutral collision, leading to transport or diffusion across the magnetic field, an important parameter is the ratio of the electron Larmor frequency over the electron-neutral collision frequency. This ratio,  $h = \omega_{ce} / \nu_{en}$ , is called the Hall parameter and characterizes the electron confinement by the magnetic field. As said in the introduction, plasma fluctuations and instabilities also contribute to un-trapping the electrons from their trajectory around the magnetic field. Their effect can be considered as similar to the effect of collisions, and one can define an effective Hall parameter and an effective collision frequency to describe their effect on cross field transport. It can be deduced from Tables I and II that the Hall parameter associated with electron-neutral collisions, for a magnetic field intensity of 10 mT, and a gas pressure of 0.1 Pa is  $h = \omega_{ce} / \nu_{en} \approx 1000$ .

Note finally that low-temperature partially magnetized plasmas are far from thermal equilibrium, and that the electron temperature (defined as 2/3 of the thermal energy) is much larger than the ion temperature and the charged particle velocity distribution functions can be very far from Maxwellian.

### B. Classical, collisional cross field transport

In this section, the classical, collisional expression of the electron current across a magnetic field is derived from a simplified form of the steady-state, electron momentum equation. We neglect the inertia

**TABLE II.** Gas pressure range and corresponding values of gas density, collision frequencies with neutrals,  $\nu_{en}$ ,  $\nu_{in}$ , and free paths,  $\lambda_{en}$ ,  $\lambda_{in}$  of electrons and ions with 5 eV kinetic energy. The ion parameters are calculated for argon mass ( $M/m = 7.35 \times 10^4$ ). Note that the electron-neutral momentum cross section in argon varies by about 2 orders of magnitudes for electron energies between 1 and 10 eV (Ramsauer minimum). Some  $E \times B$  devices, such as ion gauges, can operate at gas pressures much below 0.1 Pa (in these conditions the plasma can be non-neutral). The gas density in the anode region of a Hall thruster (where xenon is injected) is on the order of  $2-3 \times 10^{19} \text{ m}^{-3}$  under nominal conditions, but can drop by a factor of 10 or more from the anode to the channel exhaust, due to ionization<sup>7</sup>.

| $p$ (Pa) – 300 K   | 0.1–5                                     |
|--|---|
| $p$ (mtorr)  | 0.75–37.5                                 |
| $N$ ( $\text{m}^{-3}$ )                                      | $2.4 \times 10^{19} - 1.2 \times 10^{21}$ |
| $\nu_{en}$ ( $\text{s}^{-1}$ ) for 5 eV electron             | $2 \times 10^6 - 10^8$                    |
| $\nu_{in}$ ( $\text{s}^{-1}$ ) for 5 eV Ar <sup>+</sup> ions | $2 \times 10^5 - 10^7$                    |
| $\lambda_{en}$ (cm) for 5 eV electron                        | 62–1.2                                    |
| $\lambda_{in}$ (cm) for 5 eV Ar <sup>+</sup> ions            | 7.7–0.15                                  |

**TABLE III.** Plasma density range and corresponding values of the electron and ion plasma frequencies,  $\omega_{pe}$ ,  $\omega_{pi}$ , and electron Debye length,  $\lambda_{De}$  for an electron temperature of 5 eV. The plasma density is a few  $10^{18} \text{ m}^{-3}$  in Hall thrusters operating under nominal conditions (whatever their size) and can vary between  $10^{16}$  and  $10^{18} \text{ m}^{-3}$  in dc magnetron discharges. The plasma density can be larger than  $10^{18} \text{ m}^{-3}$  in HIPIMS.

|  |  |
|--|--|
| $n \text{ (m}^{-3}\text{)}$                                  | $10^{15}\text{--}10^{18}$                    |
| $\omega_{pe} \text{ (s}^{-1}\text{)}$                        | $1.8 \times 10^9\text{--}5.6 \times 10^{11}$ |
| $\omega_{pi} \text{ (s}^{-1}\text{)}$ for $\text{Ar}^+$ ions | $6.6 \times 10^6\text{--}2.1 \times 10^8$    |
| $\lambda_{De} \text{ (\mu m)}$ for $T_e = 5 \text{ eV}$      | 530–17                                       |

term and assume that the electron pressure tensor is scalar. We consider a plasma with an electric field in the  $x$  direction, the magnetic field in the perpendicular  $z$  direction. We assume that the plasma density gradient is parallel to the electric field, in the  $x$  direction (as in Hall thrusters or magnetron discharges). The notations are indicated in Fig. 1.

Neglecting inertia and assuming a scalar electron pressure, the electron momentum equation is written as follows:

$$en[\mathbf{E} + \mathbf{v}_e \times \mathbf{B}] + e\nabla(nT_e) + mn\nu_{en}\mathbf{v}_e = \mathbf{0}, \quad (1)$$

where  $\mathbf{v}_e$  is the electron mean velocity,  $enT_e$  is the electron pressure, and the electron temperature  $T_e$  is expressed in eV. The projection of this equation on the  $x$  and  $y$  directions gives

$$\left\{ \begin{array}{l} v_{ex} = -\frac{\mu_{e0}}{1+h^2} \left( E + \frac{1}{n} \frac{\partial n T_e}{\partial x} \right) \approx -\frac{1}{hB} \left( E + \frac{1}{n} \frac{\partial n T_e}{\partial x} \right) \\ v_{ey} = -\frac{\mu_{e0} h}{1+h^2} \left( E + \frac{1}{n} \frac{\partial n T_e}{\partial x} \right) \approx -\frac{1}{B} \left( E + \frac{1}{n} \frac{\partial n T_e}{\partial x} \right) \end{array} \right\}, \quad (2)$$

where  $\mu_{e0} = e/(m\nu_{en})$  is the electron mobility without magnetic field, and we have assumed  $h^2 \gg 1$ . Note that the ratio of these velocities is equal to the Hall parameter,

$$\frac{v_{ey}}{v_{ex}} = h, \quad (3)$$

so the mean electron velocity in the  $\mathbf{E} \times \mathbf{B}$  direction can be significantly larger than the velocity parallel to the electric field. The two components of the mean velocity have two terms, one related to the electric field, and the other to the pressure gradient. The expression of the mean velocity parallel to the electric field is similar to the expression without magnetic field, with a drift term and a diffusion term, but

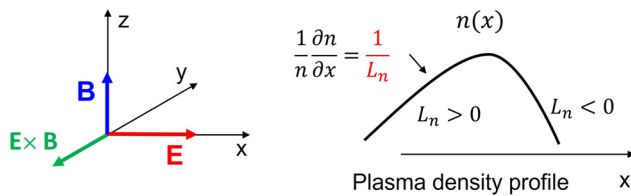


**FIG. 1.** Notations of the  $\mathbf{E} \times \mathbf{B}$  configuration: electric field  $\mathbf{E} = E\hat{x}$ , external magnetic field  $\mathbf{B} = B\hat{z}$ . In this configuration, the  $\mathbf{E} \times \mathbf{B}$  drift is in the  $-y$  direction. The plasma density gradient is supposed to be parallel to the electric field, in the  $x$  direction, with a characteristic length (positive or negative)  $L_n = \left(\frac{1}{n} \frac{\partial n}{\partial x}\right)^{-1}$ .

these coefficients are reduced by a factor  $(1+h^2) \approx h^2$  with respect to their expressions without magnetic field. The mobility parallel to the electric field can be written as follows:

$$\mu_{e\parallel E} \approx \frac{\mu_{e0}}{h^2} = \frac{1}{hB}. \quad (4)$$

The mean velocity in the  $y$  direction has also two components, one associated with the electric field, the  $\mathbf{E} \times \mathbf{B}$  drift velocity,

$$v_E = -\frac{E}{B}, \quad (5)$$

and one related to the pressure gradient, the  $\nabla P_e \times \mathbf{B}$  drift velocity or diamagnetic drift velocity,

$$v_{P_e} = -\frac{1}{Bn} \frac{\partial n T_e}{\partial x}, \quad (6)$$

where we have assumed  $h^2 \gg 1$ .

Along the magnetic field lines (in the  $z$  direction), electrons move freely between collisions. The electron conductivity parallel to the magnetic field is, therefore, much larger than the electron conductivity parallel to the electric field. An important consequence is that the magnetic field lines tend to be equipotential. More precisely, from the momentum equation along the magnetic field lines and assuming negligible electron current parallel to the magnetic field, the electric field along these lines must balance the electron pressure gradient. The potential drop along the magnetic field lines is therefore small for low electron temperature or small electron pressure gradient. Note that a magnetic field line should never connect cathode and anode in a magnetized plasma device since this would be equivalent to a short circuit at low pressure.

If the plasma is bounded by walls in the  $\mathbf{E} \times \mathbf{B}$ ,  $y$  direction, e.g., dielectric walls, there is an electron flow to one of the walls due to the  $\mathbf{E} \times \mathbf{B}$  and  $\nabla P_e \times \mathbf{B}$  drifts. The electron flow to the wall must be balanced by an ion flow. An electric field is, therefore, generated in the  $y$  direction to draw the ions to the wall. This is the Hall effect. This electric field, combined with the magnetic field, will in turn create an  $\mathbf{E} \times \mathbf{B}$  electron drift in the  $x$  direction that will destroy the electron confinement. The question of Hall effect in low-temperature partially magnetized plasmas has been illustrated analytically in the case of a plasma column in a transverse magnetic field by Ecker and Kanne<sup>52</sup> and by Kunkel,<sup>53</sup> and with particle simulations<sup>54</sup> in the case of the negative ion source for the neutral beam injector of ITER. This is summarized in Subsection II D. The solution to avoid the Hall effect is to choose a geometry where the  $\mathbf{E} \times \mathbf{B}$  electron current is closed on itself. This is possible in a cylindrical geometry where the electric field is axial and the magnetic field is radial or the opposite. Devices with this configuration are called closed-drift devices<sup>3</sup> and are described in Subsection II C.

### C. Closed drift devices

Some classical examples of closed-drift devices are displayed in Fig. 2. In Penning cells and cylindrical magnetron discharges [Figs. 2(a) and 2(b)], the external magnetic field is axial, and the applied electric field is radial. The concept of Penning discharge [Fig. 2(a)] was introduced by Phillips at the end of the 19th century<sup>55</sup> and was used for the first time in 1937 by Penning, with the construction of an

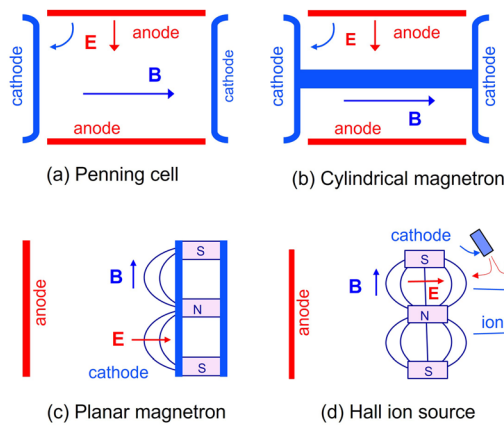


**FIG. 2.** Schematic of the principles of several  $E \times B$  discharge devices with axial magnetic field and radial electric field (a) and (b) or axial electric field and radial magnetic field (c) and (d). In all these devices, the Hall current is in the azimuthal direction.

ionization gauge.<sup>20</sup> The different modes of a Penning discharge with a long anode cylinder at low pressure were studied by Knauer<sup>56</sup> and Schuurmann<sup>16,17</sup> and the diocotron instability that develops in Penning discharge at low pressures was described by Knauer.<sup>22</sup> More recent experimental work on Penning discharges and their different regimes can be found in the article by Mamedov *et al.*<sup>57</sup>

Penning discharges are currently used as ion sources<sup>19</sup> (ions can be extracted through an aperture in one of the two cathodes or through the anode) in various applications, e.g., to sputtering and deposition, ion implantation,<sup>58</sup> isotope separation, production of hydrogen negative ions,<sup>59</sup> and neutron generators.<sup>60</sup> The electron vortices associated with the diocotron instability, which develop in Penning discharges and in cylindrical magnetrons at very low pressures, were extensively studied by Kervalishvili and his group<sup>25,61–64</sup> with the help of probe measurements and described with particle simulations in Ref. 26. Cylindrical magnetrons [Fig. 2(b)] consist of two concentric cylindrical electrodes with an axial magnetic field. Early sputtering-deposition applications were demonstrated in cylindrical magnetrons,<sup>14,65</sup> but the planar magnetron configuration [Fig. 2(c)] is now much more commonly used for deposition of metallic or compound thin films in many industrial applications. The planar magnetron can operate in a dc regime in the pressure range 0.2–4 Pa with applied voltages of 300–700 V and a magnetic field of 20–50 mT close to the cathode.<sup>14</sup> Very high power densities can be achieved in a pulsed regime (HiPIMS)<sup>13,15</sup> with repetition frequency in the range 50–5000 Hz and 1%–3% duty cycle,<sup>12–14</sup> applied voltage in the range 500–2000 V and with peak power densities up to several kW/cm<sup>2</sup>. The plasma density is  $10^{16}$ – $10^{18}$  m<sup>-3</sup> in the dc case and can be larger than  $10^{18}$ – $10^{19}$  m<sup>-3</sup> in the pulsed case. The physics of HiPIMS is extremely complex because of the high plasma density, ionization of the sputtered atoms, instabilities, neutral depletion, etc.

The magnetic field in planar magnetrons is generated by magnets placed behind the cathode as schematically shown in Fig. 2(c). In a Hall ion source [Fig. 2(d)], the objective is to generate an electric field in the quasineutral plasma and to use this field to extract ions from the plasma. The basic idea is, therefore, to place a magnetic barrier perpendicular

to the applied electric field between an emissive cathode and the anode, as shown schematically in Fig. 2(d).

Figure 3 shows some practical examples of Hall ion sources. In a Hall thruster<sup>5,7,66</sup> [Fig. 3(a)], the plasma is formed in a channel between two concentric cylinders. The anode is at one end of the channel, and an electron emissive cathode is placed outside the channel. A radial magnetic field with a maximum at the other end of the channel (“exhaust plane”) is generated by coils or magnets and a magnetic circuit. This magnetic field forms a magnetic barrier between cathode and anode. The applied electric field tends to be larger in the region of maximum magnetic field because of the lowering of the electron conductivity due to the magnetic barrier. Ions generated in the channel are extracted by this electric field. The external emissive cathode provides electrons to sustain the discharge as well as to neutralize the extracted ion beam. Several variations around this concept have been proposed and developed. Some of these designs are described in recent review papers.<sup>29,30,67</sup>

Here, we only give a brief description of some of these designs to illustrate the different possible  $E \times B$  configurations. The configuration of a magnetically shielded Hall thruster<sup>68–70</sup> is shown in Fig. 3(b). The magnetic barrier in this thruster is such that the magnetic field in the channel, close to the exhaust plane is parallel to the dielectric walls. Since the magnetic field lines tend to be equipotential (because of the large electron conductivity along these lines), this configuration limits

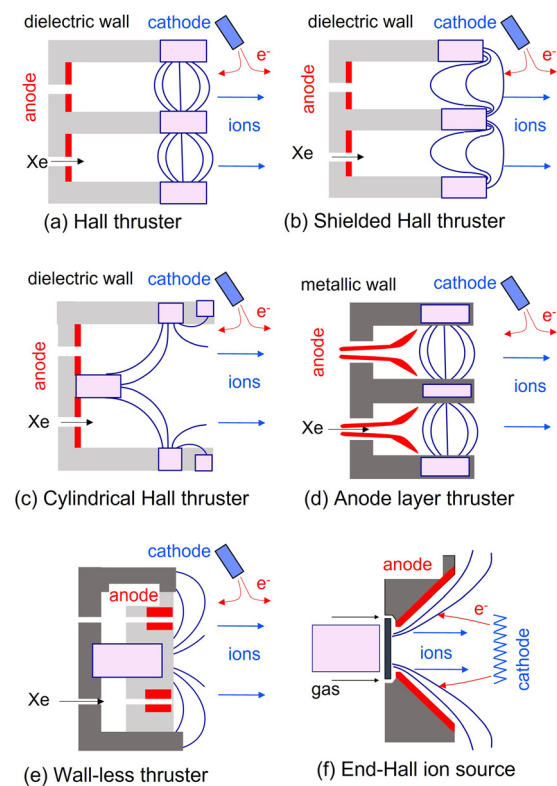


**FIG. 3.** Examples of Hall ion sources or gridless ion sources. (a)–(e) are different types of gridless ion thrusters, and (f) is an ion source used for plasma processing (e.g., for ion assist thin film coating). These figures only show the basic principles of these devices (magnetic circuit is not represented).

the electron and ion fluxes to the walls and reduces ion erosion in this region. The cylindrical Hall thruster<sup>71–73</sup> [Fig. 3(c)], where the inner cylinder is shorter, is more adapted to small or low-power thrusters since, according to the empirical scaling laws of Hall thrusters, the channel width of the channel between the two dielectric cylinder should decrease with decreasing power. The magnetic field barrier in this thruster is not perpendicular to the thruster axis so the electric field is not perfectly axial, and the divergence of the ion beam is larger than in standard Hall thrusters. The anode layer thruster (or thruster with anode layer, TAL)<sup>74,75</sup> is shown in [Fig. 3(d)]. In this thruster, the anode is very close to the magnetic barrier and the dielectric walls are no longer needed and are replaced by metallic walls. Ions are accelerated in a thin region close to the anode. Ion sources based on the same concept as TAL are also used in plasma processing applications under the name of ALIS<sup>3,10</sup> (anode layer ion sources) or ALPA<sup>11,76</sup> (Anode Layer Plasma Accelerators). Another thruster configuration where the anode is in the magnetic barrier is the wall-less thruster<sup>77</sup> of [Fig. 3(e)] proposed by Kapulkin *et al.*<sup>78</sup> in the 1990s, and by Mazouffre *et al.*<sup>79–81</sup> later. A variation of a wall-less thruster is based on a standard Hall thruster with a short channel but with a ring anode placed at the channel exit. The ion acceleration in this design takes place outside the channel. The advantage of the configuration of Fig. 3(e) is its simplicity and reduced erosion problems, but the divergence of the ion beam can be an issue. Finally, gridless ion sources are not only used for spacecraft propulsion but also for plasma processing applications. This is the case of the ALIS and ALPA source mentioned above and of the End-Hall ion sources<sup>10</sup> of Fig. 3(f), with a truncated conical anode and a magnetic field barrier along the anode surface. This ion source is used for ion assisted thin film deposition.<sup>82</sup> Particle simulations of End-Hall ion sources can be found in Refs. 9 and 83.

A final remark on the magnetic field configuration of closed-drift devices is that in all cases, the magnetic field lines intersect the cathode or some dielectric surfaces. Electrons move freely along the magnetic field lines, so, as said in the introduction, the electron confinement is not purely magnetic but is a combination of magnetic confinement in the direction perpendicular to the applied electric field and electrostatic confinement along the magnetic field lines. In configurations where the magnetic field lines end on the cathode (Penning or magnetron discharges), plasma electrons are efficiently confined electrostatically because of the large potential drop in the cathode sheaths. In configurations where the magnetic field lines intersect a dielectric surface (most of the Hall ion sources), low-energy electrons are electrostatically confined by the wall sheath potential, but higher energy electrons can overcome this wall potential and reach the wall. Electron-wall interactions and the resulting secondary electron emission can play an important role in these devices.<sup>1</sup>

From this brief review, it appears that in closed-drift devices with axial electric field and radial magnetic field (magnetron discharges and Hall ion sources), there can be three generic types of axial profiles of the radial magnetic field, as shown in Fig. 4. The three profiles correspond to (1), magnetron discharges, with a magnetic field decreasing from cathode to anode, (2) standard Hall thrusters, with a magnetic barrier between cathode and anode, and (3) ion sources with anode layers, where the magnetic field increases from cathode to anode. The choice between these three configurations depends on the application and on the objective to be achieved (performance, lifetime, simplicity,...). We will see in the rest of this paper that the magnetic field

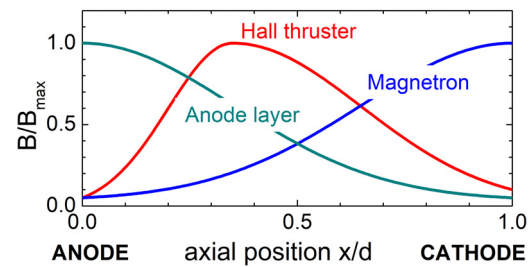


FIG. 4. Axial profiles of the normalized radial magnetic field in Hall thrusters, magnetron discharges, and anode layer ion sources (at the radial position where the axial component of the magnetic field is zero).

profile has also important consequences on the nature of the instabilities that develop in these devices and on their consequences on anomalous electron transport.

### D. $E \times B$ plasmas with non-closed drift: The Hall effect

The Hall effect occurs when the  $E \times B$  current is not closed on itself but flows to a wall. There is no Hall effect in closed-drift devices like the Hall thruster even though Hall thrusters are sometimes called “Hall effect thrusters.” To illustrate the Hall effect, we consider, as in Kunkel<sup>53</sup> (see also Ecker<sup>52</sup> for the case of a cylindrical column) a plasma slab between two dielectric or floating walls parallel to the  $x$  direction and perpendicular to the  $y$  direction, an electric field  $E_0 = E_0 \hat{x}$  in the  $x$  direction and a perpendicular magnetic field  $B = B \hat{z}$  in the  $z$  direction. The electric field  $E_0$  must adjust so that charged particle losses to the walls are balanced by ionization, as in a positive column plasma. The  $E \times B$  electron current, in the  $-y$  direction, flows to the wall. These conditions are represented schematically in Fig. 5.

We assume that the plasma column is uniform in the  $x$  direction ( $\partial n / \partial x = 0$ ), with a constant electron temperature, and that the plasma density is a function of  $y$  only ( $\partial n / \partial y$  is non-zero due to the presence of the walls). The electron current to the wall must be balanced by an ion current so an electric field must form to draw the ions to the walls and ensure a zero net current. This electric field is the Hall electric field. The Hall electric field,  $E_H = E_H \hat{y}$ , combined with the

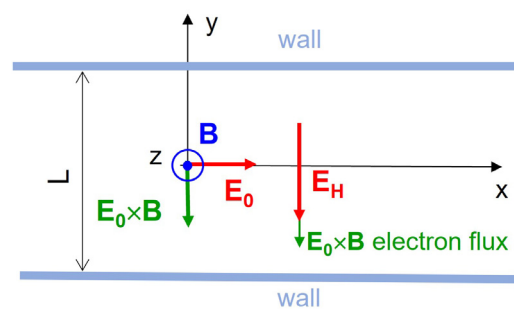


FIG. 5. Positive column plasma slab with a uniform axial electric field  $E_0 = E_0 \hat{x}$  and a perpendicular magnetic field  $B = B \hat{z}$  between two planar walls. Due to the non-closed drift in the  $E \times B$  direction, an electric field  $E_H = E_H \hat{y}$  forms in the  $y$  direction, to oppose the Hall electron current to the wall. This creates an asymmetric profile of the plasma density between the walls. The width of the plasma column is  $L$ .

perpendicular magnetic field can in turn generate an  $\mathbf{E} \times \mathbf{B}$  drift in the  $x$  direction. One can easily write a simplified momentum equation as Eq. (1), except that there is now a component of the electric field,  $E_H$ , and a density gradient  $\partial n/\partial y$  in the  $y$  direction, and we assume a zero-density gradient in the  $x$  direction. We obtain

$$\left\{ \begin{aligned} v_{ex} &= -\frac{\mu_{e0}}{1+h^2}E_0 + \frac{\mu_{e0}h}{1+h^2}E_H^* \\ v_{ey} &= -\frac{\mu_{e0}}{1+h^2}E_H^* - \frac{\mu_{e0}h}{1+h^2}E_0 \end{aligned} \right\}, \quad (7)$$

where  $E_H^* = E_H + \frac{T_e}{n} \frac{\partial n}{\partial y}$ .

The plasma is quasineutral so the condition for a zero current to the wall is that the electron mean velocity  $v_{ey}$ , and ion mean velocity  $v_{iy}$  to the walls are equal. We assume collisional, non-magnetized ions with a mobility  $\mu_i$ , and we neglect ion diffusion. Writing  $v_{iy} = \mu_i E_H$  in Eq. (7), we obtain the following expression for  $E_H$ :

$$E_H = -\frac{h}{\alpha}E_0 - \frac{1}{\alpha} \frac{T_e}{n} \frac{\partial n}{\partial y}, \quad \text{with } \alpha = 1 + \frac{\mu_i}{\mu_{e0}}(1+h^2). \quad (8)$$

The average value of  $E_H$  in the  $y$  direction is  $\overline{E_H} = -\frac{h}{\alpha}E_0$  and there is a potential drop  $U_H = -\frac{h}{\alpha}E_0L$  between the wall sheaths, the Hall voltage (the sheath thickness is neglected in this quasineutral approximation). The second term in the expression of  $E_H$  in Eq. (8) is the ambipolar field.

Using the expression (8) of  $E_H$  in Eq. (7), we obtain the following expression for the mean electron velocity  $v_{ex}$  parallel to the axial electric field:

$$v_{ex} = -\frac{\mu_{e0}}{(1+h^2)} \left(1 + \frac{h^2}{\alpha}\right) E_0 - \frac{\mu_{e0}h}{(1+h^2)} \left(1 - \frac{1}{\alpha}\right) \frac{T_e}{n} \frac{\partial n}{\partial y}. \quad (9)$$

The mean velocity parallel to the electric field,  $E_x$ , averaged in the  $z$  direction is  $\overline{v_{ex}} = -\frac{\mu_{e0}}{(1+h^2)} \left(1 + \frac{h^2}{\alpha}\right) E_0$ . This is to be compared to the mean velocity in the absence of Hall effect, given by Eq. (2),  $\overline{v_{ex}} = -\frac{\mu_{e0}}{1+h^2} E_0$ . Since the ratio of ion to electron mobility without magnetic field,  $\mu_i/\mu_{e0}$  can be on the order of  $10^{-2}$  or less, we have generally  $(1 + \frac{h^2}{\alpha}) \gg 1$ . The electron mobility parallel to the electric field  $E_x$  in the presence of Hall effect is therefore considerably larger than without Hall effect and, in the limit  $\mu_i/\mu_{e0} \rightarrow 0$ ,  $\alpha \rightarrow 1$ , and we have  $\overline{v_{ex}} \rightarrow -\mu_{e0}E_0$ . We can conclude that the Hall effect tends to destroy the electron confinement perpendicular to the magnetic field.

A consequence of the presence of the Hall electric field in the  $y$  direction is that the plasma density is no longer symmetric in this direction. This can be seen by writing a continuity equation assuming a constant ionization frequency. The charged particle flux in this equation contains an ambipolar term and a term related to the Hall current. One can easily show (see Kunkel<sup>53</sup>) that the density profile along  $y$  is of the following form (with an eigenvalue condition that connects ionization frequency, ambipolar diffusion and parameters related to the Hall effect<sup>53</sup>):

$$n(y) = n_0 \exp\left(h \frac{E_0}{2T_e} y\right) \sin(\pi y/L), \quad (10)$$

where  $L$  is the distance between the walls. The usual sinusoidal profile for ambipolar diffusion between planar walls is obtained in the absence of Hall effect ( $h = 0$ ).

The simple example above corresponds to an axially uniform plasma column between parallel walls in the presence of a perpendicular magnetic field.

We consider now the more complex example of a negative ion source used for the neutral beam injection system of ITER.<sup>84</sup> The design of this source is schematically represented in Fig. 6. The source consists of a driver where electrons are heated by inductive coupling, a diffusion region with a magnetic filter, and an extraction region. The magnetic field is perpendicular to the plane of Fig. 6. The plasma is produced in hydrogen or deuterium at 0.3 Pa. The negative ions of hydrogen or deuterium are generated in the plasma volume by attachment on vibrationally excited states, and on the surface of the plasma grid covered with a cesium layer. Hydrogen or deuterium atoms hitting the caesiated grid are converted into negative ions. Negative ions are extracted through a system of biased grids. Negative ions can be destroyed by fast electrons coming from the driver. The objective of the magnetic filter in the diffusion region is to increase the residence time of electrons and increase their energy losses through collisions with neutrals. A second objective is also to lower the density of electrons close to the extraction region and to limit their extraction through the grids (in addition to the magnetic filter, a magnetic field is also generated by magnets near and parallel to each grid hole to limit this flux).

The plasma density gradient from the driver to the magnetic filter due to the large electron pressure in the driver creates a charged particle flux toward the extraction grids. The grid voltage is positive with respect to the grounded walls to enhance the flux of negative ions to the extraction system. In this configuration, there is an axial flux of charged particles perpendicular to the magnetic field. We therefore expect to have a combination of diamagnetic drift and  $\mathbf{E} \times \mathbf{B}$  drift in the  $y$  direction of Fig. 6. These drifts are not closed and are perpendicular to the

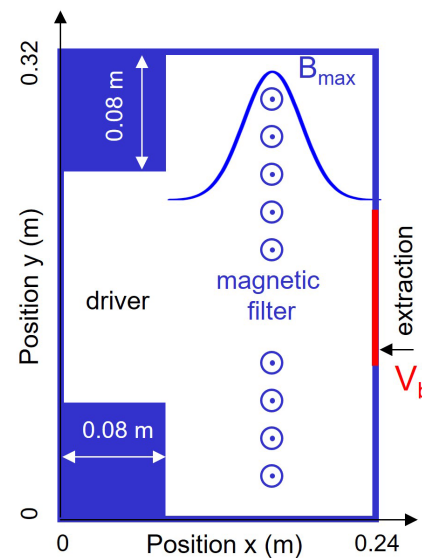
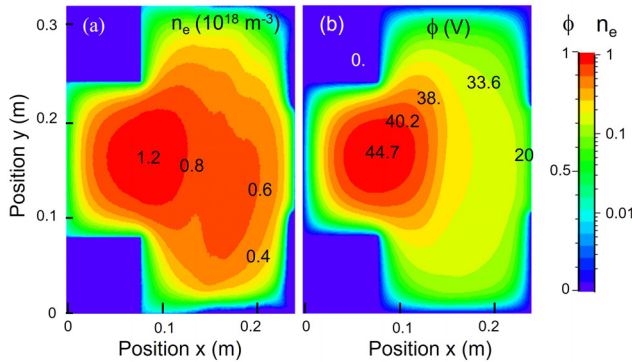


FIG. 6. Two-dimensional rectangular geometry considered in the 2D PIC MCC simulations<sup>85</sup> of the ITER negative ion source for neutral beam injection.<sup>84</sup> The chamber walls are metallic and grounded, and the right electrode (“plasma grid”) is biased at a voltage  $V_b$ . The magnetic field is perpendicular to the simulation domain (upward) and is constant along the  $y$  direction.





**FIG. 7.** 2D distributions of (a) electron density and (b) electric potential in the source in the conditions of Fig. 6. The color scale is linear for  $\phi$  (unit 45 V), and log on three decades for  $n_e$  (unit  $10^{18} \text{ m}^{-3}$ ).  $\text{H}_2$ , pressure 0.3 Pa, maximum magnetic field  $B_{\text{max}} = 3 \text{ mT}$ , bias voltage  $V_b = 20 \text{ V}$ , power absorbed in the driver  $100 \text{ kW/m}$ . The scale factor of the PIC-MCC simulation is  $\eta = 2 \times 10^4$  (i.e., the simulations are performed with a plasma density  $\eta$  times lower than indicated in (a) in Poisson equation). Adapted with permission from Boeuf *et al.*, Phys. Plasmas **19**, 113510 (2012). Copyright 2012 AIP Publishing (Fig. 3 of Ref. 85).

rectangular chamber walls, so we expect a Hall effect to occur. This Hall effect is discussed in Refs. 85–88, on the basis of PIC-MCC simulations. We present here a few results from Ref. 85. Figure 7 shows the 2D distributions of the electron density and plasma potential in the ion source. The plasma potential in the driver is much larger than in the diffusion chamber because electrons are heated in the driver and lose energy in the filter.

We observe on the potential and plasma density distributions an asymmetry, which can be attributed to the Hall effect. There is a potential difference (Hall voltage) between the sheath edges on the top and bottom walls. The plasma density is higher on the lower side of the chamber (while the electron temperature is lower on the lower side, see Ref. 89).

Figure 8 displays the intensity and streamlines of the electron and ion current densities in the chamber. We can clearly see the combination of the different electron drifts in the  $y$  direction at the driver

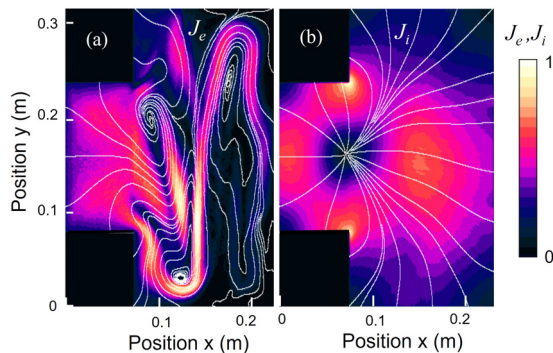


**FIG. 8.** Intensity and streamlines of (a) electron current density (unit  $8 \text{ kA/m}^2$ ), and (b) ion current density (unit  $2.8 \text{ kA/m}^2$ ) in the source in the conditions of Figs. 6 and 7.  $\text{H}_2$ , pressure 0.3 Pa, maximum magnetic field  $B_{\text{max}} = 3 \text{ mT}$ , bias voltage  $V_b = 20 \text{ V}$ , power absorbed in the driver  $100 \text{ kW/m}$ . Reproduced with permission from Boeuf *et al.*, Phys. Plasmas **19**, 113510 (2012). Copyright 2012 AIP Publishing (Fig. 7 of Ref. 85).

exit (diamagnetic and  $\mathbf{E} \times \mathbf{B}$  drift; a drift due to the magnetic field gradient, proportional to  $\nabla \mathbf{B} \times \mathbf{B}$  is also present). The more important plasma asymmetry predicted by the model at the driver exit has been confirmed by experiments.<sup>90</sup> Compared with a closed-drift system, the Hall effect enhances the electron flow through the magnetic filter, and no instability is observed in these conditions.

If the walls are removed in the  $y$  direction and periodic conditions are used instead (see Ref. 91), the drift is closed on itself and electron confinement in the axial direction is much more efficient. In these conditions, instabilities are present,<sup>91</sup> which is not the case in the bounded conditions of Figs. 7 and 8. Finally, we note, by comparing Figs. 8(a) and 8(b), that the plasma diffusion in this source is clearly non-ambipolar except in the magnetic field free driver. Non-magnetized ions simply go down the potential while the streamlines of the electron current density are much more complex. This feature is typical of partially magnetized plasmas.

### III. THEORY AND MODELING OF INSTABILITIES IN $\mathbf{E} \times \mathbf{B}$ PLASMAS

The basic way to study the existence of instabilities in a physical system is to look at how perturbations around a given steady state grow in time or are damped. This is done by linearizing the equations characterizing the steady state regime. In plasmas, instabilities are described by linearizing transport equation coupled with field equations. For some instabilities, a fluid approach of the transport equations is sufficient (macroscopic instabilities) but in some cases, a kinetic description is required (microscopic, or kinetic instabilities). The linearization of the equations gives the dispersion relations, i.e., the frequency and growth rate of the perturbations as a function of wavenumber, and are extremely useful to understand the mechanisms responsible for the development of the instabilities. However, this approach can describe only the linear stage of the development of the instability and cannot predict how the instability saturates. Numerical simulations based on fluid or kinetic (e.g., Particle-In-Cell simulations) transport equations must be used to study the evolution from the linear stage to the saturated stage of the instability but the interpretation of numerical results is not always straightforward. The best approach to fully understand the physics of the instabilities is, therefore, to combine the derivation of the dispersion relations by linearization of the equations, with numerical simulations.

$\mathbf{E} \times \mathbf{B}$  plasma devices are complex physical systems, and it should be kept in mind that before trying to develop fully predictive engineering models of these devices, it is important to build simplified or reduced models at the right level of description and approximation. As stated in Ref. 92, “Every good model starts from a question. The modeler should always choose the correct level of detail to answer the question.” This is clearly true for the derivation of analytical dispersion relations but also applies to numerical simulations.

This section is organized as follows. The principles of the derivation of fluid dispersion relations in the context of  $\mathbf{E} \times \mathbf{B}$  plasmas are described in Subsection III A. The derivation of kinetic dispersion relations is only briefly discussed in Subsection III B. The kinetic dispersion relation of an  $\mathbf{E} \times \mathbf{B}$  plasma in the conditions of a Hall thruster, leading to the electron cyclotron drift instability will be illustrated in Sec. V. In Subsection III C, we recall the basic principles of Particle-In-Cell Monte Carlo Collisions (PIC-MCC) simulations that are often used to study  $\mathbf{E} \times \mathbf{B}$  plasmas and their instabilities. Finally, Subsection III D

shows some examples of instabilities predicted by PIC-MCC simulations and that can be understood on the basis of fluid dispersion relations.

### A. Theoretical description of instabilities—Fluid dispersion relations

In this section, we describe some aspects of the derivation of the fluid dispersion relations of a low-temperature partially magnetized  $\mathbf{E} \times \mathbf{B}$  plasmas based on Refs. 2 and 93–95. We use the notations of Fig. 1, where  $\mathbf{E}$  is in the  $x$  direction,  $\mathbf{B}$  in the  $z$  direction, and  $\mathbf{E} \times \mathbf{B}$  in the  $-y$  direction. The plasma density gradient is parallel to the electric field, in the  $x$  direction.

We first write the electron and ion continuity and momentum equations assuming quasineutrality, constant electron temperature, collisionless electrons and ions, non-magnetized ions, and we neglect the ion pressure term and the electron inertia terms. We will also neglect the electron and ion mean velocities parallel to the electric field and consider purely azimuthal perturbations. This gives, for ions,

$$\frac{\partial n}{\partial t} + \nabla \cdot (n\mathbf{v}_i) = 0, \tag{11}$$

$$\frac{\partial \mathbf{v}_i}{\partial t} + (\mathbf{v}_i \cdot \nabla)\mathbf{v}_i = -\frac{e}{M}\nabla\phi, \tag{12}$$

and for electrons

$$\frac{\partial n}{\partial t} + \nabla \cdot (n\mathbf{v}_e) = 0, \tag{13}$$

$$n\mathbf{v}_e = n\mathbf{v}_E + n\mathbf{v}_{Pe}, \tag{14}$$

with  $\mathbf{v}_E = \frac{\mathbf{E} \times \mathbf{B}}{B^2} = -\frac{\nabla\phi \times \mathbf{B}}{B^2}$ , and  $\mathbf{v}_{Pe} = \frac{\nabla(nT_e) \times \mathbf{B}}{B^2}$

If we assume a uniform magnetic field, and since  $\nabla \times \mathbf{E} = 0$  and  $\nabla \times \mathbf{B} = 0$ , Eq. (13) can be written as

$$\frac{\partial n}{\partial t} + \mathbf{v}_E \cdot \nabla n = 0. \tag{15}$$

We now consider small wave perturbations in the  $\mathbf{E} \times \mathbf{B}$  direction and linearize the equations above for  $n$  and  $\phi$  around the equilibrium solutions  $n_0, \phi_0$ . As said above and shown in Fig. 1, we consider a situation where the equilibrium electric field  $\mathbf{E}_0$  and density gradient  $\nabla n_0$  are in the  $x$  direction. Since we consider purely azimuthal fluctuations, the axial electric field and density gradient are supposed to be constant and depend on the discharge conditions. In this approximation, only the azimuthal electric field and azimuthal density gradient fluctuate. Note that the axial electric field is related to the electron conductivity which may depend on the azimuthal fluctuations. Using the same notations as in Smolyakov *et al.*,<sup>2</sup> we write

$$\mathbf{E}_0 = E_0\hat{x} = -\frac{\partial\phi_0}{\partial x}\hat{x}; \quad \nabla n_0 = \frac{\partial n_0}{\partial x}\hat{x} = \frac{n_0}{L_n}\hat{x}. \tag{16}$$

$L_n = (\frac{\partial \ln(n_0)}{\partial x})^{-1}$  is a length defining the given axial plasma density gradient and can be positive or negative (see Fig. 1).

The equilibrium  $\mathbf{E} \times \mathbf{B}$  drift and diamagnetic drift are noted  $v_0$  and  $v_*$  and are written [Eqs. (5) and (6)]

$$v_0 = -\frac{E_0}{B} \tag{17}$$

$$v_* = -\frac{1}{B n_0} \frac{\partial n_0 T_e}{\partial x} = -\frac{T_e}{B} \frac{\partial \ln(n_0)}{\partial x} = -\frac{T_e}{B} \frac{1}{L_n}.$$

We look for solutions of Eqs. (11)–(14) above, of the form  $n = n_0 + \tilde{n} \exp(-i\omega t +iky)$ ,  $\phi = \phi_0 + \tilde{\phi} \exp(-i\omega t +iky)$  where  $\omega = \omega_R + i\gamma$  is the complex wave frequency and  $k$  the wavenumber in the  $y$  direction (i.e.,  $k \equiv k_y$ ).  $\omega_R$ , the real part of  $\omega$ , is the wave angular frequency and  $\gamma$ , the imaginary part, is the growth rate. The perturbation grows when  $\gamma > 0$ . In general, the equilibrium and perturbation density,  $n_0$  and  $\tilde{n}$ , are function of the axial ( $x$ ) coordinate, and the full nonlocal theory should be used. For the long-wavelength perturbations,  $(kL_n)^{-1} < 1$ , the local theory can be used, assuming the density gradients constant.

The linearization of Eqs. (11)–(14) for  $\tilde{n} \ll n_0, \tilde{\phi} \ll \phi_0$  is straightforward if one notes that the linearization of the term  $\mathbf{v}_E \cdot \nabla n$  of Eq. (15) gives the first order term  $v_0 \cdot \nabla \tilde{n} + \tilde{\mathbf{v}}_E \cdot \nabla n_0$  where  $\tilde{\mathbf{v}}_E$  has a non-zero component in the  $x$  direction resulting from the  $\mathbf{E} \times \mathbf{B}$  drift related to the field perturbation along  $y$ , i.e.,

$$\mathbf{v}_{E_0} \cdot \nabla \tilde{n} + \tilde{\mathbf{v}}_E \cdot \nabla n_0 = v_0 ik\tilde{n} + ik \frac{\tilde{\phi}}{B} \frac{\partial n_0}{\partial x} = -ik\tilde{n}v_0 - ikn_0v_* \frac{e\tilde{\phi}}{T_e}.$$

The linearization of the equations therefore gives, for ions,

$$\frac{\tilde{n}}{n_0} = \frac{k^2}{\omega^2} \frac{e\tilde{\phi}}{M}, \tag{18}$$

and for electrons

$$\frac{\tilde{n}}{n_0} = -\frac{kv_*}{\omega - kv_0} \frac{e\tilde{\phi}}{T_e}. \tag{19}$$

Combining Eqs. (18) and (19) with the notations

$$\omega_0 = kv_0, \quad \omega_* = kv_*, \quad \frac{eT_e}{M} = c_s^2. \tag{20}$$

( $c_s$  is the ion sound speed), we get the dispersion relation,

$$\frac{k^2 c_s^2}{\omega^2} = \frac{\omega_*}{\omega - \omega_0}. \tag{21}$$

For  $\omega_0 = 0$ , the solution of Eq. (21) is purely real. This corresponds to the stable, anti-drift mode.<sup>2,36,96</sup> The  $(-\omega_0)$  term in the denominator, corresponding to the  $\mathbf{E} \times \mathbf{B}$  flow, is a possible destabilizing term, since, for example, when  $|\omega_0| \gg \omega$  and  $\omega_*/\omega_0 > 0$ ,  $\omega^2$  becomes negative and Eq. (21) has a positive imaginary root ( $\gamma > 0$ ) and the instability grows. This instability, which occurs due to the destabilization of the anti-drift mode by the  $\mathbf{E} \times \mathbf{B}$  electron flow, is called the gradient-drift instability or the collisionless Simon–Hoh instability or the modified Simon–Hoh instability.<sup>35,36</sup> In the collisionless case, the instability is reactive, i.e., the dispersion relation is real, and the complex roots come in complex conjugate pairs. This is an example of negative energy mode in flowing plasmas and fluids when the instability is caused by the coupling of positive and negative energy modes (a plasma wave is said to have negative energy if energy is removed from the plasma when the wave is excited; energy is added to the plasma in the case of a positive energy mode). Negative energy modes may become unstable solely due to dissipation. As discussed by Sakawa and Joshi,<sup>36</sup> the dissipative Simon–Hoh instability was studied by Simon,<sup>97</sup> Hoh,<sup>98</sup> and Thomassen<sup>99</sup> in a weakly ionized, inhomogeneous, collisional, magnetized plasma column and was found to be unstable when the density gradient and electric field were in the same

direction (i.e.,  $\omega_*/\omega_0 > 0$ , as in the collisionless case). An important point in the Simon–Hoh instability is that the  $\mathbf{E} \times \mathbf{B}$  electron drift is much larger than the ion  $\mathbf{E} \times \mathbf{B}$  drift. This difference in electron and ion drift can be due to the weak magnetization of ions or to collisions.

The general solution of the dispersion relation (21) is

$$\omega = \frac{k^2 c_s^2}{2\omega_*} \left( 1 \pm \sqrt{1 - \frac{4\omega_* \omega_0}{k^2 c_s^2}} \right). \quad (22)$$

The condition for instability is that  $\omega$  has a positive imaginary part, i.e.,  $\omega_* \omega_0 > k^2 c_s^2/4$ , which is equivalent to  $v_0 v_* > c_s^2/4$ . This implies that the electric field  $\mathbf{E}_0$  and the density gradient  $\nabla n_0$  are in the same direction ( $\mathbf{E}_0 \cdot \nabla n_0 > 0$ ), and since  $v_0$  and  $v_*$  are generally much larger than  $c_s$ , the condition  $\omega_*/\omega_0 > 0$ , or,  $v_0 v_* > 0$ , or  $\mathbf{E}_0 \cdot \nabla n_0$  is generally sufficient.

Note that in Ref. 36, the effect of the ion velocity  $v_{0i}$  in the  $y$  direction was included, so Eq. (18) for the ion response is modified as follows:

$$\frac{\tilde{n}}{n_0} = \frac{k^2}{(\omega - k v_{0i})^2} \frac{e\tilde{\phi}}{M}, \quad (23)$$

and the corresponding dispersion relation takes the form

$$\omega = k v_{0i} + \frac{k^2 c_s^2}{2\omega_*} \left( 1 \pm \sqrt{1 + \frac{4\omega_*(k v_{0i} - \omega_0)}{k^2 c_s^2}} \right). \quad (24)$$

Therefore, azimuthal ion velocity adds some real part to the frequency and may add some stabilizing or destabilizing effect to the growth rate, depending on the sign of  $\omega_* k v_{0i}$ . This mode was named Modified Simon–Hoh Instability (MSHI) by Sakawa *et al.*<sup>36,100</sup>

Typically, for unmagnetized ions the ion azimuthal drift is neglected. In the case of weak magnetization  $k\rho_i \gg 1$ , the ion drift can be estimated as<sup>100</sup>  $v_{0i} = v_0 I_0 [(k\rho_i)^2] \exp[-(k\rho_i)^2]$  where  $I_0$  is the modified Bessel function (see Sakawa *et al.*<sup>100</sup> for the derivation of this expression, which is valid only in a slab geometry and does not include centrifugal effects).

The dispersion relation (21) has been obtained assuming a uniform magnetic field. One can show<sup>2,93,101</sup> that if the magnetic field is non-uniform, the dispersion relation is modified as

$$\frac{k^2 c_s^2}{\omega^2} = \frac{\omega_* - \omega_D}{\omega - \omega_0 - \omega_D}, \quad (25)$$

where  $\omega_D$  is related to the magnetic field gradient

$$\omega_D = k v_D \quad \text{and} \quad v_D = -2 \frac{T_e}{B} \frac{\partial \ln(B)}{\partial x} = -2 \frac{T_e}{L_D B}. \quad (26)$$

$L_D = (\frac{\partial \ln(B)}{\partial x})^{-1}$  defines the characteristic length of the magnetic field gradient and can be positive or negative.

The condition for a Simon–Hoh instability in the presence of a magnetic field gradient is then  $(\omega_* - \omega_D)/(\omega_0 + \omega_D) > 0$ , which can also be written, if  $|\omega_D| \ll |\omega_0|$

$$\mathbf{E}_0 \cdot \nabla \frac{n_0}{B^2} > 0. \quad (27)$$

The magnetic field gradient effects enter the dispersion relation via the compressibility of the transverse electron drifts

$$\nabla \cdot \mathbf{v}_E = -2v_E \cdot \nabla \ln(B_0), \quad (28)$$

$$\nabla \cdot (n \mathbf{v}_{pe}) = -2n v_{pe} \cdot \nabla \ln(B_0). \quad (29)$$

These expressions are valid when the plasma current is neglected, i.e., it does not modify the magnetic field and  $\nabla \times \mathbf{B} \rightarrow \mathbf{0}$ . These expressions also show that for a uniform magnetic field, electron temperature gradients and generally electron temperature dynamics are not coupled to the electron density directly (unless the electron temperature changes the density via ionization). For a nonuniform magnetic field, the compressibility of the electron diamagnetic flow in Eq. (29) may involve temperature evolution directly. In that case, the dispersion relation (25) becomes more complex and involve the equilibrium temperature gradients, as described in Frias *et al.*<sup>93</sup> Among other effects, the temperature gradients affect the condition for the instability (27) and may result in the appearance of unstable modes in the direction opposite to the  $\mathbf{E} \times \mathbf{B}$  drift.<sup>93</sup>

Because of the condition (29),  $\nabla \cdot (n \mathbf{v}_{pe}) = \mathbf{0}$  in the case of a uniform magnetic field, the diamagnetic drift does not result in the frequency Doppler shift in the electron dynamics, as it occurs due to the  $\mathbf{E} \times \mathbf{B}$  drift,  $\omega \rightarrow \omega - \omega_0$ , and does not result in additional terms in the Simon–Hoh dispersion relation (24), contrary to the statement in Ref. 102. We note also that the condition  $v_{pe} > v_{Te}$ , obtained in Ref. 102, is equivalent to the condition  $\rho_e > L_n$ , which is not possible in the fluid theory but requires a full kinetic treatment.

The derivation of the dispersion relations (21) and (25) was made neglecting the inertia terms in the electron momentum equation. Also, the approach based on the standard momentum equation assuming scalar pressure cannot describe situations where the wavelength of the instability becomes close to the electron Larmor radius (i.e., when  $k^2 \rho_e^2 \gg 1$ ) and a kinetic approach is necessary.

An alternative approach is to describe, in a more general electron momentum balance equation including the viscosity tensor, the finite Larmor radius (FLR) effects via the electron gyroviscosity.<sup>2</sup> This was shown to provide qualitatively correct behavior for  $k^2 \rho_e^2 \gg 1$ .<sup>103</sup> Here we will simply write the dispersion relation obtained with this approach and refer to Ref. 2 for a complete derivation of the inertia and gyroviscosity contributions to this relation. In the absence of magnetic field gradient, this equation writes<sup>2</sup>

$$k^2 \lambda_{De}^2 + \frac{\omega_* + k^2 \rho_e^2 (\omega - \omega_0 + i\nu_{en})}{\omega - \omega_0 + k^2 \rho_e^2 (\omega - \omega_0 + i\nu_{en})} = \frac{k^2 c_s^2}{\omega^2}. \quad (30)$$

The term  $k^2 \lambda_{De}^2$  in the left-hand side of Eq. (30) accounts for finite Debye length effects and can be neglected if  $\lambda_{De}^2 \ll \rho_e^2$ . The right-hand side of Eq. (30) can also be written as follows:

$$\frac{k^2 c_s^2}{\omega^2} = k^2 \rho_e^2 \frac{\omega_{LH}^2}{\omega^2}, \quad \text{with} \quad \omega_{LH} = \frac{c_s}{\rho_e} = \sqrt{\omega_{ce} \omega_{ci}}.$$

$\omega_{LH}$  is the lower-hybrid-frequency.

In the presence of a magnetic field gradient, the dispersion relation (30) must be modified as described by Lakhin *et al.*<sup>95</sup> in Eq. (5) of this reference, where the Debye length term and the electron collision frequency term are neglected. Including these terms, Eq. (30) becomes

$$k^2 \lambda_{De}^2 + \frac{\omega_* - \omega_D + k^2 \rho_e^2 (\omega - \omega_0 - 2\omega_D + i\nu_{en})}{\omega - \omega_0 - \omega_D + k^2 \rho_e^2 (\omega - \omega_0 - 2\omega_D + i\nu_{en})} = \frac{k^2 c_s^2}{\omega^2}. \quad (31)$$

Note that the dispersion relation with magnetic field of Ref. 2 [Eq. (34) of this reference] is missing the higher order terms in  $k^2 \rho_e^2 \omega_D$  and is less accurate than Eq. (31).

The dispersion relations (30) and (31) can be considered as a high frequency, small wavelength, and collisional extension of the collisionless Simon–Hoh or gradient-drift dispersion relation (21). The  $k^2 \rho_e^2$  term on the numerator of Eq. (30) comes from the inertia term in the electron momentum equation, while the same term on the denominator comes from the gyroviscosity. If the gyroviscosity term is omitted and assuming uniform magnetic field and quasineutrality, Eq. (30) is modified into

$$\frac{-\omega_* + k^2 \rho_e^2 (\omega - \omega_0 + i\nu_{en})}{\omega - \omega_0 + i\nu_{en}} = \frac{k^2 c_s^2}{\omega^2}. \quad (32)$$

In the collisionless limit, Eq. (32) is equivalent to

$$\frac{\omega^2}{\omega_{LH}^2} = 1 - \frac{\omega_*}{(\omega - \omega_0) k^2 \rho_e^2}. \quad (33)$$

This equation illustrates the transition from the collisionless Simon–Hoh mode to the lower-hybrid mode. For small values of  $k\rho_e$ , i.e., for long wavelengths, Eq. (33) gives the collisionless Simon–Hoh dispersion relation (21), while it tends to the basic lower-hybrid mode,  $\omega = \pm\omega_{LH}$  when  $k^2 \rho_e^2 |\omega_0/\omega_*|$  is sufficiently larger than 1 (assuming  $\omega \ll |\omega_0|$ ). The dispersion relation Eq. (30) can, therefore, be also considered as a lower-hybrid mode destabilized by  $E \times B$  flow, density gradient and collisions. If the diamagnetic drift is zero,  $\omega_* = 0$ , and assuming  $|\omega_0| \gg \omega$  and  $\nu_{en} \ll \omega$ , the dispersion relation (32) becomes

$$\omega = \pm\omega_{LH} \left( 1 + \frac{i\nu_{en}}{2\omega_0} \right). \quad (34)$$

This is the “resistive mode” of Ref. 104, which can be considered as a lower-hybrid mode destabilized by  $E \times B$  drift and collisions only, and is another example of a negative energy mode destabilized by collisional dissipation.

For very large values of  $k\rho_e$ , the general form of Eq. (30) gives the ion sound mode  $\omega = kc_s$  or  $\omega = kc_s/\sqrt{1 + k^2 \lambda_{De}^2}$  for finite Debye lengths.

Note that Eq. (30) can be written in dimensionless units where the frequencies are normalized by  $\omega_{LH}$ , the lengths are normalized by  $\rho_e$ , and the velocities are normalized by  $c_s$ . If we write  $\Omega = \omega/\omega_{LH}$ ,  $K = k\rho_e$ , the roots  $\Omega(K)$  of Eq. (30) depend on three parameters:  $V_0 = v_0/c_s$ ,  $V_* = v_*/c_s$ , and  $N_{en} = \nu_{en}/\omega_{LH}$ . If finite Debye length is taken into account, another parameter is  $\lambda_{De}/\rho_e$  (or, equivalently,  $\omega_{ce}/\omega_{pe}$ ).

We show in Figs. 9 and 10 some examples of solutions  $\Omega(K)$  of the dispersion relation (30) for different values of  $V_0$  and  $V_*$ , with  $\nu_{en}/\omega_{LH} = 6.23$  and  $\lambda_{De}/\rho_e = \omega_{ce}/\omega_{pe} = 0.16$  and a uniform magnetic field. In Fig. 9, the dimensionless diamagnetic drift velocity  $V_*$  is fixed and the  $E \times B$  drift velocity  $V_0$  is varied. In Fig. 10,  $V_0$  is fixed and  $V_*$  is varied. The corresponding numerical values of  $E_0$ ,  $L_n$ , and other parameters are given in the figure captions, for a particular case corresponding to argon, a magnetic field intensity of 50 mT, and an electron temperature  $T_e = 5$  eV.

We see in Fig. 9 that the maximum growth rate is obtained for decreasing values of the wave number, i.e., increasing wavelength,

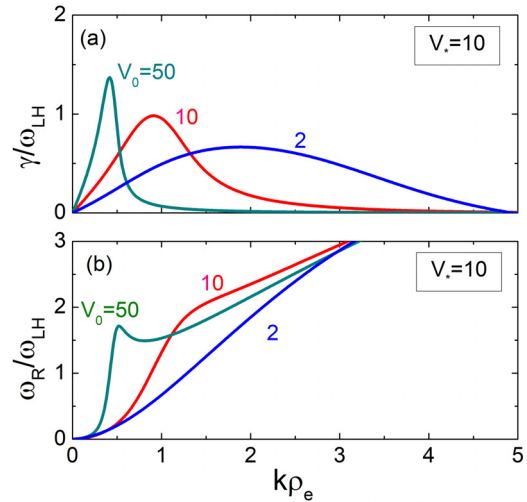


**FIG. 9.** (a) growth rate and (b) angular frequency normalized to the lower-hybrid frequency, as a function of  $k\rho_e$  for a fixed dimensionless diamagnetic drift velocity  $V_* = 10$ , and for three values of the dimensionless  $E \times B$  drift velocity,  $V_0 = 2, 10, 50$ . The dimensionless collision frequency and Debye length are fixed to  $\nu_{en}/\omega_{LH} = 6.23$  and  $\lambda_{De}/\rho_e = 0.16$ . The magnetic field is uniform ( $\omega_D = 0$ ). Numerically, these curves can correspond to argon, with a magnetic field intensity  $B = 5$  mT, an electron temperature  $T_e = 5$  eV, and a plasma density  $n = 10^{16} \text{ m}^{-3}$ . In these conditions,  $\omega_{LH} = 3.2 \times 10^5$  rad/s,  $c_s = 3.46 \times 10^3$  m/s,  $\rho_e = 1.1$  mm, and  $\nu_{en} = 2 \times 10^7$ ,  $\lambda_{De} = 0.17$  mm.  $V_* = 10$  corresponds to  $v_* = 3.5 \times 10^4$  m/s and  $L_n = 2.89$  cm.  $V_0 = 2, 10, 50$  correspond, respectively, to  $v_0 = 6.9 \times 10^3, 3.46 \times 10^4$  and  $1.73 \times 10^5$  m/s, and  $E_0 = 35, 173,$  and  $865$  V/m.

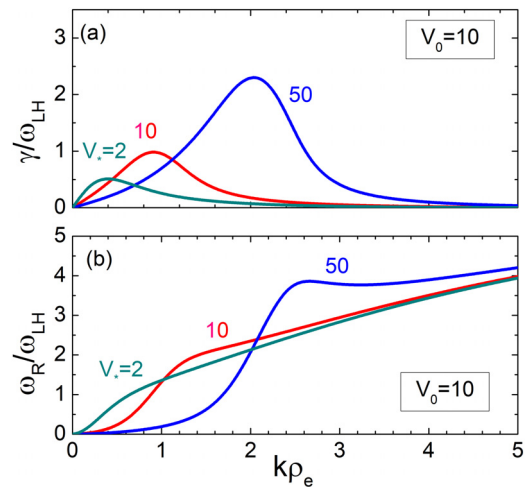


**FIG. 10.** (a) Growth rate and (b) angular frequency normalized to the lower-hybrid frequency, as a function of  $k\rho_e$  for a fixed dimensionless  $E \times B$  drift velocity  $V_0 = 10$ , and for three values of the dimensionless diamagnetic drift velocity,  $V_* = 2, 10, 50$ . The dimensionless collision frequency and Debye length are, as in Fig. 9, fixed to  $\nu_{en}/\omega_{LH} = 6.23$  and  $\lambda_{De}/\rho_e = 0.16$ , and the magnetic field is uniform ( $\omega_D = 0$ ). The numerical example is the same as in Fig. 9: argon,  $B = 50$  mT,  $T_e = 5$  eV,  $n = 10^{16} \text{ m}^{-3}$ , giving  $\omega_{LH} = 3.2 \times 10^6$  rad/s,  $c_s = 3.46 \times 10^3$  m/s,  $\rho_e = 1.1$  mm, and  $\nu_{en} = 2 \times 10^7$ ,  $\lambda_{De} = 0.17$  mm.  $V_0 = 10$  corresponds to  $v_0 = 3.5 \times 10^4$  m/s and  $E_0 = 173$  V/m.  $V_* = 2, 10,$  and  $50$  correspond, respectively, to  $v_* = 6.9 \times 10^3, 3.46 \times 10^4$  and  $1.73 \times 10^5$  m/s, and  $L_n = 14.4, 2.89,$  and  $0.58$  cm.

when  $V_0$  increases at constant  $V_*$ . It is equivalent to say that the wavenumber at maximum growth rate increases with the electric field  $E_0$  for a constant plasma density gradient defined by  $L_n$ . In Fig. 10, the wavenumber at maximum growth rate decreases with decreasing diamagnetic drift at constant  $E \times B$  drift. Long wavelengths are, therefore, obtained for low values of the diamagnetic drift or large values of the  $E \times B$  drift. At the limit of zero density gradient or zero diamagnetic drift ( $|L_n| \rightarrow \infty$  or  $V_* = 0$ ), the lower-hybrid mode is destabilized by  $E \times B$  drift and collisions only, in coherence with the simplified relation (34).

From the general dispersion relation (30), one can calculate, for each value of  $V_0$  and  $V_*$ , the maximum growth rate  $\gamma_{\max}$ , the wave angular frequency at the maximum growth rate,  $\omega_{R,\gamma_{\max}}$ , and the wavenumber  $k_{\gamma_{\max}}$  at the maximum growth rate, or the wavelength  $\lambda_{\gamma_{\max}}$  at maximum growth rate. The corresponding dimensionless values,  $\gamma_{\max}/\omega_{LH}$ ,  $\omega_{R,\gamma_{\max}}/\omega_{LH}$ , and  $\lambda_{\gamma_{\max}}/\rho_e$  are displayed in the form of contour plots as a function of  $V_0$  and  $V_*$ , in Fig. 11 (similar plots were presented in Ref. 105). On each of these plots, the Simon–Hoh or gradient drift instability is obtained in the lower right part of the figure (long wavelengths, lower angular frequencies) and the lower hybrid mode in the upper left part (shorter wavelengths, higher frequencies). The resistive mode is obtained for  $V_* \rightarrow 0$  (not seen on the plots because of the log scale), while the lower-hybrid mode destabilized by density gradient and collisions is obtained for  $V_0 \rightarrow 0$ .

The instabilities discussed in this section are closely related to Farley–Buneman and gradient-drift instabilities in ionospheric plasmas.<sup>106</sup>

The dispersion relations above have been obtained assuming perturbations in the  $\gamma(E \times B)$  direction only. More comprehensive treatment of the fluid dispersion relations in low-temperature partially magnetized  $E \times B$  plasmas can be found in the literature, which consider effects such as electron or ion flow in the  $x$  direction,<sup>93</sup> electron temperature perturbations,<sup>93</sup> sheath effects,<sup>107</sup> etc.

Finally, as mentioned in the introduction of this section; dispersion relations give information on the development of the instabilities in the linear stage only. Analyzing the growth of the instability and the saturation mechanisms is more challenging and requires the use of full fluid or kinetic models. Examples of fluid description of the evolution of the instabilities based on the BOUT++ code<sup>108</sup> can be found in Refs. 2 and 109.

### B. Kinetic dispersion relations

The derivation of the fluid dispersion relations above shows the important role of plasma density gradient and magnetic field gradient in the development of instabilities in  $E \times B$  plasmas. Simulations show that instabilities can also develop in the absence of plasma density and magnetic field gradients in low-temperature partially magnetized  $E \times B$  plasmas. These are very large wavenumber modes corresponding to wavelengths close to the electron gyroradius. In these conditions, the description of the instability must take into account the electron cyclotron orbits and requires a kinetic treatment. The dispersion relation in that case is obtained from the linearization of the Vlasov equation for electrons and of the continuity and momentum equations of the unmagnetized ions (same as in Subsection III A).

The full derivation of the kinetic dispersion relation of low-temperature  $E \times B$  partially magnetized plasmas is beyond the scope of this tutorial. We refer to Refs. 110–116 and references therein for

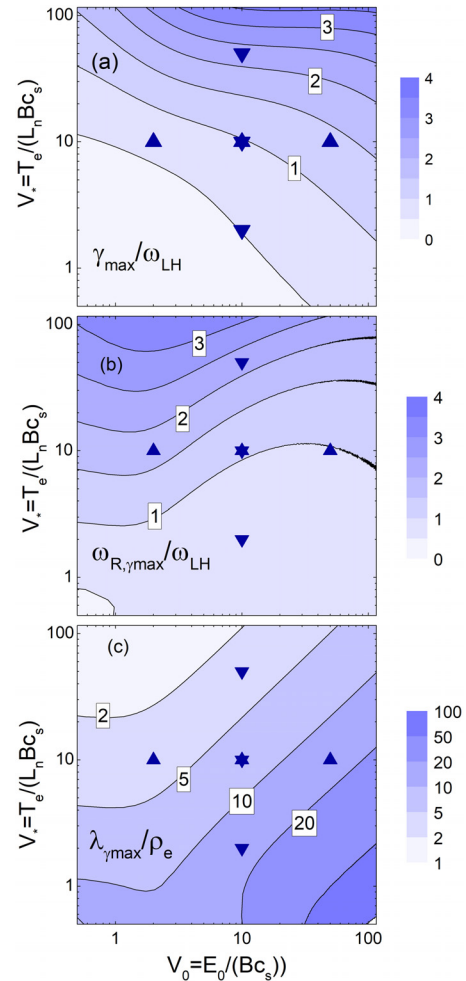


**FIG. 11.** Contour plots of dimensionless: (a) maximum growth rate,  $\gamma_{\max}/\omega_{LH}$  (b), angular frequency at the maximum growth rate,  $\omega_{R,\gamma_{\max}}/\omega_{LH}$ , and (c), wavelength  $\lambda_{\gamma_{\max}}/\rho_e$  at the maximum growth rate as a function of normalized  $E \times B$  drift  $V_0$ , and diamagnetic drift  $V_*$ , calculated from the dispersion relation (30). The dimensionless collision frequency and Debye length are fixed to  $\nu_{en}/\omega_{LH} = 6.23$  and  $\lambda_{De}/\rho_e = 0.16$  (as in Figs. 9 and 10), and the magnetic field is uniform ( $\omega_D = 0$ ). The up triangle symbols correspond to the three cases of Fig. 9 ( $V_* = 10$  with  $V_0 = 2, 10,$  and  $50$ ) and the down triangle symbols to the three cases of Fig. 10 ( $V_0 = 10$  with  $V_* = 2, 10,$  and  $50$ ).

this derivation. The expression of this kinetic dispersion relation is given and discussed in Sec. V on instabilities in Hall thrusters.

### C. Particle-In-Cell Monte Carlo Collisions simulations

In Particle-In-Cell Monte Carlo Collisions (PIC-MCC) simulations, the trajectories of a large representative number of particles (superparticles) are followed in phase space under the influence of the electric forces due to the self-consistent electric field and external magnetic field, and of collisions. The electric field is calculated at each time step from the charged particle densities on this grid, deduced from the positions of the superparticles. The electric forces are then calculated on the grid and the equations of motion of the superparticles are

integrated over time. A Monte Carlo module is used to decide which particles are undergoing collisions during the time step, the nature of the collisions, the change in velocity, etc. We will not discuss here in detail the principles of PIC-MCC and simply refer to standard text books<sup>117,118</sup> and review papers.<sup>119–122</sup> Three-dimensional particle models are still very computationally intensive, especially if one wants to resolve the large plasma frequencies, small Debye lengths, and long time to reach steady-state of Hall thrusters or magnetron discharges. Most of the particle simulations of the  $E \times B$  plasmas of Hall thrusters and magnetron discharges have been performed with 1D3V or 2D3V models, i.e., one or two dimensions in space, three dimensions in velocity, and we will limit our discussion of this article to these models (we note also the recent attempts at reducing the computational cost of 2D PIC simulations of Hall thrusters by introducing the concept of pseudo-2D PIC scheme<sup>123,124</sup>). As said above, the dominant instabilities develop in the azimuthal direction because of the large difference between electron and ion drift velocities in this direction. Therefore, the 1D and 2D models must include the azimuthal direction. The 1D models are purely azimuthal, and the 2D models can be axial–azimuthal or radial–azimuthal. This will be illustrated in Secs. V and VI.

#### D. Example of evidence for rotating instabilities in $E \times B$ plasma devices

The aim of this subsection is to show a few examples of evidence for the presence of rotating azimuthal instabilities in low-temperature partially magnetized plasmas, drawn from simulations, and which illustrate the predictions of the fluid dispersion derived above. In particular, we will see examples where PIC MCC simulations predict the formation of long wavelength Simon–Hoh instabilities due to density gradient and electric field being in the same direction, and small-scale lower hybrid instabilities driven by density gradient and electron–neutral collisions. The general context are the experiments of Raitsev *et al.*<sup>125,126</sup> on a Penning discharge, but the conditions of the simulations are not necessarily close to those of the experiments. A discussion of instabilities under conditions closer to a real device will be given in Secs. IV–VI, with the example of Hall thrusters and magnetron discharges.

We start with the Penning discharge schematically represented in Fig. 12. The principles and conditions of operation of this discharge are indicated in the caption to Fig. 12. In these conditions, rotating plasma non-uniformities (“spokes”) in a plane perpendicular to the magnetic field are observed in the experiments with both fast imaging techniques (CCD camera) and Langmuir probes measurements. Rotating spokes have been observed in many other  $E \times B$  plasma devices including standard Hall thrusters,<sup>129–133</sup> cylindrical Hall thrusters,<sup>134</sup> wall-less Hall thrusters,<sup>135</sup> anode layer Hall thrusters,<sup>136,137</sup> low power dc or rf as well as high power pulsed magnetron discharges,<sup>138–145</sup> and, of course in magnetized plasma columns dedicated to the study of turbulent phenomena.<sup>37–39,146,147</sup>

A number of articles have also been devoted to modeling and simulation of rotating spokes in recent years, with kinetic approaches (Particle-In-Cell Monte Carlo Collisions, PIC-MCC)<sup>26,105,127,128,148–154</sup> or fluid<sup>155</sup> and hybrid fluid–particle simulations.<sup>156–158</sup> An example of results of particle simulations of the Penning discharge of Fig. 12 is shown in Fig. 13 while Fig. 15 displays some high-speed camera images of a rotating spoke in a wall-less Hall thruster.<sup>135</sup>

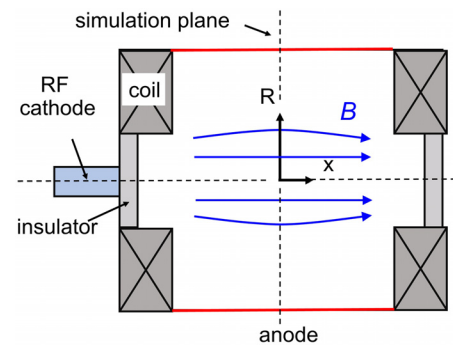


**FIG. 12.** Schematic of the Penning discharge in the PIC-MCC simulations of Carlsson *et al.*<sup>127</sup> and Powis *et al.*<sup>128</sup> (some results are shown in Figs. 13 and 14). The simulations are aimed at modeling the Penning discharge experiment of Raitsev *et al.*<sup>125,126</sup> where electrons are injected by a radio frequency plasma cathode around the discharge axis. An axial magnetic field is generated by Helmholtz coils. A dc voltage of 20–200 V is applied between the rf cathode and the cylindrical anode. The discharge is operated in xenon at a pressure in the 0.1–1 mTorr range. The anode diameter is 10 cm in the experiments, and the axial length is 40 cm.<sup>128</sup>

Figure 13 shows an example of PIC-MCC simulation results of the Penning discharge of Fig. 12 taken from the article of Powis *et al.*<sup>128</sup> The conditions of the simulations are indicated in the caption to this figure. The figure illustrates the formation of a spoke in argon at 1 mTorr, and its rotation in the  $E \times B$  direction at a velocity at mid-radius of 4.9 km/s. Simulations have also been performed in a purely collisionless situation and compared with this collisional case with self-consistent ionization (in the collisionless case, positive ions are injected in the central region of the discharge).

The main results of the paper by Powis *et al.* can be summarized as follows. The PIC-MCC simulation predicts the formation and rotation of a spoke under both the collisionless and collisional conditions, with similar rotation velocities. Anomalous electron transport to the anode can be analyzed by looking at the time-averaged profiles of the electric field and plasma density. Figure 14 shows the time-averaged radial distribution of the electric potential, radial electric field, and electron density in the collisionless and collisional case. We see that the injection of electrons and the trapping of electrons by the magnetic field tend to lower the potential in the plasma center.

The instability and resulting deformation of the electric potential allow magnetically trapped electrons to reach the anode even in the absence of collisions as well as electrostatically trapped ions to flow to the anode (no axial losses are taken into account in the simulation). The fact that the plasma density gradient and electric field are in the same direction suggests that the conditions necessary for a Simon–Hoh or gradient-drift instability, as described in Subsection III A, are met. The scaling of the rotational frequency deduced from the PIC-MCC simulation was compared with the scaling given by the dispersion relation of the collisionless Simon–Hoh mode [Eqs. (21) and (22) above] and good agreement was found. It was, however, shown in a more recent paper by Tyushev *et al.*<sup>153</sup> that in this cylindrical geometry, the Simon–Hoh dispersion relation must be modified to account for the stationary centrifugal ion rotation with frequency  $\omega_i \approx \sqrt{-eE_r/Mr}$ . The anomalous electron mobility or conductivity can be quantified by writing the expression of the radial mean electron

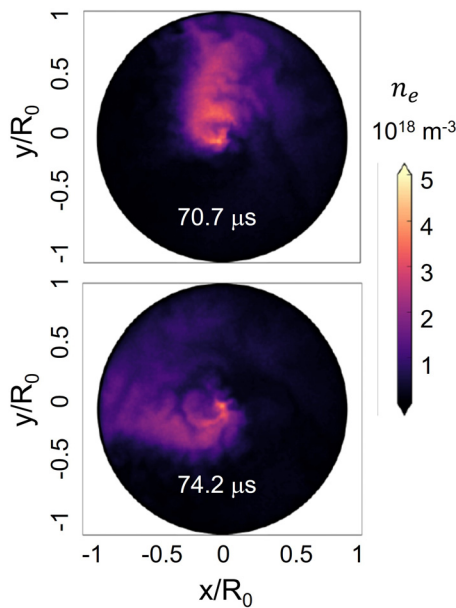


**FIG. 13.** 2D PIC-MCC simulation of the Penning discharge of Fig. 12 in a plane (radial–azimuthal) perpendicular to the magnetic field, showing the space distribution of the electron density at two different times. The anode radius  $R_0$  is 2.5 cm. Electrons are injected in a circular area of radius  $R_i = 0.1$  cm around the discharge axis, with a directed (beam) energy of 15 eV. The applied magnetic field is 10 mT, and the neutral gas pressure is 1 mTorr (293 K). The simulations are performed in a gas with helium mass and approximate cross sections of xenon (electron momentum cross section, no excitation). Ions are collisionless. A pseudo-permittivity  $\epsilon_r = 400$  is used in the simulations. This means that the “real density” simulated is actually 400 times smaller than indicated in the scale of this figure (i.e., the plotted density is actually  $\epsilon_r n_e$  so the maximum “real” density in the simulation is about  $10^{16}$  m $^{-3}$ ), but Coulomb collisions are taken into account for the density indicated in the scale. Adapted with permission from Powis *et al.*, Phys. Plasmas **25**, 072110 (2018). Copyright 2018 AIP Publishing (Fig. 6 of Ref. 128).

velocity, i.e., parallel to the time-averaged electric field. Using the expression derived in Eq. (2), we obtain

$$v_{er} = -\frac{\mu_{e,\text{eff}}}{H_{\text{eff}}^2} \left( E_r + \frac{1}{n} \frac{\partial n T_e}{\partial r} \right). \quad (35)$$

Equation (2) was derived for situations where electron transport across the magnetic field was due to collisions with neutrals. The index “eff” in Eq. (35) indicates that we consider an effective electron collision frequency  $\nu_{\text{eff}}$  to represent the effect of instabilities on cross field transport in the same way as in the purely collisional case.

The effective mobility and Hall parameter  $\mu_{e,\text{eff}} = e/(m\nu_{\text{eff}})$  and  $h_{\text{eff}} = \omega_{ce}/\nu_{\text{eff}}$  are obtained simply by equating the expression (35) of the mean cross field velocity [with  $E_r(r)$  and  $\frac{1}{n} \frac{\partial n}{\partial r}$  from Fig. 14] to the mean velocity deduced from the PIC-MCC simulation (a similar approach was used in Ref. 105). The radially (and time) averaged effective collision frequency calculated by Powis *et al.* in the conditions of Figs. 13 and 14 was on the order of  $10^8$  s $^{-1}$  both in the collisionless and collisional cases. For comparison, the real electron–neutral collision frequency in the collisional case (1 mTorr pressure) was about ten times smaller, indicating that electron cross field transport is also

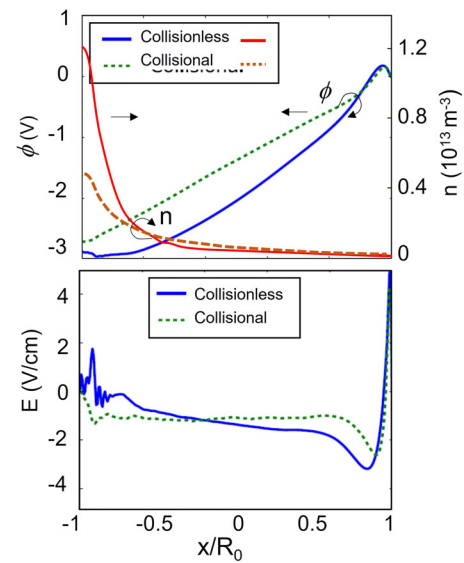


**FIG. 14.** Time-averaged radial profiles of the plasma potential and electron density (top) and electric field (bottom) in the collisionless and collisional cases in the conditions of Fig. 13. Adapted with permission from Powis *et al.*, Phys. Plasmas **25**, 072110 (2018). Copyright 2018 of AIP Publishing (Fig. 7 of Ref. 128).

dominated by fluctuations at 1 mTorr. The calculated effective Hall parameter was between 13 and 16 in both cases.

One of the conclusions of the article by Powis *et al.* is that, since similar rotating spokes are obtained in the Penning discharge model for both collisional and collisionless cases, ionization is not a necessary condition for the existence of spokes. We will see, however, in Sec. IV that under magnetron discharge conditions, ionization may play a major role in the physics of a rotating spoke and that an instability triggered by the Simon–Hoh criterion can evolve into an ionization wave. 3D PIC-MCC simulations<sup>149</sup> performed in the conditions of the wall-less Hall thruster of Fig. 15 also suggest that the rotating spoke can be associated with an ionization wave coupled with a periodic depletion of the neutral atom density (breathing mode, see Subsection III A).

Tyushev *et al.*<sup>153</sup> studied a Penning discharge under conditions similar to those of Powis *et al.*, with collisional electrons and collisionless ions. By varying the power input by the electron beam into the discharge, they could control the radial profile of the time-averaged electric potential.

In the case of a deep potential well, they found a  $m = 1$  spoke regime as in the results of Powis *et al.*,<sup>128</sup> Fig. 13. When the potential profile was flatter, they observed a transition into a rotating small scale spiral arm with  $m \gg 1$ , as illustrated in Fig. 16(a). This is a clear illustration of a transition from a long-wavelength Simon–Hoh instability (spoke), where the instability is triggered by the density gradient and radial electric field being in the same direction, to a small-scale lower hybrid instability driven by density gradient and electron–neutral collisions. Similar conclusions were drawn in Ref. 105, where the 2D PIC-MCC simulation was performed in an axial–azimuthal geometry rather than in a radial–azimuthal geometry. In these simulations, the profile of the electric potential was controlled by the magnetic field intensity.

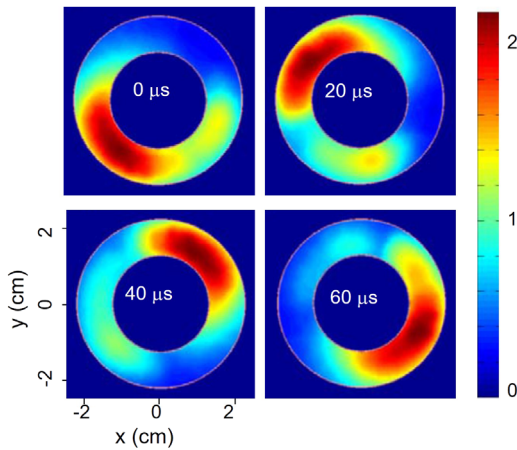


**FIG. 15.** Intensity of the light emitted by a rotating spoke at 4 different times in a wall-less Hall thruster<sup>135</sup> (arbitrary units). The thruster was operated at 110 V applied voltage, 1.3 mg/s xenon mass flow rate, and 1.16 A discharge current. The exposure time of the images was 7.66  $\mu$ s. The images were processed,<sup>135</sup> and a mask was applied to delete the light outside the channel boundaries. The measured velocity of the rotating spoke was 1290 m/s in the  $+E \times B$  direction. Adapted with permission from Mazouffre *et al.*, *Plasma Sources Sci. and Technol.* **28**, 054002 (2019). Copyright 2019 IOP Publishing Ltd. (Fig. 5 from Ref. 135).

An example from this reference is shown in Fig. 16(b) in the conditions of small-scale instabilities. Lucken *et al.*<sup>159</sup> also found the formation of rotating spiral structures with  $m \gg 1$  in 2D PIC-MCC simulations under conditions where the plasma was generated by radio frequency electron heating in the direction parallel to the magnetic field, i.e., perpendicular to the simulation domain. This is illustrated in Fig. 16(c).

In all three models,<sup>105,153,159</sup> the effective Hall parameter was found to decrease, i.e., the anomalous transport was increasing, from the spiral regime (low magnetic field or quasi-flat electric potential) to the spoke regime (larger magnetic field or deeper potential well), with a saturation at large magnetic field in Refs. 105 and 159.

#### IV. PHYSICS OF HALL THRUSTERS AND MAGNETRON DISCHARGES

In this section, we describe in more details the physics and instabilities of two important  $E \times B$  plasma devices, the Hall thruster and the magnetron discharge.

##### A. Hall thrusters

The plasma of a Hall thruster (Fig. 17) is generated in a channel between two concentric dielectric cylinders. The anode is at one end of the channel. Xenon (or krypton) is injected through the anode. An electron emissive cathode is placed outside the channel exhaust. A radial magnetic field, with a maximum (about 20 mT) close to the exhaust plane, is generated by coils or magnets and a magnetic circuit. A voltage of 300 V is applied between cathode and anode under nominal operations. The xenon mass flow rate, and radii of the inner and outer dielectric cylinders are about 5 mg/s and 3.5 and 5 cm for a 1 kW thruster. Because of the lowering of the axial electron mobility in the region of maximum magnetic field, the axial electric field in that region is expected to increase.

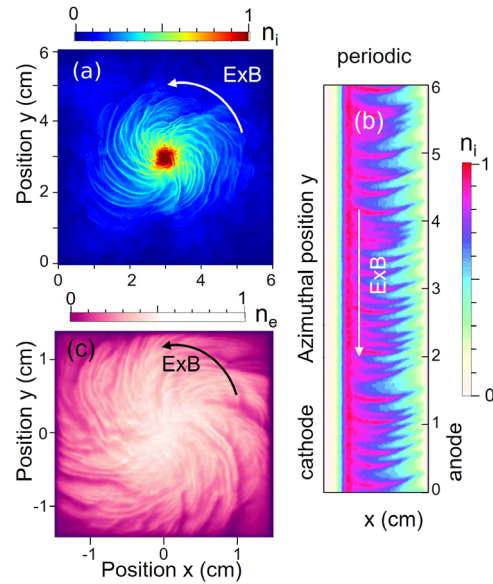


**FIG. 16.** Examples of structures of the plasma density characteristics of a lower-hybrid instability destabilized by density gradient and collisions, obtained in 2D PIC-MCC simulations. The magnetic field is perpendicular to the simulation domain. (a) spiral structure in an electron beam sustained Penning discharge, radial-azimuthal plane,<sup>153</sup> unit  $5 \times 10^{15} \text{ cm}^{-3}$ , (b) closed-drift discharge between two biased electrodes at low uniform magnetic field<sup>105</sup> (axial-azimuthal plane; the azimuthal direction is vertical), unit  $1.8 \times 10^{16} \text{ cm}^{-3}$ , and (c) discharge sustained by radio frequency electric field perpendicular to the simulation domain, radial-azimuthal plane,<sup>159</sup> unit  $3.3 \times 10^{16} \text{ cm}^{-3}$ . (a) Adapted with permission from Tyushev, *Phys. Plasmas* **30**, 033506 (2023). Copyright 2023 AIP publishing [Fig. 20(a) of Ref. 153]. (b) Adapted with permission from Boeuf, *Phys. Plasmas* **26**, 072113 (2019). Copyright 2019 of AIP Publishing (Fig. 16 of Ref. 105). (c) Adapted with permission from Lucken *et al.*, *Phys. Plasmas* **26**, 070702 (2019). Copyright 2019 AIP Publishing [Fig. 1(b) of Ref. 159].

The purpose of a Hall thruster is to extract ions from a plasma and generate thrust without using biased grids like in usual ion sources, but by creating a large accelerating field within the plasma. The Hall thruster is a very interesting and unique plasma device where a potential drop of several hundred volts can indeed be generated in a quasineutral plasma. The electric field in this potential drop can be as large as 400 V/cm over a distance of about 1 cm, much larger than the Debye length. This is quite remarkable since one could expect the cross field electron mobility to be greatly increased by instabilities and turbulence, leading to a collapse of the electric field.

One thing that helps maintaining a low electron conductivity in the acceleration region and outside the channel is the fact that the flow of neutral atoms coming from the anode side is practically fully ionized by the energetic electrons in the ionization region upstream of the channel exhaust [see the location of the ionization region in Fig. 17(b)].

This has two consequences: (1) the contribution of electron-neutral collisions to cross field transport is reduced (anomalous transport due to instabilities is present but we will see that the effective Hall parameter does not collapse in this region). (2) Since ions are practically collisionless due to almost complete ionization of the gas flow, they can be freely accelerated by the electric field resulting from the



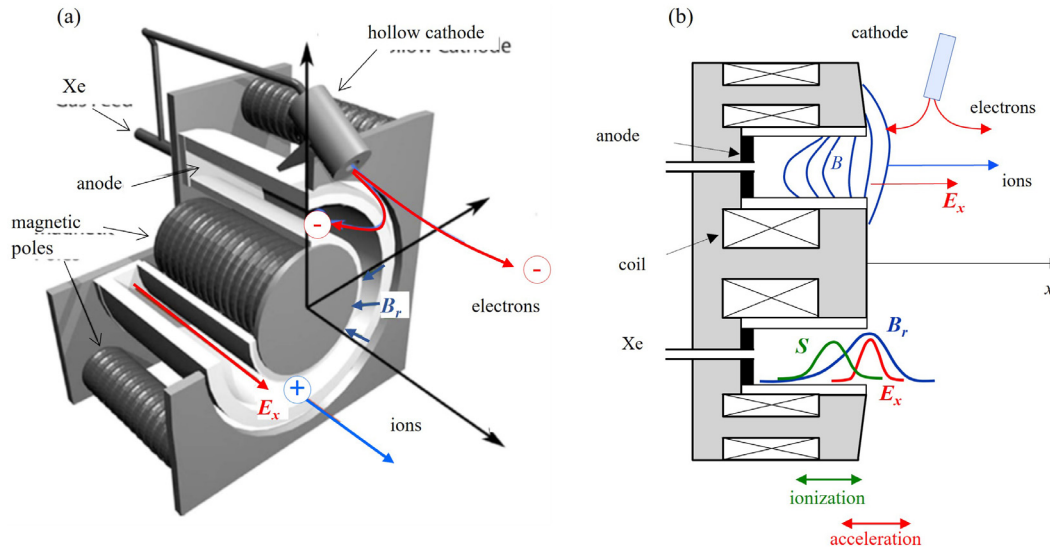


FIG. 17. Schematic of a Hall thruster: (a) 3D view and (b) radial-axial view showing the profiles, in the middle of the channel, of the radial magnetic field  $B_r$ , and of the ionization rate  $S$  and axial electric field  $E_x$  defining the ionization and acceleration zones. Adapted with permission from Boeuf, J. Appl. Phys. **121**, 011101 (2017). Copyright 2017 AIP Publishing (Fig. 5 of Ref. 7).

lowering of the electron conductivity, hence a decrease in the ion density or plasma density and electron conductivity. A larger neutral atom density in the region outside the channel would significantly decrease the mean ion velocity due to charge exchange collisions and thus increase the plasma density leading to an increase in electron conductivity and a collapse of the electric field. Nevertheless, there are some instabilities that increase the electron cross field transport, and this is very difficult to quantify. An example of experimental evidence of the presence of instabilities responsible for anomalous electron transport is shown in Fig. 18 where the inverse effective Hall parameter,  $h_{\text{eff}}^{-1}$ , deduced from different measurements of plasma parameters, is compared with the inverse Hall parameter calculated for electron-neutral collisions only.  $h_{\text{eff}}^{-1}$  is deduced from indirect estimations of the effective electron mobility  $\mu_{e,\text{eff}}$  based on measurements of the axial electric field  $E_x$ , electron current density  $J_{ex}$  and electron density  $n_e$ ,

$$h_{\text{eff}}^{-1} = \mu_{e,\text{eff}} B_r = \frac{J_{ex}}{en_e E_x} B_r. \quad (36)$$

The inverse Hall parameter due to electron-neutral collisions,  $h^{-1} = \nu_{en}/\omega_{ce}$  is deduced from measurements of the neutral atom density and electron temperature. Although this comparison involves many complex and delicate measurements and the accuracy of the electron mobility obtained in this way is difficult to estimate, there is clear evidence in Fig. 18 that the effective collision frequency is much larger than the electron-neutral frequency. This is especially true close to the exhaust plane where the inverse effective Hall parameter (or effective collision frequency) is larger than the inverse collisional Hall parameter (or electron-collision frequency) by almost two orders of magnitude. In this region, the neutral atom density is very low due to ionization upstream, and cross field electron transport is clearly not due to electron-neutral collisions alone.

Although instabilities certainly play an important role in the enhancement of cross field electron transport in a Hall thruster, they are not the only cause of the larger than expected electron mobility. Electrons interactions with the channel walls also contribute to the increase in electron effective mobility inside the channel. The scattering of fast electrons by the channel walls and the secondary electron emission resulting from this interaction are also important causes of cross field electron transport. The interactions of electrons with the channel walls also have important impact on the electron energy balance in the channel. There is a considerable literature on the effect of electron-wall interactions on the conductivity in Hall thrusters and a discussion of these effects is beyond the scope of this paper. Discussions and references on this question can be found in Kaganovich *et al.*<sup>1</sup>

Controlling the electron conductivity in a Hall thruster is an important issue because the efficiency of the thruster decreases if the electron current entering the channel increases<sup>5,7</sup> (i.e., if the electron

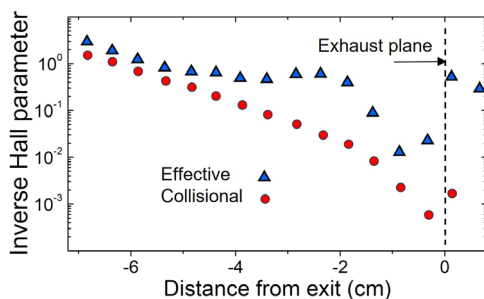
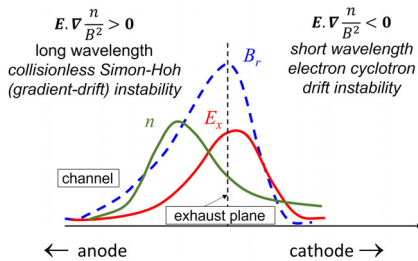


FIG. 18. Effective inverse Hall parameter  $h_{\text{eff}}^{-1} = \mu_{e,\text{eff}} B_r = \nu_{\text{eff}}/\omega_{ce}$  (triangles) deduced from experiments, compared with the inverse classical, collisional Hall parameter  $h^{-1} = \nu_{en}/\omega_{ce}$  (circles) as a function of axial position along the channel. The channel length is 7 cm in this thruster. Adapted with permission from Meezan *et al.*, Phys. Rev. E **63**, 026410 (2001). Copyright 2001 American Physical Society (Fig. 12 of Ref. 160).



**FIG. 19.** Schematic axial profiles of the radial external magnetic field,  $B_r$ , axial electric field,  $E_x$ , and plasma density  $n$  along a line through the mid-channel of a Hall thruster.

conductivity increases in the exhaust region). The operations and performance of a Hall thruster are extremely sensitive to the distribution and axial profile of the radial magnetic field which is still empirically optimized (models with predictive capabilities are not available). This sensitivity is largely due to the fact that the magnetic field intensity profile controls the instabilities and cross field electron transport. For example, the nature of azimuthal instabilities may be different in different parts of the thruster, as illustrated in Fig. 19, which shows schematic axial profiles of the radial magnetic field, axial electric field, and plasma density. The plasma density decreases outside the channel and toward the anode. On the anode side of the thruster, the plasma density and axial electric field are in the same direction. This suggests that long wavelengths instabilities of the Simon-Hoh or gradient-drift type may be present in this region. Rotating spokes have indeed been observed in this region,<sup>130–134,161,162</sup> and their presence depends on the magnetic field intensity. On the cathode side of the maximum magnetic field, the electric field and plasma density gradient are in opposite direction so a gradient-drift instability cannot develop in that region. We will see in Sec. V that a short wavelength kinetic instability, the electron cyclotron drift instability, and a fluid instability, the modified two-stream instability, can be present in the acceleration region of a Hall thruster.

Figure 20 shows the different types of instabilities that can develop in a Hall thruster. Rotating spokes, in the frequency range 5–20 kHz, electron cyclotron drift instabilities around 2–5 MHz and modified two-stream instabilities at 5–10 MHz form in the azimuthal direction and are directly related to the  $E \times B$  configuration, but axial instabilities such as the breathing mode and the ion transit time can also be present and sometimes coupled with the azimuthal fluctuations. An early review of Hall thruster oscillations can be found in Ref. 163. Although progress in understanding these oscillations has been made over the past twenty years and is described in Ref. 1, a fully self-

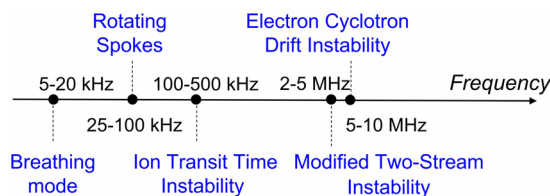


**FIG. 20.** Different types of instabilities occurring in a Hall thruster and their frequencies.

consistent and predictive description of Hall thruster instabilities has yet to be achieved. We briefly summarize these instabilities below, and describe some of them in more details in Sec. V.

The breathing mode is an ionization instability related to a periodic depletion of the neutral density due to strong ionization of the neutral flow. This is one of the most common and most studied instabilities in Hall thrusters.<sup>6</sup> This ionization instability can lead to large amplitude oscillations of the discharge current. The breathing mode is strongly related to the cross field electron transport and to the electron energy balance. Strong ionization by electrons trapped in the large magnetic field region and drifting in the  $E \times B$  direction induces a depletion of the neutral density in the ionization region. The neutral density depletion changes the momentum and energy balance of the electrons, leading to a decrease in electron conductivity and in the current of electron entering the channel. The ionization decreases until the flow of neutral atoms from the anode replenishes the neutral depletion. The oscillation frequency is therefore related to the time necessary for the neutrals to refill the ionization region. This is a low-frequency mode typically in the 5–20 kHz range. This qualitative description actually hides a very complex and non-linear physics that is still under discussion. Excitation of the breathing mode is affected by several interrelated mechanisms that depend in a complex way on the magnetic field configuration and are not easily quantifiable. These mechanisms include electron momentum and energy losses to the walls, anomalous electron transport, ion backflow and recombination on the walls and anode, etc. Attempts to untangle these complex physical mechanisms have been made in a number of papers based on 1D<sup>164–173</sup> numerical models. A simple 0D predator–prey model has been proposed<sup>165,169,171,174</sup> to describe the ionization–depletion–replenishment process but fails to identify the conditions for the instability. We will not discuss these research efforts further here and we refer to some early or more recent review articles<sup>1,175</sup> and to recently published papers on this subject.<sup>172,173,176</sup>

Under certain conditions, the low-frequency breathing mode coexists with high-frequency oscillations in the range of 100–500 kHz. These high frequency oscillations correspond to the characteristic time-of-flight of ions in the channel and have been evidenced in hybrid Hall thruster models and in experiments.<sup>173,177–184</sup> Using 1D fluid and hybrid models, Chapurin *et al.*<sup>173</sup> identified two distinct regimes of breathing oscillations depending on the assumption on the electron energy losses to the walls. The regime with higher energy losses exhibits a low-frequency mode of about 14 kHz that coexists with high-frequency ion transit time oscillations around 150 kHz. In the second regime with low electron energy losses, pure breathing oscillations are observed.

The higher frequency oscillations of Fig. 20, the electron cyclotron drift instability and the modified two-stream instability will be described in Sec. V.

### B. Magnetron discharges

We have seen in Subsection IIC that in a magnetron discharge, the magnetic field is generated by magnets placed behind the cathode (Fig. 21). This creates a point-cusped magnetic field. Electrons are mirroring at the cusp regions and are also electrostatically confined by the cathode sheath. The plasma forms in the region above the cathode, where the magnetic field is parallel to the cathode. This is an  $E \times B$  configuration with axial electric field and radial magnetic field. The

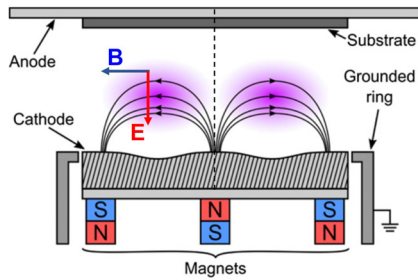


**FIG. 21.** Schematic of a magnetron discharge. Adapted with permission from Gudmundson, *Plasma Sources Sci. Technol.* **29**, 113001 (2020). Copyright 2020 Authors, licensed under a Creative Commons Attribution (CC BY) license (Fig. 2 of Ref.14).

magnetic field intensity decreases from cathode to anode (as in the channel of a Hall thruster). Magnetron discharges can be operated in dc or rf regimes, but also in a pulsed regime with very high-power densities (HiPIMS) at gas pressures below a few Pa. They are used in sputter deposition applications.

The ions are accelerated at high energies toward the target cathode in the quasi-collisionless sheath and sputter atoms from the cathode surface. These atoms then deposit on a substrate, forming a thin layer.

A number of papers report the presence of instabilities in magnetron discharges, which take the form of large-scale plasma non-uniformities rotating in the azimuthal direction and associated with rotating regions of enhanced light emission and ionization. These rotating non-uniformities were first detected in Hall thrusters by Janes and Lowder<sup>185</sup> using Langmuir probes and were called spokes. More recent observations with high speed camera imaging in Hall thrusters<sup>130,133–135,186,187</sup> as well as in magnetron discharges<sup>138,141,142,188–192</sup> have shown that these rotating non-uniformities are associated with a strong light emission.

Interestingly, it has been shown in several articles<sup>142,190,192–194</sup> that the spoke can rotate in the  $-E \times B$  direction in low power dc magnetrons and in the  $+E \times B$  direction in high power pulsed magnetrons used in plasma processing applications (HiPIMS) and in some Hall thrusters, at velocities more than ten times smaller than the  $E \times B$  drift velocity. The images of rotating spokes in a dc magnetron discharge obtained by Panjan and Anders<sup>194</sup> and displayed in Fig. 22 show that the number of spokes increases with gas pressure. Stable

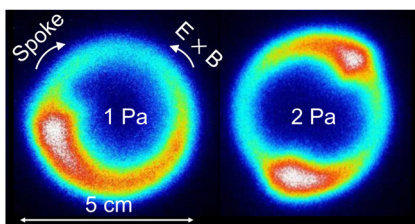


**FIG. 22.** Intensity of the emitted light by rotating spokes in a dc magnetron discharge at two different gas pressures in argon (red-white correspond to maximum luminous emission). The spokes rotate in the  $-E \times B$  direction. Adapted with permission from Panjan *et al.*, *J. Appl. Phys.* **125**, 203303 (2019). Copyright 2019 of AIP (Fig. 4 of Ref. 144).

plasma patterns with four and up to seven spokes were observed by these authors under rf (radio frequency) voltages with self-bias. At high enough pressure, collisional electron transport becomes dominant and the spokes disappear.<sup>195</sup>

An important issue that has been widely discussed in the literature on magnetron discharges<sup>15,139,192,196,197</sup> relates to the electron heating mechanisms leading to the formation of these luminous regions, one conclusion being that electrons are not heated in the cathode sheath as in non-magnetized glow discharges but rather in the presheath, by Ohmic heating.

We will show in Sec. VI that particle simulations provide a new insight in the electron heating mechanisms in the spokes of magnetron discharges.

Space- and time-resolved Langmuir probe measurements of the plasma and floating potentials in dc magnetron discharges by Panjan and Anders<sup>194</sup> have revealed the existence of strong electric fields parallel and perpendicular to the cathode surface, forming a double layer structure at the leading edge of the ionization zone. Figure 23 shows an example of measured plasma potential distribution in a plane-parallel to the cathode and 7.5 mm above it. A sharp drop of the potential of several tens of volts can be seen at the spoke front. The magnetron discharges in Figs. 22 and 23 operate in a low power dc regime, and the spokes rotate in the  $-E \times B$  direction.

These measurements suggest that the double layer at the leading edge of the spoke plays a crucial role in the energization of electrons in the spoke. Held *et al.*<sup>145</sup> measured the plasma potential, electron density, electron temperature, and electron energy probability function (EPEF) with Langmuir probes, as a function of time at a given location above the cathode, on the spoke path.

The sharp increase in the plasma potential when the spoke front reaches the probe, seen in the measurements of Held *et al.*, Fig. 24) is consistent with the 2D potential distribution of Fig. 23 and is associated with a very fast increase and decay of the electron temperature. The electron density presents large amplitude oscillations as a function of time in the spoke region. Held *et al.*<sup>145</sup> also measured the electron energy distribution at different times and observed a fast increase in the tail of this energy distribution at the spoke front, followed by a quick decay. We will see in Sec. V that the particle simulations of magnetron plasma are qualitatively consistent with these measurements.

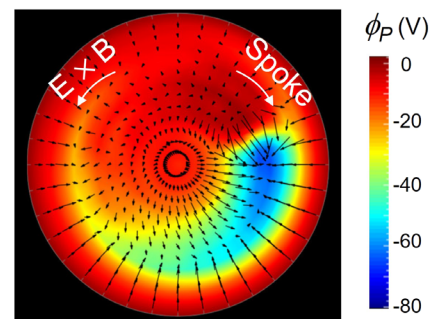


**FIG. 23.** 2D radial-azimuthal distribution of the plasma potential measured by Langmuir probe in a dc magnetron discharge, 7.5 mm above the cathode. Adapted with permission from Panjan and Anders, *J. Appl. Phys.* **121**, 063302 (2017). Copyright 2017 AIP (Fig. 5 of Ref. 194).

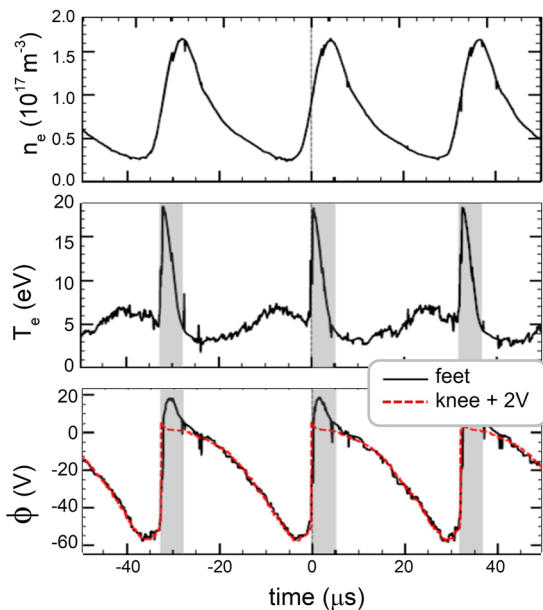


**FIG. 24.** Probe measurements by Held *et al.*<sup>145</sup> of the time evolution of electron density,  $n_e$ , electron temperature,  $T_e$ , and plasma potential  $\phi$  in a dc magnetron discharge in argon, 0.56 Pa pressure and applied dc voltage 255 V. The probe is located 6 mm above the cathode surface, on the spoke path. The gray areas indicate positions where the validity of the electron temperature and plasma potential are in question. Reproduced from Held *et al.*, *Plasma Sources Sci. Technol.* **31**, 085013 (2022). Copyright 2020 Authors, licensed under a Creative Commons Attribution (CC BY) license (Fig. 6 of Ref. 145).

## V. MICROSCOPIC (KINETIC) INSTABILITIES IN HALL THRUSTERS

Hall thrusters and other  $E \times B$  plasma devices are complex because of the different non-linear and coupled physical mechanisms involved (instabilities, ionization, neutral depletion, and other interaction of charged particles with the neutral gas). As discussed in the introduction of Sec. III, rather than trying to deal with the full complexity of the problem it is often useful to simplify or reduce the problem and to decouple some of these mechanisms. This is illustrated in this section with the example of a Hall thruster, where we focus on the electron cyclotron drift instability, a kinetic instability that has been shown to develop in this device.

The existence of the electron cyclotron drift instability (ECDI) in the particle simulations of Hall thrusters has been demonstrated for the first time by Adam *et al.*<sup>198</sup> in 2004 with a 2D PIC-MCC axial-azimuthal model including a fluid description of the neutral atom transport, ionization, and neutral atom depletion. The model was able to describe the azimuthal ECDI and the breathing mode mentioned above. The ECDI was characterized, in these simulations, by the presence of large amplitude, small wavelengths azimuthal oscillations of the azimuthal electric field, and plasma density in the acceleration region of a Hall thruster. The EDCI was then studied in more details by Ducrocq *et al.*<sup>115,116</sup> with dispersion relations and a simpler 1D PIC-MCC simulation. An analysis and a parameter study of the 3D dispersion relation of the ECDI in Hall thrusters can be found in the paper by Cavalier *et al.*<sup>115</sup> The dispersion relation for the ECDI had

been derived and studied earlier,<sup>110,199–201</sup> in the 1970s, in other contexts such as collisionless shocks in the magnetosphere.

In this section, we consider PIC simulations based on reduced models where the plasma is collisionless. This is a good approximation downstream of the ionization region. The PIC simulations contain the azimuthal direction and, to represent closed-drift, the boundary conditions are periodic in the azimuthal direction. In Subsection V A, the ECDI is described by a 1D PIC simulation in the azimuthal direction. The theory of the ECDI is outlined in Sec. V B. Additional details on the properties of the ECDI in Hall thrusters are discussed in Secs. V C and V D on the basis of 2D axial-azimuthal and radial-azimuthal PIC simulations, respectively. We conclude this section by some remarks on experimental evidence of the presence of the ECDI in Hall thrusters in Subsection V E.

### A. 1D Particle-In-Cell simulations of instabilities in a Hall thruster

In 1D models, the particle simulation is performed in the azimuthal,  $y$  direction (same notations as Fig. 1), i.e., electrons and ion trajectories are followed in the  $y$  direction and the electric field is recalculated at each time step in this direction, with periodic boundary conditions. The axial electric field  $E_0$ , in the  $x$  direction perpendicular to the azimuthal direction of the simulation and to the magnetic field is given and is supposed to be constant.  $E_0$  represents the electric field of the acceleration region of the Hall thruster. The magnetic field intensity  $B$  in the  $z$  direction is also given as constant and represents the radial magnetic field of the Hall thruster. The simulation is collisionless and starts with given Maxwellian velocity distributions of electrons and ions. As the instability forms, anomalous transport across the magnetic field occurs and electrons can gain energy from the axial electric field. Since the electric field is fixed in the direction perpendicular to the direction of the simulation, the electrons constantly gain energy in this direction. In order to limit the electron mean energy, a finite dimension can be assumed in the direction of the electric field. The electron positions in the direction of the applied electric field  $E_0$  can be tracked, and each electron that has traveled a given length along the electric field (the acceleration region) is removed from the simulation and replaced by an electron with the initial velocity distribution.

Figure 25 shows an example of result from a 1D Particle-In-Cell simulation, from Ref. 112. A short wavelength instability develops in the simulated azimuthal direction. An analysis of the wavelength of the instability shows that the azimuthal wavenumber  $k_y$  closely satisfies the relation  $-k_y v_0 = \omega_{ce}$  (cyclotron resonance) where  $v_0 = -E_0/B$  is the azimuthal drift velocity and  $\omega_{ce}$  the cyclotron angular frequency. We can say that the instability is dominated by a  $m = 1$  cyclotron resonance and appears as a quasi-coherent mode. Higher modes with larger growth rates, defined by  $-k_y v_0 = m\omega_{ce}$  and  $m > 1$ , can also be observed during the early stage of the instability and have larger growth rates (see Fig. 27) but the increase in electron temperature and nonlinear inverse cascade make the  $m = 1$  mode dominant in the nonlinear stage. We will see in Subsection V B that the instability observed in the simulation is consistent with the theory defining the electron cyclotron drift instability (ECDI).

We also observe in Fig. 25 the generation of large-scale structures, at the length scale of the simulation box. These long wavelength modes were also seen in Ref. 114. A possible explanation of the presence of large-scale structures is that while the energy input via the resonant

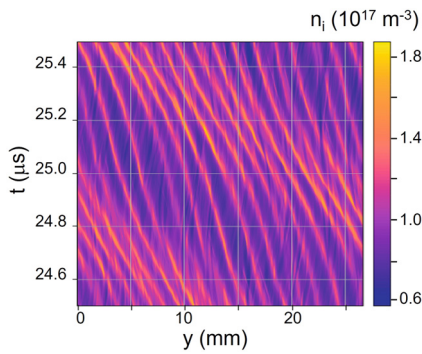


**FIG. 25.** Propagating ion density perturbation around  $t = 25 \mu\text{s}$ , from a 1D PIC-MCC simulation of the azimuthal,  $y$  direction of a Hall thruster, with perpendicular magnetic field  $B = 20 \text{ mT}$  and electric field  $E_0 = 20 \text{ kV/m}$ , and a plasma density  $n = 10^{17} \text{ m}^{-3}$ . Reproduced with permission from Smolyakov *et al.*, Plasma Physics Reports, **46**, 496 (2020). Copyright 2020 Pleiades Publishing, Ltd. (Fig. 3 of Ref. 112).

ECDI occurs at small scales, nonlinear inverse cascade mechanisms may result in energy condensation in large scale structures, as shown in the analytical results of Ref. 202.

In some earlier 1D PIC studies, it was shown that at some finite amplitude, the cyclotron resonances are washed out by nonlinear effects and the instability occurs in the ion sound regime. This is not the case in the simulation results of Fig. 25 where the numerical noise has been reduced by using more than 1000 particles per cell (10 000 particles per cell were used in the 1D simulation of Janhunen *et al.*, with similar results). Similar conclusions were drawn in Ref. 203. It is important to note that numerical collisions due to the inherent numerical noise in particle simulations may also lead to resonance overlap and to the transition to the ion sound regime. Recent simulations with a noise-free Vlasov code<sup>204</sup> have shown that in the 1D case, the nonlinear broadening does not produce the transition to the ion sound and the cyclotron resonances remain most active so that the fluctuations energy is concentrated in the lowest  $m = 1$  resonance and in the lower wavelength (due to the inverse cascade condensation).

This is illustrated in Fig. 26, which shows the frequency spectrum of the azimuthal electric field in the nonlinear regime obtained with a 1D Vlasov simulation of the ECDI (comparisons between Vlasov and PIC simulations of the ECDI are discussed in Ref. 205).

The cyclotron harmonics are clearly pronounced in Fig. 26. Note the backward wave (with positive value of the wavevector) propagating in the direction opposite to the  $\mathbf{E} \times \mathbf{B}$  drift. These waves are usually a result of the strong modification of the electron distribution function due to trapping in high-amplitude potential wells of the electric field (see, e.g., Refs. 206–209). The theory of the ECDI below assumes a Maxwellian electron velocity distribution function and cannot describe this backward wave. A similar feature of the backward waves has also been observed experimentally in the Hall thruster plasma (see Fig. 3 of Ref. 210 and Fig. 4 of Ref. 210).

### B. Theory of the electron cyclotron drift instability

The wavelength of the instability revealed by the PIC simulations above is short, not much larger than the electron Larmor radius. A fluid description of this instability is, therefore, not appropriate, and

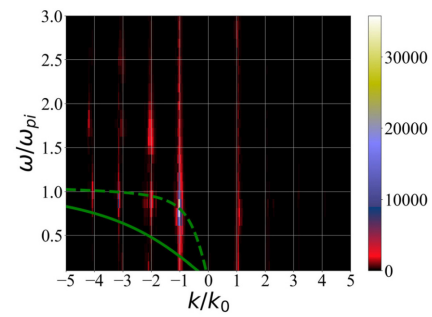


**FIG. 26.** frequency spectrum of the azimuthal electric field (in V/m) in the nonlinear regime, obtained with a noise free Vlasov simulation. The green solid line and the green dashed line show the ion-sound dispersion relation with the initial temperature and large average temperature later in simulations, respectively. Reproduced with permission from Tavassoli *et al.*, Phys. Plasmas **29** 030701 (2022). Copyright 2022 of AIP Publishing (Fig. 4 of Ref. 204).

we must use a kinetic approach obtained from the linearization of the Vlasov and Poisson equations. Here, we will only recall the assumptions leading to this dispersion relation, and its general form. We use the notations of Fig. 1 for the configuration of electric and magnetic field. The wave is supposed to be electrostatic. Ions are assumed to be unmagnetized and cold, with an axial velocity (beam velocity)  $v_{bi}$ . The electron dynamics is described using the Vlasov equation and assuming a Maxwellian velocity distribution at temperature  $T_e$ . The electrons drift azimuthally ( $-y$  direction) in a static axial electric field  $E_0$  ( $x$  direction) and perpendicular magnetic field  $\mathbf{B}$  ( $z$  direction) at a velocity  $v_0 = -E_0/B$ . The drifts due to plasma density and magnetic field gradients are neglected (the  $\mathbf{E} \times \mathbf{B}$  drift velocity  $v_0$  is much larger than the azimuthal drifts due to magnetic field gradient and density gradient in the conditions of Hall thrusters). The electron thermal velocity is noted  $v_{Te}$ . The conditions of the theory are, therefore, very close to those of the 1D PIC simulations of Subsection V A.

The details of the derivation of the kinetic dispersion relation are outside the scope of this tutorial and can be found in Refs. 110–116 and references therein. We just give here the expression of the 3D dispersion relation obtained by linearization of the electron Vlasov equation, ion fluid equations, and Poisson’s equation under the conditions described above,

$$1 - \frac{\omega_{pi}^2}{(\omega - k_x v_{bi})^2} + \frac{1}{k^2 \lambda_{De}^2} \times \left[ 1 + \frac{\Omega}{k_z v_{Te} \sqrt{2}} \sum_{m=-\infty}^{+\infty} Z\left(\frac{\Omega + m\omega_{ce}}{k_z v_{Te} \sqrt{2}}\right) \exp(-b) I_m(b) \right] = 0, \quad (37)$$

$$\text{with } \Omega = \omega - k_y v_0, \quad b = (k_x^2 + k_y^2) \rho_e^2, \quad \omega_{pi} = \left(\frac{e^2 n}{\epsilon_0 M}\right)^{\frac{1}{2}},$$

$$v_{Te} = \left(\frac{e T_e}{m}\right)^{\frac{1}{2}}, \quad k^2 = k_x^2 + k_y^2 + k_z^2.$$

$Z$  is the plasma dispersion function<sup>211</sup> defined by

$$Z(\zeta) = \frac{1}{\sqrt{\pi}} \int_{-\infty}^{\infty} \frac{e^{-t^2}}{t - \zeta} dt, \text{ and } I_m \text{ the modified Bessel function of the first kind.}$$

Some examples of solutions of this dispersion relation are shown in Fig. 27 as a function of the wave number in the azimuthal direction  $k_y$ ,

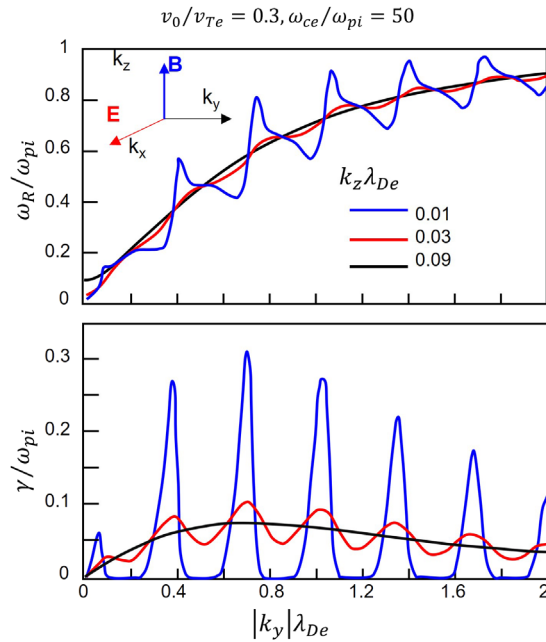


**FIG. 27.** Solutions of the 3D dispersion relation for the electron cyclotron drift instability as a function of the wave number in the azimuthal direction,  $k_y$ , and for three values of the wave number  $k_z$  in the magnetic field direction. The component parallel to the electric field,  $k_x$ , is set to zero.  $\omega_R$  and  $\gamma$  are the angular frequency and the growth rate of the perturbation, respectively.  $v_0$  is the  $E \times B$  drift,  $v_{Te}$  the electron thermal velocity,  $\omega_{pi}$  the ion plasma frequency. The maximum growth rate, around  $k_y \lambda_{De} \approx 0.7$ , corresponds to an azimuthal wavelength  $\lambda = 2\pi/k_y$  on the order of 1 mm in the conditions of a Hall thruster. Adapted with permission from Cavalier *et al.*, Phys. Plasmas **20**, 082107 (2013). Copyright 2013 of AIP Publishing (Fig. 2 of Ref. 113).

for three values of the wave number in the magnetic field direction,  $k_z$ , and for a zero wave number  $k_x$  in the direction of the applied electric field.

We see in Fig. 27 that the angular frequency of the instability at maximum growth rate is slightly below the ion plasma frequency (about  $10^8$  rad/s for xenon and a plasma density of  $10^{18} \text{ m}^{-3}$ , i.e., a wave frequency in the 5–10 MHz range). For a wave vector strictly orthogonal to the magnetic field (which was the case of the 2D PIC-MCC simulation of Adam *et al.*<sup>198</sup>) i.e., for  $k_z = 0$ , instabilities are present only in small intervals in  $k_y$  around each multiple of the inverse Larmor radius of an electron with velocity  $v_0$ , i.e.,  $|k_{y,m}| = m\omega_{ce}/v_0$ , with  $m$  integer.

The dispersion relation for  $k_z = k_x = 0$  can be written as follows<sup>111</sup>

$$k_y^2 \lambda_{De}^2 \left[ 1 - \frac{\omega_{pi}^2}{\omega^2} \right] + 1 - \exp(-b) I_0(b) - 2(\omega - k_y v_0)^2 \sum_{m=1}^{+\infty} \frac{\exp(-b) I_m(b)}{(\omega - k_y v_0)^2 - m^2 \omega_{ce}^2} = 0. \quad (38)$$

For  $k_z = 0$ , Eq. (38) shows that the instability occurs as a reactive mode due to the overlap of the Bernstein modes Doppler shifted by the  $E \times B$  flow with the ion sound mode. In this case, the dispersion

relation is fully real and the instability appears in complex conjugate pairs with the growth rates narrowly peaked around the cyclotron resonances at  $-k_y = m\omega_{ce}/v_0$  (with  $m = 1, 2, 3, \dots$ ).

For finite but small  $k_z$ , the instability still appears as a sequence of narrowly spaced resonant peaks, the cyclotron resonances, as can be seen in Fig. 27 (blue curves). With increasing  $k_z$ , the instability gradually changes to the dissipative mode driven by inverse Landau damping on the electrons. For larger values of  $k_z$  (red curves of Fig. 27), the resonant peaks overlap and the instability eventually switches into the ion sound unmagnetized plasma regime (black curve of Fig. 27) but driven by the electron  $E \times B$  flow in the  $y$  direction. The transition to the ion sound regime is also possible with  $k_z = 0$  due to collisions and/or nonlinear resonance broadening. It can be shown that the angular frequency and growth rate of this “modified ion acoustic mode” can be written as<sup>113,212–214</sup>

$$\begin{cases} \omega_R = k_x v_{bi} + \frac{kc_s}{(1 + k^2 \lambda_{De}^2)^{1/2}}, \\ \gamma = \sqrt{\frac{\pi m}{8M}} \frac{kv_0}{(1 + k^2 \lambda_{De}^2)^{3/2}}. \end{cases} \quad (39)$$

### C. 2D axial-azimuthal PIC simulation of the ECDI

More realistic, but still reduced models of the ECDI in the context of Hall thrusters based on 2D axial-azimuthal PIC-MCC simulations have also been developed. We present in this subsection some PIC simulations results corresponding to a reduced model defined in Refs. 183 and 215, and which was used in the benchmark simulations of Ref. 217. As in the 1D PIC model of Sec. V A, the aim is to study the ECDI independently of the question of self-consistent ionization and complications related to the ionization instability mentioned above (the breathing mode). Only the ionization region, acceleration region, and a small part of the near plume are simulated in the model. The gas flow is supposed to be fully ionized so the model is purely collisionless. Compared with the 1D model, this 2D reduced model allows to describe self-consistently the formation of the electric field in the acceleration region as well as the effect of the azimuthal instability on cross field electron transport under more realistic conditions.

The principles of the 2D model are shown in Fig. 28. The axial length is 2.5 cm and contains a small part of the channel (generally situated on the left side of the maximum magnetic field  $B$ ), the acceleration region, which is supposed to develop around the maximum magnetic field, and part of the near plume. The profiles of the radial magnetic field  $B(x)$  and of the given ionization rate  $S(x)$  (cosine profile) are shown in Fig. 28. The simulation domain is periodic in the azimuthal direction, with a length of 1.28 cm. In the results shown in Fig. 29, the maximum magnetic field is 10 mT, and the integral of the ionization rate over the axial length corresponds to a current density of  $400 \text{ A/m}^2$  (the current density in standard Hall thrusters<sup>7</sup> is on the order of  $1000 \text{ A/m}^2$ ). To represent the effect of the electron emissive cathode, a flux of electrons is injected on the right side of the simulation domain as described in the caption to Fig. 28 and in Refs. 183 and 216.

Figure 29 shows the axial-azimuthal distribution of the azimuthal electric field and of the ion density obtained with the PIC simulation in the steady-state regime (at a simulation time of  $20 \mu\text{s}$ ). An azimuthal wave moving in the  $E \times B$  direction is observed in the

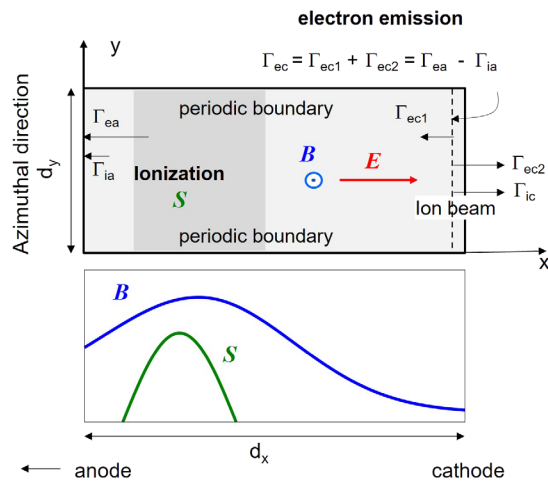


**FIG. 28.** Axial–azimuthal domain used in the benchmark 2D PIC-MCC simulations of Charoy *et al.*<sup>216</sup> and Boeuf and Garrigues<sup>183</sup> (top) and axial profiles of the perpendicular magnetic field and of the fixed ionization rate  $S$  (bottom). Collisionless simulation, with axial length  $d_x = 2.5$  cm, and azimuthal length  $d_y = 1.28$  cm. The simulation domain is periodic in the azimuthal direction. Electrons from the emissive cathode are injected uniformly along the dashed line on the right of the simulation domain. The total emitted electron flux  $\Gamma_{ec}$  (flux entering the channel,  $\Gamma_{ec1}$ , plus flux neutralizing the ion beam,  $\Gamma_{ec2}$ ) is equal to the net charged particle flux at the anode ( $\Gamma_{ea} - \Gamma_{ia}$ ).

simulations. Very large amplitude oscillations of the azimuthal electric field, on the order of 400 V/cm, can be seen in Fig. 29, with wavelengths below 1 mm and frequency in the MHz range.

One can actually distinguish in Fig. 29 two regions with different wavelengths on the left (smaller wavelength) and on the right side (larger wavelength) of the maximum magnetic field at  $x = 0.75$  cm.

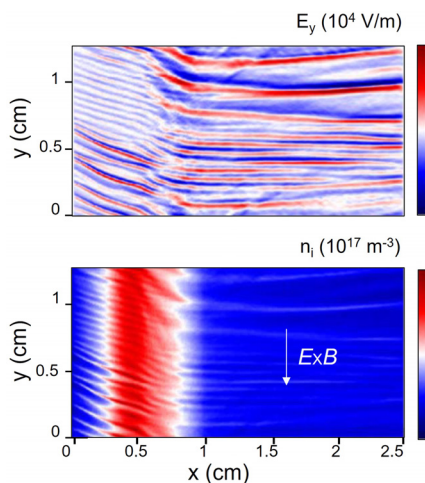


**FIG. 29.** 2D axial–azimuthal color maps of the azimuthal electric field (top) and ion density (bottom) at a given time, from PIC-MCC simulations, illustrating the electron cyclotron drift instability. Conditions of Fig. 28. The instability moves in the  $E \times B$  direction Adapted with permission from Charoy *et al.*, Plasma Sources Sci. Technol. **28**, 105010 (2019). Copyright 2023 IOP Publishing Ltd. (Fig. 4 of Ref. 216).

A fast Fourier transform of the azimuthal electric field of Fig. 29 at two different locations is shown in Fig. 30. The dispersion relation of the modified ion acoustic mode is also shown on these plots. We see that at the location  $x = 0.3$  cm, i.e., on the left of the maximum magnetic field, the angular frequency from the PIC simulation follows the angular frequency of the modified ion acoustic instability, Eq. (39), with a dominant mode corresponding to the mode with maximum growth rate (the maximum of the growth rate of Eq. (39) is obtained for  $k_x \lambda_{De} = 2^{-1/2}$ ). Similar results were obtained in Ref. 215. Although it is known that nonlinear effects can potentially lead to the transition to an ion acoustic instability, the exact reason for this transition in the 2D simulations, in contrast to the 1D case, and in spite of the fact that  $k_z$  is necessarily zero in this axial–azimuthal model, is unclear and need further study. The spectrum of the modified ion acoustic mode is less visible at the location  $x = 1.5$  cm of Fig. 30, where the dispersion relation from the PIC simulation exhibits a more discrete structure.

The space distribution of the ion density in the axial–azimuthal plane of Fig. 29 presents a maximum in the ionization region on the left of the maximum magnetic field and decreases, due to ion acceleration by the axial electric field, on the right of the maximum field, as expected in a Hall thruster. The axial profiles of the azimuthally and time-averaged axial electric field and ion density are shown in Fig. 31. Results from different PIC simulations performed by different groups<sup>216</sup> are represented on this figure. Although the principles of PIC simulations are relatively simple, the different numerical constraints (time step, grid spacing, number of particle per cell, ...) control the accuracy and numerical noise, and it is important to perform convergence tests and benchmarks (see Ref. 217 for a list of the past and current benchmarks simulations organized by the low-temperature plasma community to study instabilities in  $E \times B$  partially magnetized plasmas). The aim of the benchmark of the 2D axial–azimuthal ECDI reported in Ref. 216 was to increase the confidence in the simulation results and their physical interpretation. Good agreement between the different codes (Fig. 31) was obtained when 250 particles per cell were used in the simulations.

The axial profile of the electric field in Fig. 31(a) shows a maximum of about 500 V/cm with a shift of a few mm to the right of the

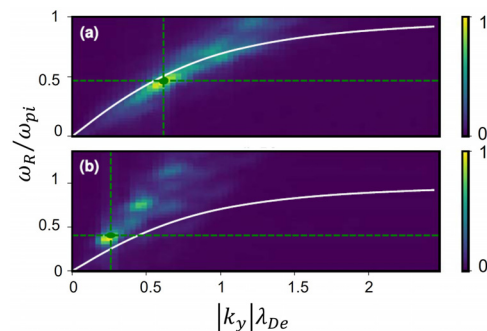


**FIG. 30.** Fast Fourier transform (FFT) of the azimuthal electric field (color map of Fig. 29, at  $x = 0.3$  cm, (a), and at  $x = 1.5$  cm, (b)). The solid line is the angular frequency of the ion acoustic instability [Eq. (39)]. The green dashed lines indicate the wavenumber and frequency of the dominant mode. Adapted with permission from Charoy *et al.*, Plasma Sources Sci. Technol. **28**, 105010 (2019). Copyright 2023 IOP Publishing Ltd. (Fig. 8 of Ref. 216).

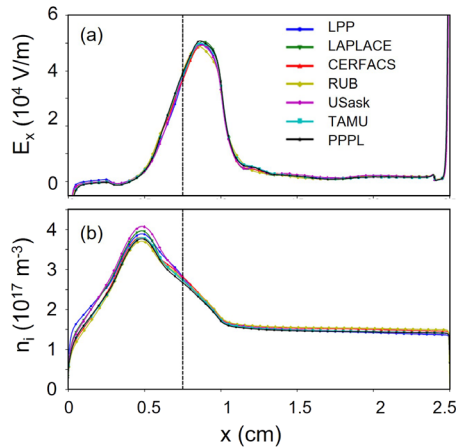


**FIG. 31.** Azimuthally and time-averaged axial profiles of the axial electric field (a), and ion density (b) deduced from the PIC-MCC simulations of Fig. 29. The different curves correspond to benchmark simulations by different groups. Adapted with permission from Charoy *et al.*, *Plasma Sources Sci. Technol.* **28**, 105010 (2019). Copyright 2023 IOP Publishing Ltd. (Fig. 5 of Ref. 216).

maximum magnetic field. The width of the acceleration region is less than 1 cm. Ions generated in the ionization region are accelerated by the axial electric field, resulting in the decay of the ion density from  $4 \times 10^{17} \text{ m}^{-3}$  in the ionization region to  $1.5 \times 10^{17} \text{ m}^{-3}$  at the end of the acceleration region [Fig. 31(b)].

The ECDI instability described in this section is responsible for the collisionless electron transport across the magnetic field. An effective Hall parameter or collision frequency due to the instability can be deduced from the simulations. The effective Hall parameter (see Sec. II A) deduced from the simulation at the location of the maximum magnetic field was  $h_{\text{eff}} \approx 192$  for a total current density of  $400 \text{ A/m}^2$  in the simulations of Ref. 183, under conditions close to those reported in this subsection and was found to decrease with decreasing total current density. This corresponds to an effective collision frequency  $\nu_{\text{eff}} \approx 8.3 \times 10^6 \text{ s}^{-1}$ . These values of  $h_{\text{eff}}$  and  $\nu_{\text{eff}}$  seem consistent with the experimental measurements. For example, the inverse Hall parameter  $h_{\text{eff}}^{-1}$  deduced from measurements in Fig. 18 is on the order of  $10^{-2}$ . Also, the ratio of electron to ion current in the exhaust region that can be deduced from the PIC simulations is on the same order as in the experiments. However, the amplitude of the azimuthal electric field oscillations predicted by the PIC simulations are much larger than those measured experimentally, and the question arises as to whether the mechanisms leading to anomalous transport are well described by this reduced PIC model. This issue is briefly discussed in Subsection V E.

## D. 2D radial-azimuthal PIC simulation: Electron cyclotron drift instability and modified two-stream instability

In order to study the role of electron transport parallel to the magnetic field, and of the presence of dielectric walls and sheaths in this direction, 2D PIC simulations in the radial-azimuthal plane have been performed. In these PIC models as well as in the 1D models of Sec. V A, the axial electric field cannot be calculated self-consistently

and is imposed. Different ways of describing the axial transport (e.g., finite length of the acceleration region or not, re-injection of particles, ionization) and the electron interactions with the dielectric walls perpendicular to the radial direction (i.e., to the magnetic field) have been used by different authors,<sup>218–222</sup> leading to various conclusions. Heron *et al.*<sup>218</sup> conclude that the balance due to the ECDI and the SEE (secondary electron emission at the walls) is extremely complex and depends on the emissivity of the wall as well as on the thruster geometry. Beam-plasma instabilities can even be present when the interaction of the SEE with the instability is too violent. Croes *et al.*<sup>219</sup> found that the wall effects play only an auxiliary role and suggest that the fact that there is experimental evidence that the nature of the walls has a strong influence on the characteristics of a thruster, is due to the modification of the electron distribution function by the SEE. Tavant *et al.*<sup>220</sup> showed that anomalous electron cross field transport decreases in the presence of SEE because of the electron cooling associated with secondary electron emission. This was also a result of the simulations of Taccogna *et al.*<sup>221</sup> From their 2D radial-azimuthal simulations without SEE in the direction of the applied electric field, Janhunen *et al.*<sup>111</sup> show that the ECDI proceeds as a coherent mode driven by the main cyclotron resonance ( $k_y v_0 = \omega_{ce}$ ) and does not evolve in the ion sound instability well into the nonlinear stage. They also found a strong energy cascade toward the longer wavelength and that the anomalous electron current was dominated by the long wavelength modes. They showed the development of a modified two-stream instability (MTSI) resulting in rapid heating parallel to the magnetic field due to the finite electric field along the magnetic field. The MTSI was shown to amplify the inverse energy cascade due to its long wavelength nature. Similar conclusions were drawn by Taccogna *et al.*<sup>221</sup> (where SEE was included). We illustrate below the radial-azimuthal models with the work of Villafana *et al.*,<sup>222</sup> which reports benchmark PIC simulations without SEE, in a radial-azimuthal ( $z, y$ ) Cartesian domain. Before doing that, we recall the definition and properties of the MTSI.

The MTSI can be obtained by considering the asymptotic case of cold electrons ( $T_e \rightarrow 0$ ) in the ECDI dispersion relation (37) with non-zero wavenumber parallel to the magnetic field,  $k_z \neq 0$ , and assuming  $k_x = 0$ . This implies that  $b \rightarrow 0$  and  $\xi \rightarrow \infty$ , where  $\xi$  is the argument of the  $Z$  function in Eq. (37). Lashmore-Davies<sup>223</sup> derived the cold electrons asymptotic form of the ECDI by keeping only the  $m = 0$  term in the sum of Eq. (37) and obtained the following form of the MTSI:

$$1 - \frac{\omega_{pi}^2}{\omega^2} - \frac{\omega_{pe}^2 k_z^2}{(\omega - k_y v_0)^2 k^2} + \frac{\omega_{pe}^2 k_y^2}{\omega_{ce}^2 k^2} = 0. \quad (40)$$

A more accurate asymptotic limit of Eq. (37) can be obtained by keeping the  $m = \pm 1$  terms in the sum of Eq. (37). The limits of the Bessel functions when  $b \rightarrow 0$  are  $I_0(b) \rightarrow \frac{1}{2}$  and  $I_{\pm 1}(b) \rightarrow b/2$ .

The exponential term gives  $(1 - b)$  for small  $b$  and the asymptotic form of the plasma function  $Z(\xi)$  for large values of  $\xi$  (since  $\nu_{Te} \rightarrow 0$ ) is

$$Z(\xi) \rightarrow -\frac{1}{\xi} \left( 1 + \frac{1}{2\xi^2} \right)$$

Therefore, the expression of the dispersion relation (37) in the cold electrons approximation takes the following asymptotic form (to the first order in  $T_e$ ):



$$1 - \frac{\omega_{pi}^2}{\omega^2} + \frac{1}{k^2 \lambda_{De}^2} \left[ b - \frac{1}{2\xi^2} - \frac{b}{2} \xi \left( \frac{1}{\xi^+} + \frac{1}{\xi^-} \right) \right] = 0,$$

with

$$\xi = \frac{\omega - k_y v_0}{k_z v_{Te} \sqrt{2}}, \quad \xi^\pm = \frac{\omega - k_y v_0 \pm \omega_{ce}}{k_z v_{Te} \sqrt{2}}, \quad b = k_y^2 \rho_e^2.$$

This gives a more general dispersion relation, which includes the upper hybrid Buneman instability, and can be called the modified Buneman two-stream instability (MBTSI),<sup>111</sup>

$$1 - \frac{\omega_{pi}^2}{\omega^2} - \frac{\omega_{pe}^2 k_z^2}{(\omega - k_y v_0)^2 k^2} - \frac{\omega_{pe}^2 k_y^2}{[(\omega - k_y v_0)^2 - \omega_{ce}^2] k^2} = 0. \quad (41)$$

The MTSI or MBTSI modes are important because they correspond to long wavelength instabilities, with wavenumber much smaller than the first cyclotron resonance  $|k_y| = \omega_{ce}/v_0$ . The MTSI appears as the first peak at low wavenumber for small enough  $|k_y|$  in Fig. 27. The growth rate of the MTSI on this figure is small but this mode can become important in the nonlinear regime because it can enhance the tendency toward long wavelength condensation or inverse energy cascade.

We illustrate below the development of ECDI and MTSI with the radial–azimuthal simulations of Villafana *et al.*<sup>222</sup> The principles and conditions of the simulations in the model of Villafana *et al.*<sup>222</sup> are as follows (see Fig. 32). The radial magnetic field is given and uniform. The electric field in the radial–azimuthal plane is obtained by solving Poisson’s equation at each time step in this plane, and the electric field in the axial direction is imposed. Electron and ion trajectories are followed not only in the  $(y, z)$  plane but also in the axial direction. The simulation domain is bounded by two grounded walls in the radial direction, and periodic boundary conditions are used in the azimuthal directions. Electrons and ions reaching the walls are removed from the simulation. A finite length  $2L_x$  is considered in the axial,  $x$  direction, and each charged particle exiting the  $[-L_x, L_x]$  interval is replaced by a new electron at  $x = 0$  and at the same  $(y, z)$  location, according to a Maxwellian distribution at fixed temperatures,  $T_{e,0}$  and  $T_{i,0}$  for

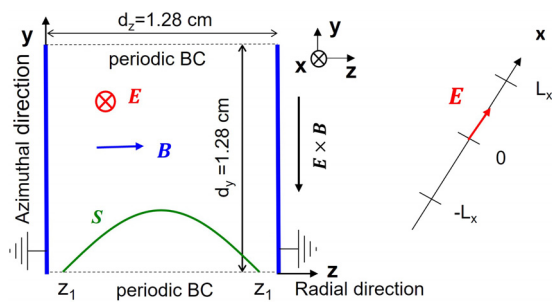


**FIG. 32.** Simulation domain for the radial–azimuthal model. The axial electric field and radial magnetic field are given as  $E = 10^4$  V/m and  $B = 20$  mT in the simulations reported here.<sup>222</sup> The dimensions in the radial and azimuthal directions are  $d_z = d_y = 1.28$  cm. The virtual length in the axial direction is  $L_x = 1$  cm. The ionization rate  $S$  has a cosine profile between  $z_1 = 0.09$  cm, and  $z_2 = 1.19$  cm. The integral of  $S(y, z)$  in the radial direction correspond to a current density of  $100$  A/m<sup>2</sup>. The walls in the radial direction are grounded, and secondary electron emission is not taken into account.

electrons and ions respectively. The value of  $L_x$ , together with the given axial electric field  $E_x$ , imposes the maximum energy gain ( $L_x E_x$ ) from this applied electric field.

To balance the charged particle losses to the walls, a fixed ionization rate with a cosine profile in an interval  $[z_1, z_2]$  in the radial direction is imposed. The integral of the given ionization rate over the radial direction gives the total discharge current density ( $100$  A/m<sup>2</sup>). These conditions are summarized in Fig. 32 (see Ref. 222 for more details).

The results of the radial–azimuthal PIC simulations in these conditions show the clear development of the ECDI with a dominant  $m = 1$  mode ( $k_y = \omega_{ce}/v_0$ ) and a less visible  $m = 2$  mode, as can be seen in the FFT plot of Fig. 33. No evolution toward an ion sound instability was found in these simulations. The MTSI at low wavenumber is also clearly apparent in Fig. 33, and its amplitude seems to decay in time, so the inverse cascade is not observed in these conditions. The relatively small length of the simulation domain in the azimuthal direction could limit the development of long wavelength modes in these simulations (this is confirmed by the simulations of Refs. 111 and 224).

### E. Experimental evidence of the ECDI and conclusion

We can conclude from Secs. VA–VD that electron cyclotron instabilities are ubiquitous in particle simulations of  $E \times B$  plasmas under Hall thruster conditions and that they result in large amplitude oscillations of the azimuthal electric field with wavelengths around 1 mm and frequency in the 5–10 MHz range. Soon after the first evidence of the presence of ECDI in PIC simulations by Adam *et al.*,<sup>198</sup> experiments based on collective light scattering were designed to detect these instabilities in Hall thrusters. Electron density fluctuations were measured by coherent Thomson scattering by Tsikata *et al.*<sup>210,225–227</sup> in Hall thrusters and were found to be consistent with the presence of the ECDI microinstabilities predicted by the PIC simulations and with their transition into an ion acoustic instability. The measurements showed the existence of a finite wave component along the magnetic field, which could explain the transition to the ion sound behavior.<sup>210</sup> However, the amplitudes of the fluctuations measured by collective

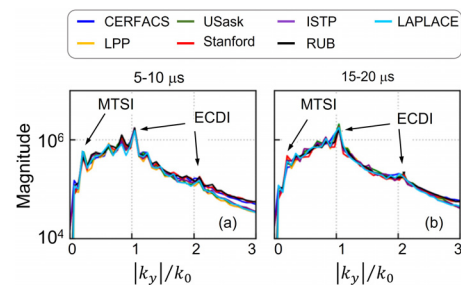


**FIG. 33.** 1D azimuthal fast Fourier transform of the azimuthal electric field, averaged over radial positions and over two time intervals, (a) 5–10  $\mu$ s, (b) 15–20  $\mu$ s.  $k_0 = \omega_{ce}/v_0$  is the wavenumber corresponding to the first cyclotron resonance. The different curves correspond to simulations by different groups carried out within a benchmark of different codes. Adapted with permission from Villafana *et al.*, Phys. Plasmas **30** 075002 (2021). Copyright 2021 AIP Publishing (Fig. 9 of Ref. 222).

light scattering were much smaller than those observed in the simulations and displayed in Fig. 29. Possible reasons for this discrepancy are 3D effects, coupling of wall electron-emission to the ECDCI, limits in the azimuthal dimension of the 2D models which prevent inverse energy cascades, etc. The results of laser experiments show the presence of ECDCI, but it is uncertain if the PIC simulations correctly identify ECDCI or its modified ion acoustic version as the main source of anomalous transport in the acceleration and near-plume region of a Hall thruster. A discussion of the experimental measurements of the microinstabilities in Hall thrusters and of their interpretation, and of the need for joint experimental and modeling work to clarify the relationship between different instabilities and anomalous transport can be found in the section by Jorns and Tsikata of Kaganovich *et al.*<sup>1</sup>

**VI. MACROSCOPIC INSTABILITIES IN MAGNETRONS. ROTATING SPOKE AND IONIZATION WAVE**

Two-dimensional PIC-MCC simulations were conducted to examine the physics of spokes in magnetron discharges. The following are the key findings from these simulations:

As in Sec. V C, the simulations are done in a rectangular axial-azimuthal domain and periodic boundary conditions are used in the azimuthal direction to represent the closed-drift. The simulation domain is shown in Fig. 34(a). The cathode-anode gap is  $d_x = 2$  cm, and the length of the domain in the azimuthal direction is  $d_y = 8$  cm. Simulation results will be presented below for two profiles of the axial magnetic field,  $B_1(x)$  and  $B_2(x)$ , shown in Fig. 34(b). The magnetic field profile  $B_1(x)$  is of the form

$$B_1(x) = ae^{-\frac{x}{2\sigma}} + b, \tag{42}$$

with  $\sigma = 0.35d_x$  and  $a$  and  $b$  chosen so that  $B_1(0) = 0.1$  T,  $B_1(d_x) = 0$ ,

The magnetic field  $B_2(x)$  is

$$B_2(x) = B_2(0)e^{-\frac{x}{\alpha}} \text{ with } B_2(0) = 0.12 \text{ T}, \alpha = 0.3d_x. \tag{43}$$

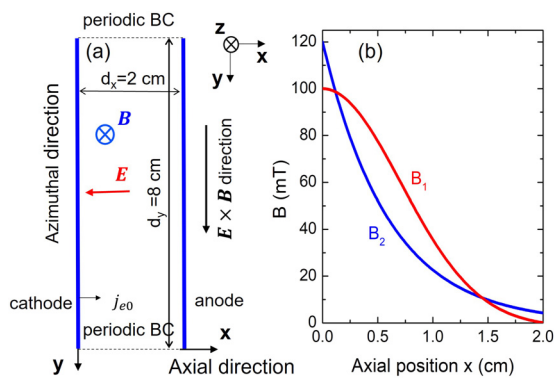


**FIG. 34.** (a) Axial-azimuthal simulation domain for a magnetron discharge. The magnetic field is perpendicular to the simulation domain. A 260 V voltage is applied between cathode and anode, and a fixed electron current density  $j_{e0}$  is emitted at the cathode to represent the secondary electron emission by ion impact. (b) Two different axial profiles,  $B_1(x)$  and  $B_2(x)$ , of the perpendicular magnetic field used in the simulations.

**A. Structure of the rotating spoke at steady state**

We first present some simulation results for a pressure of 2 Pa, with the magnetic field profile  $B_1$  of Fig. 34(b). The conditions (argon, 2 Pa, 260 V dc voltage, secondary emission 25 mA/m<sup>2</sup>) are similar to those of Refs. 150 and 151 except that the azimuthal length of the simulation is 8 cm instead of 4 cm and the magnetic field profile is slightly different ( $B_1(d) = 0.01$  T in Refs. 150 and 151 instead of  $B_1(d) = 0$ ). These conditions are similar to those of the experimental work of Ito *et al.*,<sup>142</sup> with a scaling factor of 10 (pressure and magnetic field divided by 10, dimensions multiplied by 10).

The PIC-MCC simulations in these conditions predict the formation of two large scale rotating non-uniformities (spokes) along the azimuthal direction. Figure 35 displays the 2D distribution of the electric potential, ion density, ionization rate, and electron current density at a given time after the spoke regime is established. The spokes are moving in the  $-E \times B$  direction at a velocity of about 10 km/s. The spoke is characterized by a region of intense ionization, which is typically observed as a luminous region in experiments. It is located at the edge and on top of a region with higher plasma density and is oriented in the  $-E \times B$  direction. By extension, we will refer to the combination of the region of intense ionization and the adjacent region of high plasma density as the “spoke.” The region of high plasma density is characterized by a low electric field. In contrast, the region of intense ionization is located in an area where the electric potential drops abruptly. The deformation of the potential forms a long wavelength ( $\sim 4$  cm) azimuthal wave that moves upward.

The region of high plasma density moves in the direction of the region of intense ionization, and therefore the spoke can be considered as an ionization wave under these conditions. The electric field is perpendicular to the equipotential lines so the  $E \times B$  electron current

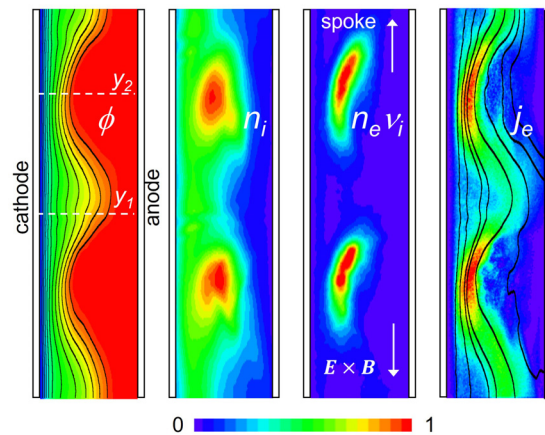


**FIG. 35.** 2D color maps of the electric potential,  $\phi$ , ion density,  $n_i$ , ionization rate,  $n_e v_i$ , and current density  $j_e$  in the simulation domain of Fig. 34(a), with the magnetic profile  $B_1$  of Fig. 34(b). Argon, 2 Pa, 260 V dc voltage, and net current density of emitted electron 25 mA/m<sup>2</sup>. The units are 260 V for  $\phi$ ,  $0.5 \times 10^{16}$  m<sup>-3</sup> for  $n_i$ ,  $1.2 \times 10^{22}$  m<sup>-3</sup> s<sup>-1</sup> for  $n_e v_i$ , and 200 A/m<sup>2</sup> for  $j_e$ . The equipotential contours are plotted from 20 to 240 V and are separated by 20 V. Some streamlines are plotted for the electron current density. The initial plasma density in the simulation was uniform and equal to  $5 \times 10^{14}$  m<sup>-3</sup> and the plasma parameters of this figure are plotted at time  $t = 18 \mu\text{s}$ . The axial plots of Fig. 36 correspond to the azimuthal positions  $y_1$  and  $y_2$  indicated by dashed lines on the potential plot.

follows the equipotential contours. This can be seen in the  $j_e$  plot of Fig. 35.

The maximum electron current density roughly follows the equipotential lines at the boundary between the low electric field region (red region on the potential plot of Fig. 29) and the region (green-yellow regions on the potential plot) where a large electric field is present in the quasineutral plasma. This boundary is characterized by a significant potential drop and can be called a double layer. The deformation of the equipotential contours by the spoke acts as a short-circuit between the cathode and anode regions, enabling cross field electron transport. The axial profiles of the charged particles densities and axial electric field at two different azimuthal locations noted  $y_1$  and  $y_2$  in Fig. 35 (dashed lines on the potential plot) are shown in Fig. 36. The large cathode sheath electric field is apparent on this figure but one can also see that the electric field penetrates the quasineutral plasma with a modulation of the penetration depth that depends on the azimuthal location and is associated with the electric potential wave. The axial electric field and plasma density gradient are in the same direction, which suggests that the plasma non-uniformity is triggered by gradient-drift or Simon–Hoh instability.

The spoke instability is highly coherent in both the simulations and in many experiments on magnetron discharges. The position of the ionization region is well-defined on the side of the potential wave where the axial component of the  $\mathbf{E} \times \mathbf{B}$  drift is directed toward the cathode. Electrons are clearly heated in the spoke region and the question arises as to the mechanisms leading to this electron heating. Collisional heating is possible along the line of intense electron current density and large potential drop seen on the  $j_e$  plot of Fig. 35, but it is unclear why electron heating would only occur on one side of the potential wave.

**B. Mechanisms of electron heating in the spoke**

A detailed analysis shows that collisional heating is not the dominant mechanism of electron heating and that another mechanism is responsible for a large part of this electron heating. This is illustrated in Fig. 37, which shows an electron trajectory in the double layer region. We said above that electrons follow the equipotential lines in their  $\mathbf{E} \times \mathbf{B}$  drift between collisions and therefore should not gain energy on the average, along their path. Figure 37(b) shows a

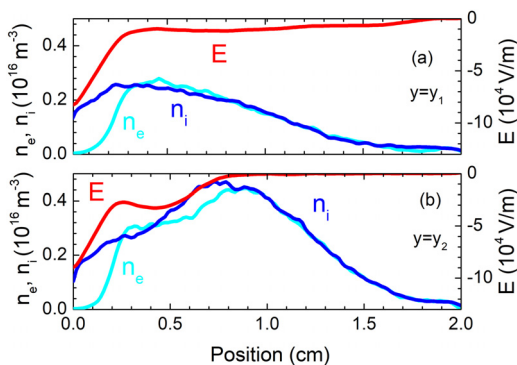


FIG. 36. Axial profiles of the axial electric field, and the electron and ion densities at two different azimuthal positions (a)  $y_1$  and (b)  $y_2$  indicated by dashed lines on the potential plot of Fig. 35.

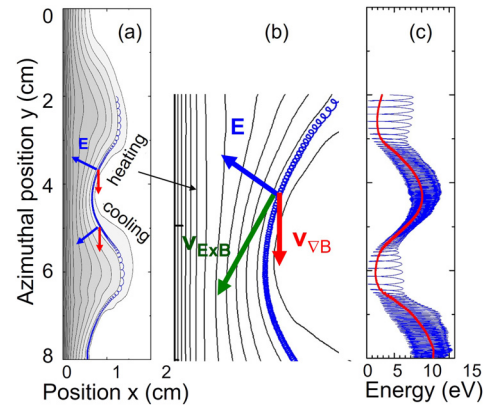


FIG. 37. (a) Example of electron trajectory along an equipotential line in the double layer region in the axial-azimuthal plane; (b) magnified view of part of Fig. 37(a) illustrating the fact that the electron trajectory slightly deviates from the equipotential line due to  $\nabla B$  drift; and (c) variations of the electron kinetic energy as a function of azimuthal position along the trajectory of Fig. 37(a). The red line is the averaged energy over the cyclotron oscillations. Same conditions as Fig. 35.

magnified view of part of the electron trajectory of Fig. 37(a). We see that the electron slightly deviates from the equipotential contour, so its mean energy [red line of Fig. 37(c)] does not stay constant along its trajectory. The electron gains energy on the upper part of the potential wave (leading edge of the spoke or spoke front) and loses energy on the other side (trailing edge of the spoke). These successive energy gain and losses are related to the  $\nabla B$  drift. This drift is due to the gradient of magnetic field and is in the  $-\mathbf{B} \times \nabla B$  direction [it is included in the  $v_D$  and  $\omega_D$  terms of the fluid dispersion relation, see Eq. (26)]. It can be written as<sup>228</sup>

$$v_{\nabla B} = -1/2\rho_e v_{\perp} \mathbf{B} \times \nabla B / B^2 = -\varepsilon_{\perp} \mathbf{B} \times \nabla B / B^3, \tag{44}$$

where  $v_{\perp}$  is the electron velocity and  $\varepsilon_{\perp}$  is the electron kinetic energy in eV, perpendicular to the magnetic field. In the conditions of the simulations considered here,  $v_{\nabla B}$  is directed in the azimuthal direction, in the positive  $y$  direction, i.e., downward.

The electron heating or cooling per electron per unit time due to the  $\nabla B$  drift is given (in eV/s) by

$$\theta_{v_{\nabla B}} = -v_{\nabla B} \cdot \mathbf{E} = \varepsilon_{\perp} E_y / (BL_B). \tag{45}$$

As illustrated in Fig. 37(a), the scalar product  $v_{\nabla B} \cdot \mathbf{E}$  is negative on the top side of the potential wave and positive on the bottom side so that  $\nabla B$  drift heating takes place at the leading edge of the spoke while cooling occurs at the trailing edge. Electron heating and cooling would cancel each-other in the absence of collisions. The net heating due to  $\nabla B$  drift in our conditions is due to collisions: electrons can lose energy through inelastic collisions before  $\nabla B$  drift cooling becomes important.

**C. Linear development of the instability and evolution toward an ionization wave**

Simulations under conditions close to those of the experiments and Langmuir probe measurements of Held *et al.*<sup>145</sup> (see Fig. 24) have been performed and are described in detail in Ref. 154. The simulation

23 July 2023 04:21:49

domain is the same as above [Fig. 34(a)], the argon pressure is 0.6 Pa, and the magnetic field distribution corresponds to the  $B_2$  curve of Fig. 34(b). In these conditions, only one spoke is observed in the simulations (as in the experiments, where the closed drift of the magnetron is also on the order of 8 cm). The spoke rotates, as in the previous example, in the  $-E \times B$  direction but at a smaller velocity, on the order of 1.3 km/s (2.5 km/s in the experiment of Held *et al.*<sup>145</sup>) The 1D stable, steady state solution of this problem was used as initial condition for the 2D simulation. This means that the initial axial positions and velocities of the charged particles in the 2D simulations are identical to those of the 1D steady state solution. This allows the study of the linear development of the instability around the unperturbed, stable, steady state 1D solutions. The plasma density gradient and electric field of the 1D solution were in the same direction, indicating that the condition for a gradient-drift or Simon–Hoh instability was satisfied. An interesting aspect of the 2D solutions was that a gradient-drift instability forms in a few hundred nanoseconds, leading to the rotation of plasma non-uniformities in the  $+E \times B$  direction. After about 1  $\mu$ s, ionization starts to play an important role and the instability evolves into an ionization wave, rotating in the  $-E \times B$  direction (details are shown in Ref. 154). Figure 38 displays color maps of the ion density, electron temperature, and ionization rate at a given time, when the instability has reached a steady state, saturated regime. Equipotential contours are also shown, superimposed on the ion density color map. A plot of the electron heating rates due to  $\nabla B$  drift,  $\theta_{v_{\nabla B}}$ , and to collisions,  $\theta_E$ , is also represented in Fig. 38, as a function of azimuthal position and at the axial position  $x = 1$  cm. The collisional heating rate,  $\theta_E$ , can be written as

$$\theta_E = -v_{||E} \cdot E = \frac{v}{\omega_{ce}} \frac{E^2}{B}, \quad (46)$$

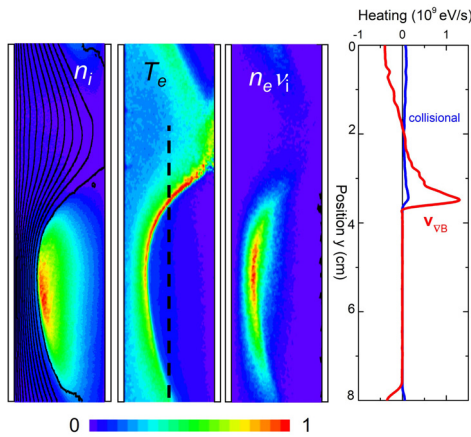


**FIG. 38.** 2D color maps of the ion density,  $n_i$ , electron temperature,  $T_e$ , and ionization rate,  $n_e \nu_i$  at a given time, under conditions close to the experiments of Held *et al.*<sup>145</sup> Equipotential contours are superimposed on the ion density color map. The right plot shows the azimuthal profile of the collisional and  $\nabla B$  drift heating rates along the dashed line of the electron temperature plot, at  $x = 1$  cm. The conditions are: argon, 0.6 Pa, 260 V dc voltage, net current density of emitted electron 30 mA/m<sup>2</sup>. The units are  $2 \times 10^{16} \text{ m}^{-3}$  for  $n_i$ , 20 eV for  $T_e$  and  $1.4 \times 10^{22} \text{ m}^{-3} \text{ s}^{-1}$  for  $n_e \nu_i$ . The equipotential contours are plotted from 20 to 260 V and are separated by 20 V. Adapted from Figs. 5 and 11 of Ref. 154.

where  $v_{||E}$  is the collisional electron drift velocity parallel to the electric field.

We see in Fig. 38 the sharp increase in the electron temperature at the leading edge of the spoke. The maximum ionization rate is shifted downward along the double layer, with respect to the electron temperature (the mean free path for ionization is a few cm). The plots of the  $\nabla B$  drift and collisional heating rates clearly indicate that the  $\nabla B$  drift heating is largely dominant in the double layer.

### D. Comparisons with experiments

The time variation of the plasma parameters, electron density, electron temperature, and plasma potential at a location 6 mm above the cathode surface, i.e., on the spoke path, are shown in Fig. 39 and can be compared to the Langmuir probe measurements of Held *et al.*<sup>145</sup> (reproduced in Fig. 24). These parameters exhibit large amplitude oscillations with very sharp variations of the electron temperature when the leading edge of the spoke reach the point where they are recorded in the simulation ( $x = 6$  mm). There are some clear discrepancies between the experiments and the simulation results, but the qualitative agreement is reasonably good. The plasma density is lower in the simulation, by a factor of about 10. This is because the electron emission current at the cathode has been limited in order to reduce the simulation time (which increases with increasing plasma density). The large increase in the electron temperature at the leading edge of the spoke is a common feature of experiments and simulations but the rise and decay of the electron temperature have different time constants. The period of variations of the plasma parameters is longer in

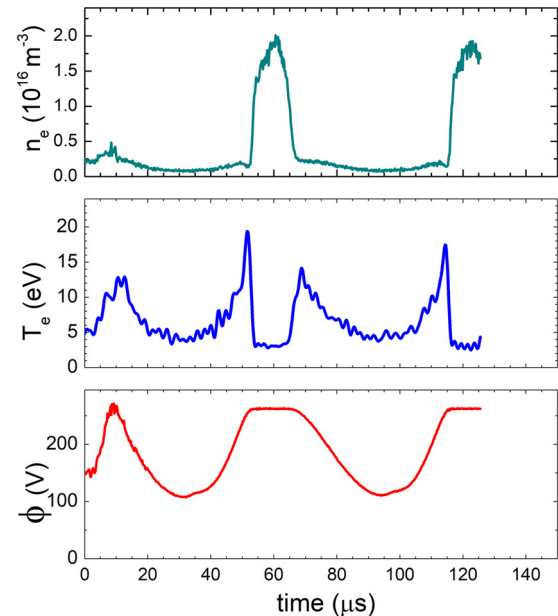


**FIG. 39.** Time variations of electron density,  $n_e$ , electron temperature,  $T_e$ , and plasma potential  $\phi$  from the 2D PIC-MCC simulation, 6 mm above the cathode surface ( $x = 6$  mm), under the same conditions as Fig. 38 (argon, 0.6 Pa, dc voltage 260 V). To be compared with the experimental measurements of Held *et al.*<sup>145</sup> reproduced in Fig. 24 of the present paper). Adapted with permission from Boeuf, Phys. Plasmas, 30 022112 (2023). Copyright 2023 AIP (Fig. 9 of Ref. 154).

the simulations (60  $\mu$ s, instead of about 32  $\mu$ s in the experiment, see Fig. 24). This is consistent with the higher spoke velocity in the experiment (2.5 km/s, vs 1.3 km/s in the simulations).

Held *et al.* have also measured the electron energy probability function at different times near the spoke front and found a strong modulation of the tail of the distribution. This is also observed in the simulations as shown in Fig. 40. The population of high energy electrons increases abruptly in the double layer region and decays in the high plasma density and low field region of the spoke. This is consistent with the heating of electrons flowing along the double layer in the spoke front. The residence time of electrons in the high-density plasma behind the spoke front is long because these electrons are trapped in this low electric field region. This explains the fast decay of the electron temperature in the simulations and the large population of low-energy electrons in that region (Coulomb collisions, not taken into account in the model, could reduce this effect).

Finally, the simulations show that the number of spokes increases with pressure, in agreement with the experiments of Panjan *et al.*<sup>143</sup> who showed that this is related to a decrease in the ionization mean free path with increasing pressure.

To conclude this section, we can say that the simulations tend to show that the very coherent mode of spoke rotation observed in dc magnetron discharges in experiments and simulations is due to the strong and localized electron heating associated with the  $\nabla B$  drift, and that the  $-E \times B$  rotation is a consequence of the evolution of a gradient-drift instability into an ionization wave resulting from this

mechanism of electron heating. Simulations performed under uniform magnetic field in similar conditions exhibit much less coherent instabilities rotating in the  $+E \times B$  direction.

### VII. CONCLUSION

Low-temperature  $E \times B$  plasmas with closed-drift configurations are widely used in space propulsion and plasma processing; however, their design and development still rely on a semi-empirical approach due to a lack of self-consistent engineering models. The availability of predictive models would be an extremely valuable asset for the industry as it would greatly reduce development costs. Even though understanding the fascinating physics of  $E \times B$  plasmas can be a goal in itself, the important research effort devoted, for example, to Hall thrusters in the last twenty years is largely driven by the development of predictive models.

The physics of these plasmas is complex and non-linear, and the presence of instabilities at a wide range of frequencies and wavelengths makes it challenging to develop predictive models. In this tutorial, we have shown that, despite these difficulties, significant progress has been made over the years in characterizing and understanding the various types of instabilities that can occur in closed-drift devices. This progress has been made possible through a collaborative research effort involving theory, simulations and experiments. The theory, based on the linearization of fluid or kinetic transport equations, has resulted in the derivation of dispersion relations that define the various types of instabilities that may develop in the partially magnetized plasmas of closed-drift devices. Computer simulations, primarily using particle methods, have been used to verify or to initiate the theoretical developments and to describe the non-linear evolution of instabilities. Experiments have revealed the presence of some of the instabilities predicted by theory and simulation. Despite these important achievements, the development of fully predictive models is still not within our reach for the following reasons. (1) Although the simulations can predict both the linear and non-linear evolution of some instabilities, they are based on reduced or over-simplified models that focus on one particular aspect or one particular type of instability. Additionally, these models are primary two-dimensional (and still computationally intensive) with limitations in the dimensions of the simulation domain that may prevent the inverse energy cascade to longer wavelengths. (2) Three-dimensional particle models can be run in massively parallel simulations but their use under realistic plasma densities and device dimensions remains challenging and does not allow parameter studies at a reasonable cost. (3) An alternative approach is using hybrid models, in which electrons are treated as a fluid and ions and neutral atoms are treated as particles. This approach is less computationally intensive and is better suited for engineering applications. It has been used in the last twenty years, but it is not self-consistent, as it cannot accurately describe instabilities. These models use anomalous transport coefficients, such as electron mobility, as input to fit experimental data. It is yet to be determined whether anomalous transport coefficients derived from particle simulations can be used to improve the predictivity of hybrid models.

The strong electric fields in some regions of  $E \times B$  devices result in  $E \times B$  drift velocities that approach thermal particle velocities. In these conditions, kinetic theory and simulations are essential for studying anomalous transport. Results from existing 1D and 2D simulations, as well as emerging 3D simulations,<sup>149,229,230</sup> suggest not only

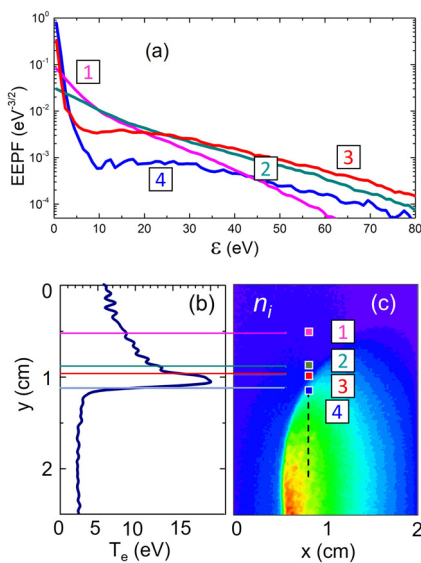


**FIG. 40.** (a) Normalized electron energy probability function (EEPF) at four different azimuthal locations around the spoke front, 8.8 mm above the cathode surface ( $x = 8.8$  mm) obtained from the PIC-MCC simulation at a given time in the conditions of Fig. 38. The EEPF are integrated over squares of 80  $\mu$ m side [indicated on (c)] in space, and over 10 ns in time; (b) azimuthal profile of the electron temperature at  $x = 8.8$  mm around the spoke front in the conditions of (a); (c) 2D distribution of ion density. The azimuthal locations corresponding to the EEPF of (a) are indicated by colored squares and numbers on (c), and by lines on (b), with the same colors and numbers as the EEPF plots on (a). Adapted with permission from Boeuf, Phys. Plasmas, **30** 022112 (2023). Copyright 2023 AIP (Fig. 10 of Ref. 154).

quantitative changes in multidimensional effects, such as the reduction of fluctuation amplitudes and associated transport, but also qualitative changes due to the emergence of new instability regimes (e.g. MTSI) and complex plasma-wall interactions. These investigations require comprehensive 3D simulations, the importance of which cannot be underestimated.

The physics of low-temperature partially magnetized plasmas presents a formidable intellectual challenge in the field of general nonlinear physics. The magnetic configurations, though simple in appearance, give rise to turbulence and transport in  $E \times B$  plasmas that are just as complex as those observed in high-temperature fusion plasmas. This makes it a topic that deserves significant attention and focused research efforts.

Despite the challenges in achieving a fully self-consistent description of  $E \times B$  plasmas for closed-drift devices, we are optimistic that our capabilities in understanding and modeling these plasmas will continue to improve. This will be achieved through (1) increasing model power and complexity with larger simulation domains and 3D simulations (investments in exascale computing at a small fraction of the cost of those spent on fusion plasmas would certainly bring us closer to fully predictive codes, see, e.g., the project WarpX, an exascale computing platform for beam-plasma simulations<sup>231</sup>) (2) continuing international collaboration through  $E \times B$  workshops and benchmarking of simulations and experiments, and (3) strengthening the synergy between theory, simulations and experiments.

## ACKNOWLEDGMENTS

JPB thanks the French Spatial Agency CNES for continuous support and the RTRA STAE foundation under the project IMPULSE. Part of the work of AS in this tutorial was supported by NSERC Canada, U.S. Air Force Office of Scientific Research and The Digital Research Alliance of Canada.

## AUTHOR DECLARATIONS

### Conflict of Interest

The authors have no conflicts to disclose.

### Author Contributions

**Jean-Pierre Boeuf:** Conceptualization (lead); Data curation (lead); Formal analysis (equal); Writing – original draft (lead); Writing – review & editing (equal). **Andrei I. Smolyakov:** Conceptualization (supporting); Data curation (supporting); Formal analysis (equal); Writing – original draft (supporting); Writing – review & editing (equal).

## DATA AVAILABILITY

The data that support the findings of this study are available from the corresponding author upon reasonable request.

## REFERENCES

- I. D. Kaganovich, A. Smolyakov, Y. Raitses, E. Ahedo, I. G. Mikellides, B. Jorns, F. Taccogna, R. Gueroult, S. Tsikata, A. Bourdon, J.-P. Boeuf, M. Keidar, A. T. Powis, M. Merino, M. Cappelli, K. Hara, J. A. Carlsson, N. J. Fisch, P. Chabert, I. Schweigert, T. Lafleur, K. Matyash, A. V. Khrabrov, R. W. Boswell, and A. Fruchtman, “Physics of  $E \times B$  discharges relevant to plasma propulsion and similar technologies,” *Phys. Plasmas* **27**, 120601 (2020).
- A. I. Smolyakov, O. Chapurin, W. Frias, O. Koshkarov, I. Romadanov, T. Tang, M. Umansky, Y. Raitses, I. D. Kaganovich, and V. P. Lakhin, “Fluid theory and simulations of instabilities, turbulent transport and coherent structures in partially-magnetized plasmas of  $E \times B$  discharges,” *Plasma Phys. Controlled Fusion* **59**, 014041 (2017).
- V. V. Zhurin, H. R. Kaufman, and R. S. Robinson, “Physics of closed drift thrusters,” *Plasma Sources Sci. Technol.* **8**, R1 (1999).
- A. I. Morozov, “The conceptual development of stationary plasma thrusters,” *Plasma Phys. Rep.* **29**, 235 (2003).
- D. M. Goebel and I. Katz, *Fundamentals of Electric Propulsion: Ion and Hall Thrusters* (Wiley, 2008).
- A. I. Morozov and V. V. Savel'ev, in *Review of Plasma Physics*, edited by M. A. Leontovich (Springer, 2000), Vol. 8.
- J.-P. Boeuf, “Tutorial: Physics and modeling of Hall thrusters,” *J. Appl. Phys.* **121**, 011101 (2017).
- H. Kaufman, R. Robinson, and R. I. Seddon, “End-Hall ion sources,” *J. Vac. Sci. Technol. A* **5**, 2081 (1987).
- N. Oudini, G. J. M. Hagelaar, J. P. Boeuf, and L. Garrigues, “Physics and modeling of an end-Hall (gridless) ion source,” *J. Appl. Phys.* **109**, 073310 (2011).
- V. Zhurin, *Industrial Ion sources: Broadbeam Gridless Ion Source Technology* (Wiley-VCH Verlag GmbH & Co. KGaA, Weinheim, Germany, 2012).
- V. Dudnikov and A. Westner, “Ion source with closed drift anode layer plasma acceleration,” *Rev. Sci. Instrum.* **73**, 729 (2002).
- K. Sarakinos, J. Alami, and S. Konstantinidis, “High power pulsed magnetron sputtering: A review on scientific and engineering state of the art,” *Surf. Coat. Technol.* **204**, 1661–1684 (2010).
- J. T. Gudmundsson, N. Brenning, D. Lundin, and U. Helmersson, “High power impulse magnetron sputtering discharge,” *J. Vac. Sci. Technol. A* **30**, 030801 (2012).
- J. T. Gudmundsson, “Physics and technology of magnetron sputtering discharges,” *Plasma Sources Sci. Technol.* **29**, 113001 (2020).
- A. Anders, “Tutorial: Reactive high power impulse magnetron sputtering (R-HiPIMS),” *J. Appl. Phys.* **121**, 171101 (2017).
- W. Schuurman, “Investigation of a low pressure penning discharge,” *Physica* **36**, 136 (1967).
- W. Schuurman, “On the theory of electrical characteristics of a penning discharge at low magnetic field,” *Physica* **43**, 513 (1969).
- J. L. Rovey, “Design parameter investigation of a cold-cathode Penning ion source for general laboratory applications,” *Plasma Sources Sci. Technol.* **17**, 035009 (2008).
- B. Wolf, *Handbook of Ion Sources* (CRC Press, Boca Raton, FL, 1995).
- F. M. Penning, “A new manometer for low gas pressures especially between  $10^{(-3)}$  and  $10^{(-5)}$  mm,” *Physica* **4**, 71 (1937).
- F. M. Penning, “The spark discharge in low pressure between coaxial cylinders in an axial magnetic field,” *Physica* **3**, 873 (1936).
- W. Knauer, “Diocotron instability in plasmas and gas discharges,” *J. Appl. Phys.* **37**, 602 (1966).
- P. A. Redhead, “Instabilities in crossed-field discharges at low pressures,” *Vacuum* **38**, 901 (1988).
- R. C. Davidson, *Physics of Nonneutral Plasmas* (Addison-Wesley, New York, 1990).
- N. A. Kervalishvili, “Formation and dynamics of vortex structures in pure and gas-discharge nonneutral collisionless electron plasmas,” *J. Georgian Geophys. Soc.* **15B**, 120 (2012).
- J.-P. Boeuf, “Rotating structures in low temperature magnetized plasmas; insight from particle simulations,” *Front. Phys.* **2**, 74 (2014).
- V. Kim and A. Semenkin, “History of the Hall Thrusters Development in USSR,” in 30th International Electric Propulsion Conference, Florence, Italy, 2007.
- S. N. Abolmasov, “Physics and engineering of crossed-field discharge devices,” *Plasma Sources Sci. Technol.* **21**, 035006 (2012).
- S. Mazouffre, “Electric propulsion for satellites and spacecraft: Established technologies and novel approaches,” *Plasma Sources Sci. Technol.* **25**, 033002 (2016).

- <sup>30</sup>I. Levchenko, S. Xu, S. Mazouffre, D. Lev, D. Pedrini, D. Goebel, L. Garrigues, F. Taccogna, and K. Bazaka, "Perspectives, frontiers, and new horizons for plasma-based space electric propulsion," *Phys. Plasmas* **27**, 020601 (2020).
- <sup>31</sup>E. Dale, B. Jorns, and A. Gallimore, "Future directions for electric propulsion research," *Aerospace* **7**, 120 (2020).
- <sup>32</sup>A. Sengupta, "Magnetic confinement in a ring-cusp ion thruster discharge plasma," *J. Appl. Phys.* **105**, 093303 (2009).
- <sup>33</sup>R. Wirz and D. Goebel, "Effects of magnetic field topography on ion thruster discharge performance," *Plasma Sources Sci. Technol.* **17**, 035010 (2008).
- <sup>34</sup>B. Dankongkakul and R. Wirz, "Miniature ion thruster ring-cusp discharge performance and behavior," *J. Appl. Phys.* **122**, 243303 (2017).
- <sup>35</sup>Y. Sakawa, C. Joshi, P. Kaw, V. Jain, T. Johnston, F. Chen, and J. Dawson, "Nonlinear evolution of the modified Simon-Hoh instability via a cascade of sideband instabilities in a weak beam plasma system," *Phys. Rev. Lett.* **69**, 85 (1992).
- <sup>36</sup>Y. Sakawa and C. Joshi, "Growth and nonlinear evolution of the modified Simon-Hoh instability in an electron beam-produced plasma," *Phys. Plasmas* **7**, 1774 (2000).
- <sup>37</sup>C. Rebont, N. Claire, T. Pierre, and F. Doveil, "Ion velocity distribution function investigated inside an unstable magnetized plasma exhibiting a rotating nonlinear structure," *Phys. Rev. Lett.* **106**, 225006 (2011).
- <sup>38</sup>N. Claire, A. Escarguel, C. Rebont, and F. Doveil, "Ion velocity analysis of rotating structures in a magnetic linear plasma device," *Phys. Plasmas* **25**, 061203 (2018).
- <sup>39</sup>S. Jaeger, T. Pierre, and C. Rebont, "Direct observation of a cross-field current-carrying plasma rotating around an unstable magnetized plasma column," *Phys. Plasmas* **16**, 022304 (2009).
- <sup>40</sup>E. Gravier, E. Plaut, X. Caron, and M. Jenny, "Transitions between drift waves in a magnetized cylindrical plasma: Experiments and fluid model, solved with a spectral method," *Eur. Phys. J. D* **67**, 7 (2013).
- <sup>41</sup>G. Y. Antar, J. H. Yu, and G. Tynan, "The origin of convective structures in the scrape-off layer of linear magnetic fusion devices investigated by fast imaging," *Phys. Plasmas* **14**, 022301 (2007).
- <sup>42</sup>C. Schröder, O. Grulke, T. Klinger, and V. Naulin, "Spatial mode structures of electrostatic drift waves in a collisional cylindrical helicon plasma," *Phys. Plasmas* **11**, 4249 (2004).
- <sup>43</sup>M. Light, F. F. Chen, and P. Colestock, "Quiescent and unstable regimes of a helicon plasma," *Plasma Sources Sci. Technol.* **11**, 273 (2002).
- <sup>44</sup>A. Simon, "Ambipolar diffusion in a magnetic field," *Phys. Rev.* **98**, 317 (1955).
- <sup>45</sup>S. J. Zweben, R. Gueroult, and N. J. Fisch, "Plasma mass separation," *Phys. Plasmas* **25**, 090901 (2018).
- <sup>46</sup>R. Gueroult, S. J. Zweben, N. J. Fisch, and J. M. Rax, " $E \times B$  configurations for high-throughput plasma mass separation: An outlook on possibilities and challenges," *Phys. Plasmas* **26**, 043511 (2019).
- <sup>47</sup>B. Lehnert, "A partially ionized plasma centrifuge," *Phys. Scr.* **2**, 106 (1970).
- <sup>48</sup>B. Lehnert, "The partially ionized plasma centrifuge," *Phys. Scr.* **7**, 102 (1973).
- <sup>49</sup>B. Trotabas and R. Gueroult, "Trade-off in perpendicular electric field control using negatively biased emissive end-electrodes," *Plasma Sources Sci. Technol.* **31**, 025001 (2022).
- <sup>50</sup>A. J. Fetterman and N. J. Fisch, "Alpha channeling in a rotating plasma," *Phys. Rev. Lett.* **101**, 205003 (2008).
- <sup>51</sup>J. Bohlmark, U. Helmersson, M. VanZeeland, I. Axnäs, J. Alami, and N. Brenning, "Measurement of the magnetic field change in a pulsed high current magnetron discharge," *Plasma Sources Sci. Technol.* **13**, 654 (2004).
- <sup>52</sup>G. Ecker and H. Kanne, "Cylindrical plasma column in a transverse magnetic field," *Phys. Fluids* **7**, 1834 (1964).
- <sup>53</sup>W. B. Kunkel, "Hall effect in a plasma," *Am. J. Phys.* **49**, 733 (1981).
- <sup>54</sup>J. Claustre, B. Chaudhury, G. Fubiani, M. Paulin, and J. P. Boeuf, "Particle-in-cell Monte Carlo collision model on GPU-application to a low-temperature magnetized plasma," *IEEE Trans. Plasma Sci.* **41**, 391 (2013).
- <sup>55</sup>C. E. S. Phillips, "The action of magnetised electrodes upon electrical discharge phenomena in rarefied gases," *Proc. R. Soc. London* **A64**, 172 (1899).
- <sup>56</sup>W. Knauer, "Mechanism of the penning discharge at low pressures," *J. Appl. Phys.* **33**, 2093 (1962).
- <sup>57</sup>N. V. Mamedov, N. N. Schitov, D. V. Kolodko, I. A. Sorokin, and D. N. Sinel'nikov, "Discharge characteristics of the Penning plasma source," *Tech. Phys.* **63**, 1129–1136 (2018).
- <sup>58</sup>H. Cun, A. Spescha, A. Schuler, M. Hengsberger, J. Osterwalder, and T. Greber, "Characterization of a cold cathode Penning ion source for the implantation of noble gases beneath 2D monolayers on metals: Ions and neutrals," *J. Vac. Sci. Technol. A* **34**, 020602 (2016).
- <sup>59</sup>D. Faircloth and S. Lawrie, "An overview of negative hydrogen ion sources for accelerators," *New J. Phys.* **20**, 025007 (2018).
- <sup>60</sup>B. K. Das and A. Shyam, "Development of compact size penning ion source for compact neutron generator," *Rev. Sci. Instrum.* **79**, 123305 (2008).
- <sup>61</sup>N. A. Kervalishvili, "Rotational Instability of a charged plasma in crossed fields and generation of electrons of anomalously high energy," *Sov. J. Plasma Phys.* **15**, 98 (1989).
- <sup>62</sup>N. A. Kervalishvili, "Evolution of non-linear structures in charged plasmas in crossed fields," *Sov. J. Plasma Phys.* **15**, 436 (1989).
- <sup>63</sup>N. A. Kervalishvili, "Electron vortices in a nonneutral plasma in crossed  $E \times H$  fields," *Phys. Lett. A* **157**, 391 (1991).
- <sup>64</sup>N. A. Kervalishvili and G. Kervalishvili, "The mechanism of stability of long-lived, self-organized solitary vortex in nonneutral electron plasma," *J. Georgian Geophys. Soc.* **4**, 115 (1999).
- <sup>65</sup>J. Thornton, "Magnetron sputtering: Basic physics and application to cylindrical magnetrons," *J. Vac. Sci. Technol.* **15**, 171 (1978).
- <sup>66</sup>A. I. Morozov and V. V. Savelyev, in *Reviews of Plasma Physics*, edited by B. B. Kadomtsev and V. D. Shafranov (Kluwer Academic/Plenum Publishers, New York, 2000), Vol. 21.
- <sup>67</sup>I. Levchenko, K. Bazaka, Y. Ding, Y. Raitses, S. Mazouffre, T. Henning, P. J. Klar, S. Shinohara, J. Schein, L. Garrigues, M. Kim, D. Lev, F. Taccogna, R. W. Boswell, C. Charles, H. Koizumi, Y. Shen, C. Scharlemann, M. Keidar, and S. Xu, "Space micropropulsion systems for Cubesats and small satellites: From proximate targets to furthestmost frontiers," *Appl. Phys. Rev.* **5**, 011104 (2018).
- <sup>68</sup>I. G. Mikellides, I. Katz, R. R. Hofer, and D. M. Goebel, "Magnetic shielding of a laboratory Hall thruster. I. Theory and validation," *J. Appl. Phys.* **115**, 043303 (2014).
- <sup>69</sup>R. R. Hofer, D. M. Goebel, I. G. Mikellides, and I. Katz, "Magnetic shielding of a laboratory Hall thruster. II. Experiments," *J. Appl. Phys.* **115**, 043304 (2014).
- <sup>70</sup>L. L. Su and B. A. Jorns, "Performance comparison of a 9-kW magnetically shielded Hall thruster operating on xenon and krypton," *J. Appl. Phys.* **130**, 163306 (2021).
- <sup>71</sup>Y. Raitses and N. J. Fisch, "Parametric investigations of a nonconventional Hall thruster," *Phys. Plasmas* **8**, 2579 (2001).
- <sup>72</sup>Y. Raitses, E. Merino, and N. J. Fisch, "Cylindrical Hall thrusters with permanent magnets," *J. Appl. Phys.* **108**, 093307 (2010).
- <sup>73</sup>G. Doh, H. Kim, D. Lee, S. Park, S. Mazouffre, and W. Choe, "Structure of the ion acceleration region in cylindrical Hall thruster plasmas," *J. Phys. D* **55**, 225204 (2022).
- <sup>74</sup>E. Y. Choueiri, "Fundamental difference between the two Hall thruster variants," *Phys. Plasmas* **8**, 5025–5033 (2001).
- <sup>75</sup>M. Keidar, I. Boyd, and I. Beilis, "Modeling of a high-power thruster with anode layer," *Phys. Plasmas* **11**, 1715 (2004).
- <sup>76</sup>V. P. Kim, "On the longitudinal distribution of electric field in the acceleration zones of plasma accelerators and thrusters with closed electron drift," *Plasma Phys. Rep.* **43**, 486 (2017).
- <sup>77</sup>J. Simmonds and Y. Raitses, "Ion acceleration in a wall-less Hall thruster," *J. Appl. Phys.* **130**, 093302 (2021).
- <sup>78</sup>A. Kapulkin, A. D. Grishkevich, and V. F. Prisnyakov, "Outside electric field thruster," *Space Technol.* **15**, 391 (1995).
- <sup>79</sup>J. Vaudolon, S. Mazouffre, C. Hénaux, D. Harribey, and A. Rossi, "Optimization of a wall-less Hall thruster," *Appl. Phys. Lett.* **107**, 174103 (2015).
- <sup>80</sup>S. Mazouffre, J. Vaudolon, S. Tsikata, G. Largeau, C. Hénaux, D. Harribey, and A. Rossi, "Optimization of magnetic field topology and anode geometry for a wall-less Hall thruster," in 34th International Electric Propulsion Conference, Kobe, Japan, 2015.
- <sup>81</sup>S. Mazouffre, S. Tsikata, and J. Vaudolon, "Development and experimental characterization of a wall-less Hall thruster," *J. Appl. Phys.* **116**, 243302 (2014).

- <sup>82</sup>A. Anders, "Plasma and ion sources in large area coating: A review," *Surf. Coat. Technol.* **200**, 1893–1906 (2005).
- <sup>83</sup>N. Oudini, L. Garrigues, G. J. M. Hagelaar, and J. P. Boeuf, "Numerical study of the characteristics of the ion and fast atom beams in an end-Hall ion source," *J. Appl. Phys.* **112**, 083301 (2012).
- <sup>84</sup>U. Fantz, S. Briefi, A. Heiler, C. Wimmer, and D. Wunderlich, "Negative hydrogen ion sources for fusion: From plasma generation to beam properties," *Front. Phys.* **9**, 709651 (2021).
- <sup>85</sup>J. P. Boeuf, J. Claustre, B. Chaudhury, and G. Fubiani, "Physics of a magnetic filter for negative ion sources. II.  $E \times B$  drift through the filter in a real geometry," *Phys. Plasmas* **19**, 113510 (2012).
- <sup>86</sup>G. Fubiani and J. P. Boeuf, "Plasma asymmetry due to the magnetic filter in fusion-type negative ion sources: Comparisons between two and three-dimensional particle-in-cell simulations," *Phys. Plasmas* **21**, 073512 (2014).
- <sup>87</sup>G. Fubiani and J. P. Boeuf, "Three-dimensional modeling of a negative ion source with a magnetic filter: Impact of biasing the plasma electrode on the plasma asymmetry," *Plasma Sources Sci. Technol.* **24**, 055001 (2015).
- <sup>88</sup>G. Fubiani, L. Garrigues, G. Hagelaar, N. Kohen, and J. P. Boeuf, "Modeling of plasma transport and negative ion extraction in a magnetized radio-frequency plasma source," *New J. Phys.* **19**, 015002 (2017).
- <sup>89</sup>J. P. Boeuf, G. J. M. Hagelaar, P. Sarraih, G. Fubiani, and N. Kohen, "Model of an inductively coupled negative ion source: II. Application to an ITER type source," *Plasma Sources Sci. Technol.* **20**, 015002 (2011).
- <sup>90</sup>U. Fantz, L. Schiesko, and D. Wunderlich, "Plasma expansion across a transverse magnetic field in a negative hydrogen ion source for fusion," *Plasma Sources Sci. Technol.* **23**, 044002 (2014).
- <sup>91</sup>J. P. Boeuf, B. Chaudhury, and L. Garrigues, "Physics of a magnetic filter for negative ion sources. I. Collisional transport across the filter in an ideal, 1D filter," *Phys. Plasmas* **19**, 113509 (2012).
- <sup>92</sup>N. Goldenfeld and L. P. Kadanoff, "Simple lessons from complexity," *Science* **284**, 87 (1999).
- <sup>93</sup>W. Frias, A. I. Smolyakov, I. D. Kaganovich, and Y. Raitses, "Long wavelength gradient drift instability in Hall plasma devices. I. Fluid theory," *Phys. Plasmas* **19**, 072112 (2012).
- <sup>94</sup>V. P. Lakhin, V. I. Ilgisonis, A. I. Smolyakov, E. A. Sorokina, and N. A. Marusov, "Effects of finite electron temperature on gradient drift instabilities in partially magnetized plasmas," *Phys. Plasmas* **25**, 012106 (2018).
- <sup>95</sup>V. P. Lakhin, V. I. Ilgisonis, A. I. Smolyakov, E. A. Sorokina, and N. A. Marusov, "Marginal stability, characteristic frequencies, and growth rates of gradient drift modes in partially magnetized plasmas with finite electron temperature," *Phys. Plasmas* **25**, 012107 (2018).
- <sup>96</sup>A. M. Fridman, "On the phenomena of the critical magnetic field and anomalous diffusion in weakly ionized plasmas," *Sov. Phys. Dokl.* **9**, 75 (1964).
- <sup>97</sup>A. Simon, "Instability of a partially ionized plasma in crossed electric and magnetic fields," *Phys. Fluids* **6**, 382 (1963).
- <sup>98</sup>F. C. Hoh, "Instability of Penning-type discharges," *Phys. Fluids* **6**, 1184 (1963).
- <sup>99</sup>K. I. Thomassen, "Turbulent diffusion in a Penning-type discharge," *Phys. Fluids* **9**, 1836 (1966).
- <sup>100</sup>Y. Sakawa, N. Joshi, O. K. Kaw, F. F. Chen, and V. K. Jain, "Excitation of the modified Simon-Hoh instability in an electron beam produced plasma," *Phys. Fluids B* **5**, 1681 (1993).
- <sup>101</sup>A. Kapulkin and M. M. Guelman, "Low-frequency instability in near-anode region of hall thruster," *IEEE Trans. Plasma Sci.* **36**, 2082 (2008).
- <sup>102</sup>K. Hara, A. R. Mansour, and S. Tsikata, "Theory of gradient drift instabilities in low-temperature, partially magnetised plasmas," *J. Plasma Phys.* **88**, 905880408 (2022).
- <sup>103</sup>I. O. Pogutse, A. I. Smolyakov, and A. Hirose, "Magnetohydrodynamic equations for plasmas with finite Larmor radius effects," *J. Plasma Phys.* **60**, 133 (1998).
- <sup>104</sup>A. Litvak and N. J. Fisch, "Resistive instabilities in Hall current plasma discharge," *Phys. Plasmas* **8**, 648 (2001).
- <sup>105</sup>J. P. Boeuf, "Micro instabilities and rotating spokes in the near-anode region of partially magnetized plasmas," *Phys. Plasmas* **26**, 072113 (2019).
- <sup>106</sup>M. C. Kelley, *The Earth's Ionosphere: Plasma Physics and Electrodynamics* (Academic Press/Elsevier, San Diego, CA, 2009).
- <sup>107</sup>V. Morin and A. I. Smolyakov, "Modification of the Simon-Hoh instability by the sheath effects in partially magnetized  $E \times B$  plasmas," *Phys. Plasmas* **25**, 084505 (2018).
- <sup>108</sup>B. D. Dudson, M. V. Umansky, X. Q. Xu, P. B. Snyder, and H. R. Wilson, "BOUT++: A framework for parallel plasma fluid simulations," *Comput. Phys. Commun.* **180**, 1467–1480 (2009).
- <sup>109</sup>O. Koshkarov, A. Smolyakov, Y. Raitses, and I. Kaganovich, "Self-organization, structures, and anomalous transport in turbulent partially magnetized plasmas with crossed electric and magnetic fields," *Phys. Rev. Lett.* **122**, 185001 (2019).
- <sup>110</sup>P. S. Gary, "Longitudinal waves in a perpendicular collisionless plasma shock. II. Vlasov ions," *J. Plasma Phys.* **4**, 753 (1970).
- <sup>111</sup>S. Janhunen, A. Smolyakov, D. Sydorenko, M. Jimenez, I. Kaganovich, and Y. Raitses, "Evolution of the electron cyclotron drift instability in two-dimensions," *Phys. Plasmas* **25**, 082308 (2018).
- <sup>112</sup>A. Smolyakov, T. Zintel, L. Couedel, D. Sydorenko, A. Umnov, E. Sorokina, and N. Marusov, "Anomalous electron transport in one-dimensional electron cyclotron drift turbulence," *Plasma Phys. Rep.* **46**, 496 (2020).
- <sup>113</sup>J. Cavalier, N. Lemoine, G. Bonhomme, S. Tsikata, C. Honoré, and D. Grésillon, "Hall thruster plasma fluctuations identified as the  $E \times B$  electron drift instability: Modeling and fitting on experimental data," *Phys. Plasmas* **20**, 082107 (2013).
- <sup>114</sup>S. Janhunen, A. Smolyakov, O. Chapurin, D. Sydorenko, I. Kaganovich, and Y. Raitses, "Nonlinear structures and anomalous transport in partially magnetized  $E \times B$  plasmas," *Phys. Plasmas* **25**, 011608 (2018).
- <sup>115</sup>A. Ducrocq, J. C. Adam, A. Héron, and G. Laval, "High-frequency electron drift instability in the cross-field configuration of Hall thrusters," *Phys. Plasmas* **13**, 102111 (2006).
- <sup>116</sup>A. Ducrocq, *Rôle des Instabilités Électroniques de Dérive Dans le Transport Électronique du Propulseur à Effet Hall* (Ecole Polytechnique, Centre de Physique Théorique, 2010).
- <sup>117</sup>C. K. Birdsall and A. B. Langdon, *Plasma Physics via Computer Simulation* (Taylor & Francis Ltd, 2004).
- <sup>118</sup>R. W. Hockney and J. W. Eastwood, *Computer Simulations Using Particles* (Taylor & Francis, New York, London, 1988).
- <sup>119</sup>C. K. Birdsall, "Particle-In-Cell charged-particle simulations plus Monte Carlo Collisions with neutral atoms, PIC-MCC," *IEEE Trans. Plasma Sci.* **19**, 65 (1991).
- <sup>120</sup>J. P. Verboncoeur, "Particle simulation of plasmas: Review and advances," *Plasma Phys. Controlled Fusion* **47**, A231 (2005).
- <sup>121</sup>D. Tskhakaya, K. Matyash, R. Schneider, and F. Taccogna, "The particle-in-cell method," *Contrib. Plasma Phys.* **47**, 563 (2007).
- <sup>122</sup>Z. Donkó, A. Derzsi, M. Vass, B. Hováth, S. Wilczek, B. Hartmann, and P. Hartmann, "eduPIC: An introductory particle based code for radio-frequency plasma simulation," *Plasma Sources Sci. Technol.* **30**, 095017 (2021).
- <sup>123</sup>F. Faraji, M. Reza, and A. Knoll, "Verification of the generalized reduced-order particle-in-cell scheme in a radial azimuthal  $E \times B$  plasma configuration," *arXiv:2211.16604* (2022).
- <sup>124</sup>M. Reza, F. Faraji, and A. Knoll, "Resolving multi-dimensional plasma phenomena in Hall thrusters using the reduced-order particle in cell scheme," *J. Electric Propul.* **1**, 19 (2022).
- <sup>125</sup>Y. Raitses, I. Kaganovich, and A. Smolyakov, "Effect of the gas pressure on low frequency oscillations in  $E \times B$  discharges," in Joint Conference of 30th ISTS, 34th IEPC, and 6th Kobe, Japan, 2015.
- <sup>126</sup>Y. Raitses, E. Rodríguez, V. Skoutnev, A. Powis, B. Kraus, I. Kaganovich, and A. Smolyakov, "Characterization of the  $E \times B$  penning discharge using electrostatic probes," in 36th International Electric Propulsion Conference, Vienna, Austria, 2019.
- <sup>127</sup>J. Carlsson, I. Kaganovich, A. Powis, Y. Raitses, I. Romadanov, and A. Smolyakov, "Particle-in-cell simulations of anomalous transport in a Penning discharge," *Phys. Plasmas* **25**, 061201 (2018).
- <sup>128</sup>A. T. Powis, J. A. Carlsson, I. Kaganovich, Y. Raitses, and A. Smolyakov, "Scaling of spoke rotation frequency within a Penning discharge," *Phys. Plasmas* **25**, 072110 (2018).
- <sup>129</sup>M. McDonald, C. Bellant, A. S. P. Brandon, and A. Gallimore, "Measurement of cross-field electron current in a Hall thruster due to rotating spoke instabilities," AIAA Paper No. AIAA 2011-5810, 2011.



- <sup>130</sup>M. McDonald and A. D. Gallimore, "Rotating spoke instabilities in Hall thrusters," *IEEE Trans. Plasma Sci.* **39**, 2952 (2011).
- <sup>131</sup>M. J. Sekerak, "Plasma oscillations and operation modes in Hall effect thrusters," Ph.D. thesis (Michigan State University, 2014).
- <sup>132</sup>M. J. Sekerak, B. W. Longmier, A. D. Gallimore, D. L. Brown, R. R. Hofer, and J. E. Polk, "Azimuthal spoke propagation in Hall effect thrusters," *IEEE Trans. Plasma Sci.* **43**, 72–85 (2015).
- <sup>133</sup>M. J. Sekerak, A. D. Gallimore, D. L. Brown, R. R. Hofer, and J. E. Polk, "Mode transitions in hall-effect thrusters induced by variable magnetic field strength," *J. Propul. Power* **32**, 903 (2016).
- <sup>134</sup>C. L. Ellison, Y. Raitses, and N. J. Fisch, "Cross-field electron transport induced by rotating spoke in a cylindrical Hall thruster," *Phys. Plasmas* **19**, 013503 (2012).
- <sup>135</sup>S. Mazouffre, L. Grimaud, S. Tsikata, K. Matyash, and R. Schneider, "Rotating spoke instabilities in a wall-less Hall thruster: Experiments," *Plasma Sources Sci. Technol.* **28**, 054002 (2019).
- <sup>136</sup>J. Bak, R. Kawashima, K. Komurasaki, and H. Koizumi, "Plasma formation and cross-field electron transport induced by azimuthal neutral inhomogeneity in an anode layer Hall thruster," *Phys. Plasmas* **26**, 073505 (2019).
- <sup>137</sup>J. Bak, R. Kawashima, G. Romanelli, and K. Komurasaki, "Plasma structure and electron cross-field transport induced by azimuthal manipulation of the radial magnetic field in a Hall thruster  $E \times B$  discharge," *J. Appl. Phys.* **131**, 053302 (2022).
- <sup>138</sup>J. Winter, A. Hecimovic, T. de los Arcos, M. Böke, and V. Schulz-von der Gathen, "Instabilities in high-power impulse magnetron plasmas: From stochasticity to periodicity," *J. Phys. D* **46**, 084007 (2013).
- <sup>139</sup>N. Brenning, D. Lundin, T. Minea, C. Costin, and C. Vitelaru, "Spokes and charged particle transport in HiPIMS magnetrons," *J. Phys. D* **46**, 084005 (2013).
- <sup>140</sup>A. Anders, M. Panjan, R. Franz, J. Andersson, and P. Ni, "Drifting potential humps in ionization zones: The 'propeller blades' of high power impulse magnetron sputtering," *Appl. Phys. Lett.* **103**, 144103 (2013).
- <sup>141</sup>A. Hecimovic, V. Schulz-von der Gathen, M. Böke, A. von Keudell, and J. Winter, "Spoke transitions in HiPIMS discharges," *Plasma Sources Sci. Technol.* **24**, 045005 (2015).
- <sup>142</sup>T. Ito, C. V. Young, and M. A. Cappelli, "Self-organization in planar magnetron microdischarge plasmas," *Appl. Phys. Lett.* **106**, 254104 (2015).
- <sup>143</sup>M. Panjan, S. Loquai, J. E. Klemberg-Sapieha, and L. Martinu, "Non-uniform plasma distribution in dc magnetron sputtering: Origin, shape and structuring of spokes," *Plasma Sources Sci. Technol.* **24**, 065010 (2015).
- <sup>144</sup>M. Panjan, "Self-organizing plasma behavior in RF magnetron sputtering discharges," *J. Appl. Phys.* **125**, 203303 (2019).
- <sup>145</sup>J. Held, M. George, and A. von Keudell, "Spoke-resolved electron density, temperature and potential in direct current magnetron sputtering and HiPIMS discharges," *Plasma Sources Sci. Technol.* **31**, 085013 (2022).
- <sup>146</sup>S. Oldenbürger, F. Brochard, and G. Bonhomme, "Investigation of mode coupling in a magnetized plasma column using fast imaging," *Phys. Plasmas* **18**, 032307 (2011).
- <sup>147</sup>J. Y. Kim, J. Y. Jang, J. Choi, J. Wang, W. I. Jeaong, M. A. I. Elgarhy, G. Go, K. J. Chung, and Y. S. Hwang, "Magnetic confinement and instability in partially magnetized plasma," *Plasma Sources Sci. Technol.* **30**, 025011 (2021).
- <sup>148</sup>J.-P. Boeuf and B. Chaudhury, "Rotating instability in low-temperature magnetized plasmas," *Phys. Rev. Lett.* **111**, 155005 (2013).
- <sup>149</sup>K. Matyash, R. Schneider, S. Mazouffre, S. Tsikata, and L. Grimaud, "Rotating spoke instabilities in a wall-less Hall thruster: Simulations," *Plasma Sources Sci. Technol.* **28**, 044002 (2019).
- <sup>150</sup>J. P. Boeuf and M. Takahashi, "Rotating spokes, ionization instability, and electron vortices in partially magnetized  $E \times B$  plasmas," *Phys. Rev. Lett.* **124**, 185005 (2020).
- <sup>151</sup>J. P. Boeuf and M. Takahashi, "New insights into the physics of rotating spokes in partially magnetized  $E \times B$  plasmas," *Phys. Plasmas* **27**, 083520 (2020).
- <sup>152</sup>M. Sengupta, A. Smolyakov, and Y. Raitses, "Restructuring of rotating spokes in response to changes in the radial electric field and the neutral pressure of a cylindrical magnetron plasma," *J. Appl. Phys.* **129**, 223302 (2021).
- <sup>153</sup>M. Tyushev, M. Zadeh, V. Sharma, M. Sengupta, Y. Raitses, J. P. Boeuf, and A. Smolyakov, "Azimuthal structures and turbulent transport in Penning discharges," *Phys. Plasmas* **30**, 033506 (2023).
- <sup>154</sup>J. P. Boeuf, "Spoke formation in low temperature  $E \times B$  plasmas. Transition from gradient-drift instability to ionization wave," *Phys. Plasmas* **30**, 022112 (2023).
- <sup>155</sup>A. R. Mansour and K. Hara, "Full fluid moment modeling of rotating spokes in Penning-type configuration," *Plasma Sources Sci. Technol.* **31**, 055012 (2022).
- <sup>156</sup>R. Kawashima, K. Hara, and K. Komurasaki, "Numerical analysis of azimuthal rotating spokes in a crossed-field discharge plasma," *Plasma Sources Sci. Technol.* **27**, 035010 (2018).
- <sup>157</sup>L. Xu, D. Eremin, and R. P. Brinkmann, "Direct evidence of gradient drift instability being the origin of a rotating spoke in a crossed field plasma," *Plasma Sources Sci. Technol.* **30**, 075013 (2021).
- <sup>158</sup>L. Xu, D. Eremin, A. Smolyakov, D. Krüger, K. Köhn, and R. P. Brinkmann, "Formation mechanism of the rotating spoke in partially magnetized plasmas," *Plasma Sources Sci. Technol.* (2022), [arXiv:2202.07033](https://arxiv.org/abs/2202.07033)
- <sup>159</sup>R. Lucken, A. Bourdon, M. A. Lieberman, and P. Chabert, "Instability-enhanced transport in low temperature magnetized plasma," *Phys. Plasmas* **26**, 070702 (2019).
- <sup>160</sup>N. Meezan, W. Hargus, and M. Cappelli, "Anomalous electron mobility in a coaxial Hall discharge plasma," *Phys. Rev. E* **63**, 026410 (2001).
- <sup>161</sup>A. W. Smith and M. A. Cappelli, "On the role of fluctuations, cathode placement, and collisions on the transport of electrons in the near-field of Hall thrusters," *Phys. Plasmas* **17**, 093501 (2010).
- <sup>162</sup>M. MC Donald, "Electron transport in hall thrusters," Ph.D. thesis (Michigan State University, 2012).
- <sup>163</sup>E. Y. Choueiri, "Plasma oscillations in Hall thrusters," *Phys. Plasmas* **8**, 1411 (2001).
- <sup>164</sup>A. I. Morozov and V. V. Savel'ev, "Numerical simulation of plasma flow dynamics in SPT," in 24th International Electric Propulsion Conference, Moscow, Russia, 1995.
- <sup>165</sup>J. Fife, M. Martinez-Sanchez, and J. Szabo, "A numerical study of low-frequency discharge oscillations in Hall thrusters," AIAA Paper No. AIAA 1997-3052 (1997).
- <sup>166</sup>J. Boeuf and L. Garrigues, "Low frequency oscillations in a stationary plasma thruster," *J. Appl. Phys.* **84**, 3541 (1998).
- <sup>167</sup>S. Barral, K. Makowski, Z. Peradzynski, N. Gascon, and M. Dudeck, "Wall material effects in stationary plasma thrusters. II. Near-wall and in-wall conductivity," *Phys. Plasmas* **10**, 4137 (2003).
- <sup>168</sup>S. Chable and F. Rogier, "Numerical investigation and modeling of stationary plasma thruster low frequency oscillations," *Phys. Plasmas* **12**, 033504 (2005).
- <sup>169</sup>S. Barral and E. Ahedo, "Low-frequency model of breathing oscillations in Hall discharges," *Phys. Rev. E* **79**, 046401 (2009).
- <sup>170</sup>K. Hara, I. D. Boyd, and V. I. Kolobov, "One-dimensional hybrid-direct kinetic simulation of the discharge plasma in a Hall thruster," *Phys. Plasmas* **19**, 113508 (2012).
- <sup>171</sup>K. Hara, M. J. Sekerak, I. D. Boyd, and A. D. Gallimore, "Perturbation analysis of ionization oscillations in Hall effect thrusters," *Phys. Plasmas* **21**, 122103 (2014).
- <sup>172</sup>O. Chapurin, A. I. Smolyakov, G. Hagelaar, and Y. Raitses, "On the mechanism of ionization oscillations in Hall thrusters," *J. Appl. Phys.* **129**, 233307 (2021).
- <sup>173</sup>O. Chapurin, A. I. Smolyakov, G. Hagelaar, J. P. Boeuf, and Y. Raitses, "Fluid and hybrid simulations of the ionization instabilities in Hall thruster," *J. Appl. Phys.* **132**, 053301 (2022).
- <sup>174</sup>S. Barral and Z. Peradzynski, "Ionization oscillations in Hall accelerators," *Phys. Plasmas* **17**, 014505 (2010).
- <sup>175</sup>L.-Q. Wei, L. Han, D.-R. Yu, and N. Guo, "Low-frequency oscillations in Hall thrusters," *Chin. Phys. B* **24**, 055201 (2015).
- <sup>176</sup>T. Lafleur, P. Chabert, and A. Bourdon, "The origin of the breathing mode in Hall thrusters and its stabilization," *J. Appl. Phys.* **130**, 053305 (2021).
- <sup>177</sup>J. Bareilles, G. J. M. Hagelaar, L. Garrigues, C. Boniface, J. P. Boeuf, and N. Gascon, "Critical assessment of a two-dimensional hybrid Hall thruster model: Comparisons with experiments," *Phys. Plasmas* **11**, 3035 (2004).
- <sup>178</sup>S. Barral, K. Makowski, Z. Peradzynski, and M. Dudeck, "Transit-time instability in Hall thrusters," *Phys. Plasmas* **12**, 073504 (2005).
- <sup>179</sup>E. Fernandez, M. K. Scharfe, C. A. Thomas, N. Gascon, and M. A. Cappelli, "Growth of resistive instabilities in  $E \times B$  plasma discharge simulations," *Phys. Plasmas* **15**, 012102 (2008).

- <sup>180</sup>Y. Lim, W. Choe, S. Mazouffre, J. S. Park, H. Kim, J. Seon, and L. Garrigues, "Nonlinear ion dynamics in Hall thruster plasma source by ion transit-time instability," *Plasma Sources Sci. Technol.* **26**, 031t01 (2017).
- <sup>181</sup>S. Mazouffre, V. Kulaev, and J. P. Luna, "Ion diagnostics of a discharge in crossed electric and magnetic fields for electric propulsion," *Plasma Sources Sci. Technol.* **18**, 034022 (2009).
- <sup>182</sup>J. Vaudolon and S. Mazouffre, "Investigation of the ion transit time instability in a Hall thruster combining time-resolved LIF spectroscopy and analytical calculations," in Joint Conference of 30th International Symposium on Space Technology and Science, 34th International Electric Propulsion Conference and 6th Nano-Satellite Symposium, Hyogo-Kobe, Japan, 2015).
- <sup>183</sup>J. P. Boeuf and L. Garrigues, " $E \times B$  electron drift instability in Hall thrusters: Particle-in-cell simulations vs. theory," *Phys. Plasmas* **25**, 061204 (2018).
- <sup>184</sup>T. Charoy, T. Lafleur, A. A. Laguna, A. Bourdon, and P. Chabert, "The interaction between ion transit-time and electron drift instabilities and their effect on anomalous electron transport in Hall thrusters," *Plasma Sources Sci. Technol.* **30**, 065017 (2021).
- <sup>185</sup>C. S. Janes and R. S. Lowder, "Anomalous electron diffusion and ion acceleration in a low-density plasma," *Phys. Fluids* **9**, 1115 (1966).
- <sup>186</sup>J. B. Parker, Y. Raitses, and N. J. Fisch, "Transition in electron transport in a cylindrical Hall thruster," *Appl. Phys. Lett.* **97**, 091501 (2010).
- <sup>187</sup>A. Guglielmi, F. Gaboriau, and J. P. Boeuf, "Simultaneous measurements of axial motion and azimuthal rotation of non-uniformities ('spokes') in a Hall thruster," *Phys. Plasmas* **29**, 112108 (2022).
- <sup>188</sup>A. Anders, "Self-organization and self-limitation in high power impulse magnetron sputtering," *Appl. Phys. Lett.* **100**, 224104 (2012).
- <sup>189</sup>A. Anders, P. Ni, and A. Rauch, "Drifting localization of ionization runaway: Unraveling the nature of anomalous transport in high power impulse magnetron sputtering," *J. Appl. Phys.* **111**, 053304 (2012).
- <sup>190</sup>Y. Yang, J. Liu, L. Liu, and A. Anders, "Propagation direction reversal of ionization zones in the transition between high and low current magnetron sputtering," *Appl. Phys. Lett.* **105**, 254101 (2014).
- <sup>191</sup>A. Hecimovic, M. Böke, and J. Winter, "The characteristic shape of emission profiles of plasma spokes in HiPIMS: The role of secondary electrons," *J. Phys. D* **47**, 102003 (2014).
- <sup>192</sup>A. Hecimovic and A. von Keudell, "Spokes in high power impulse magnetron sputtering plasmas," *J. Phys. D* **51**, 453001 (2018).
- <sup>193</sup>A. Hecimovic, C. Maszl, V. Schulz-von der Gathen, M. Böke, and A. von Keudell, "Spoke rotation reversal in magnetron discharges of aluminium, chromium and titanium," *Plasma Sources Sci. Technol.* **25**, 035001 (2016).
- <sup>194</sup>M. Panjan and A. Anders, "Plasma potential of a moving ionization zone in DC magnetron sputtering," *J. Appl. Phys.* **121**, 063302 (2017).
- <sup>195</sup>M. Rudolph, N. Brenning, H. Hajihoseini, M. A. Raadu, T. M. Minea, A. Anders, J. T. Gudmundsson, and D. Lundin, "Influence of the magnetic field on the discharge physics of a high power impulse magnetron sputtering discharge," *J. Phys. D* **55**, 015202 (2021).
- <sup>196</sup>C. Huo, D. Lundin, M. A. Raadu, A. Anders, J. T. Gudmundsson, and N. Brenning, "On sheath energization and Ohmic heating in sputtering magnetrons," *Plasma Sources Sci. Technol.* **22**, 045005 (2013).
- <sup>197</sup>A. Anders, "Localized heating of electrons in ionization zones: Going beyond the Penning-Thornton paradigm in magnetron sputtering," *Appl. Phys. Lett.* **105**, 244104 (2014).
- <sup>198</sup>J. C. Adam, A. Héron, and G. Laval, "Study of stationary plasma thrusters using two-dimensional fully kinetic simulations," *Phys. Plasmas* **11**, 295 (2004).
- <sup>199</sup>P. S. Gary and J. J. Sanderson, "Longitudinal waves in a perpendicular collisionless plasma shock: I. Cold ions," *J. Plasma Phys.* **4**, 739 (1970).
- <sup>200</sup>D. Forslund, "Electron cyclotron drift instability and turbulence," *Phys. Fluids* **15**, 1303 (1972).
- <sup>201</sup>D. Forslund, R. Morse, and C. Nielson, "Electron cyclotron drift instability," *Phys. Rev. Lett.* **25**, 1266 (1970).
- <sup>202</sup>V. P. Lakhin, V. I. Ilgisonis, A. I. Smolyakov, and E. A. Sorokina, "Nonlinear excitation of long-wavelength modes in Hall plasmas," *Phys. Plasmas* **23**, 102304 (2016).
- <sup>203</sup>Z. Asadi, F. Taccogna, and M. Sharifian, "Numerical study of electron cyclotron drift instability: application to Hall thruster," *Front. Phys.* **7**, 140 (2019).
- <sup>204</sup>A. Tavassoli, A. Smolyakov, M. Shoucri, and R. J. Spiteri, "Nonlinear regimes of the electron cyclotron drift instability in Vlasov simulations," *Phys. Plasmas* **29**, 030701 (2022).
- <sup>205</sup>A. Tavassoli, M. Zadeh, A. Smolyakov, M. Shoucri, and R. J. Spiteri, "The electron cyclotron drift instability: A comparison of particle-in-cell and continuum Vlasov simulations," *Phys. Plasmas* **30**, 033905 (2023).
- <sup>206</sup>A. Tavassoli, M. Shoucri, A. Smolyakov, M. Papahn Zadeh, and R. J. Spiteri, "Backward waves in the nonlinear regime of the Buneman instability," *Phys. Plasmas* **28**, 022307 (2021).
- <sup>207</sup>N. Jain, T. Umeda, and P. H. Yoon, "Modeling nonlinear development of Buneman instability with linear dispersion theory," *Plasma Phys. Controlled Fusion* **53**, 025010 (2011).
- <sup>208</sup>K. Hara and C. Treece, "Ion kinetics and nonlinear saturation of current-driven instabilities relevant to hollow cathode plasmas," *Plasma Sources Sci. Technol.* **28**, 055013 (2019).
- <sup>209</sup>L. P. Dyrud and M. M. Oppenheim, "Electron holes, ion waves, and anomalous resistivity in space plasmas," *J. Geophys. Res.* **111**, A01302, <https://doi.org/10.1029/2004JA010482> (2006).
- <sup>210</sup>S. Tsikata, C. Honoré, N. Lemoine, and D. M. Grésillon, "Three-dimensional structure of electron density fluctuations in the Hall thruster plasma:  $E \times B$  bar mode," *Phys. Plasmas* **17**, 112110 (2010).
- <sup>211</sup>B. D. Fried and S. D. Conte, *The Plasma Dispersion Function* (Academic Press, New York, NY, 1961).
- <sup>212</sup>M. Lampe, W. M. Manheimer, J. B. McBride, J. H. Orens, K. Papadopoulos, R. Shanny, and R. N. Sudan, "Theory and simulation of the beam cyclotron instability," *Phys. Fluids* **15**, 662 (1972).
- <sup>213</sup>M. Lampe, W. M. Manheimer, J. B. McBride, J. H. Orens, R. Shanny, and R. N. Sudan, "Nonlinear development of the beam-cyclotron instability," *Phys. Rev. Lett.* **26**, 1221 (1971).
- <sup>214</sup>T. Lafleur, S. D. Baalrud, and P. Chabert, "Theory for the anomalous electron transport in Hall effect thrusters. II. Kinetic model," *Phys. Plasmas* **23**, 053503 (2016).
- <sup>215</sup>J. P. Boeuf, "New insights from PIC simulations on the  $E \times B$  Electron Drift Instability in Hall thrusters," in 35th International Electric Propulsion Conference, Atlanta, Georgia, 2017.
- <sup>216</sup>T. Charoy, J. P. Boeuf, A. Bourdon, J. A. Carlsson, P. Chabert, B. Cuenot, D. Eremin, L. Garrigues, K. Hara, I. D. Kaganovich, A. T. Powis, A. Smolyakov, D. Sydorenko, A. Tavant, O. Vermorel, and W. Villafana, "2D axial-azimuthal particle-in-cell benchmark for low-temperature partially magnetized plasmas," *Plasma Sources Sci. Technol.* **28**, 105010 (2019).
- <sup>217</sup>See <https://www.landmark-plasma.com/> for "Low Temperature Partially Magnetized Benchmarks."
- <sup>218</sup>A. Héron and J. C. Adam, "Anomalous conductivity in Hall thrusters: Effects of the non-linear coupling of the electron-cyclotron drift instability with secondary electron emission of the walls," *Phys. Plasmas* **20**, 082313 (2013).
- <sup>219</sup>V. Croes, T. Lafleur, Z. Bonaventura, A. Bourdon, and P. Chabert, "2D particle-in-cell simulations of the electron drift instability and associated anomalous electron transport in Hall-effect thrusters," *Plasma Sources Sci. Technol.* **26**, 034001 (2017).
- <sup>220</sup>A. Tavant, V. Croes, R. Lucken, T. Lafleur, A. Bourdon, and P. Chabert, "The effects of secondary electron emission on plasma sheath characteristics and electron transport in an  $E \times B$  discharge via kinetic simulations," *Plasma Sources Sci. Technol.* **27**, 124001 (2018).
- <sup>221</sup>F. Taccogna, P. Minelli, Z. Asadi, and G. Bogopolsky, "Numerical studies of the  $E \times B$  electron drift instability in Hall thrusters," *Plasma Sources Sci. Technol.* **28**, 064002 (2019).
- <sup>222</sup>W. Villafana, F. Petronio, A. C. Denig, M. J. Jimenez, D. Eremin, L. Garrigues, F. Taccogna, A. Alvarez-Laguna, J. P. Boeuf, A. Bourdon, P. Chabert, T. Charoy, B. Cuenot, K. Hara, F. Pechereau, A. Smolyakov, D. Sydorenko, A. Tavant, and O. Vermorel, "2D radial-azimuthal particle-in-cell benchmark for  $E \times B$  discharges," *Plasma Sources Sci. Technol.* **30**, 075002 (2021).
- <sup>223</sup>C. N. Lashmore-Davies and T. J. Martin, "Electrostatic instabilities driven by an electric current perpendicular to a magnetic field," *Nucl. Fusion* **13**, 193 (1973).
- <sup>224</sup>F. Petronio, A. Tavant, T. Charoy, A. Alvarez Laguna, A. Bourdon, and P. Chabert, "Conditions of appearance and dynamics of the modified two-stream instability in  $E \times B$  discharges," *Phys. Plasmas* **28**, 043504 (2021).

- <sup>225</sup>S. Tsikata, N. Lemoine, V. Pisarev, and D. M. Grésillon, “Dispersion relations of electron density fluctuations in a Hall thruster plasma, observed by collective light scattering,” *Phys. Plasmas* **16**, 033506 (2009).
- <sup>226</sup>S. Tsikata, C. Honoré, and D. Grésillon, “Collective Thomson scattering for studying plasma instabilities in electric thrusters,” *J. Instrum.* **8**, C10012 (2013).
- <sup>227</sup>S. Tsikata, C. Honoré, D. Grésillon, and N. Lemoine, “collective light scattering for the study of fluctuations in magnetized plasmas: The Hall thruster case study,” *Contrib. Plasma Phys.* **51**, 119 (2011).
- <sup>228</sup>F. F. Chen, *Introduction to Plasma Physics and Controlled Fusion* (Plenum Press, New-York, 1984).
- <sup>229</sup>F. Taccogna and P. Minelli, “Three-dimensional particle-in-cell model of Hall thruster: The discharge channel,” *Phys. Plasmas* **25**, 061208 (2018).
- <sup>230</sup>W. Villafana, G. Fubiani, L. Garrigues, G. Vigot, B. Cuenot, and O. Vermorel, “3D Particle-In-Cell modeling of anomalous electron transport driven by the Electron Drift Instability in Hall thrusters,” in *37th International Electric Propulsion Conference* (MIT, Cambridge, MA, 2022).
- <sup>231</sup>J. L. Vay, A. Almgren, J. Bell, L. Ge, D. P. Grote, M. Hogan, O. Kononenko, R. Lehe, A. Myers, C. Ng, J. Park, R. Ryne, O. Shapoval, M. Thévenet, and W. Zhang, “Warp-X: A new exascale computing platform for beam-plasma simulations,” *Nucl. Instrum. Methods Phys. Res., Sect. A* **909**, 476 (2018).